Rhodes University

Master's Thesis

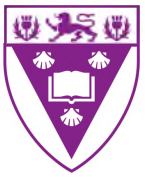

RHODES UNIVERSITY
Where leaders learn

A PILOT WIDE-FIELD VLBI SURVEY OF THE GOODS-NORTH FIELD

Author: Alexander Akoto-Danso

Supervisor: Roger P. Deane
Co-Supervisors: Oleg M. Smirnov & Gianni Bernardi

A thesis submitted in fulfillment of the requirements for the degree of Master of Science

in the

Centre for Radio Astronomy Techniques and Technologies
Department of Physics and Electronics

August, 2018

Declaration of Authorship

I, Alexander Akoto-Danso, declare that this thesis titled, '*A PILOT WIDE-FIELD VLBI SURVEY OF THE GOODS-NORTH FIELD*' and the work presented in it are my own. I confirm that:

- This work was done wholly or mainly while in candidature for a research degree at this University.
- Where any part of this thesis has previously been submitted for a degree or any other qualification at this University or any other institution, this has been clearly stated.
- Where I have consulted the published work of others, this is always clearly attributed.
- Where I have quoted from the work of others, the source is always given. With the exception of such quotations, this thesis is entirely my own work.
- I have acknowledged all main sources of help.
- Where the thesis is based on work done by myself jointly with others, I have made clear exactly what was done by others and what I have contributed myself.

Signed: 

Date: 22/10/2018

Abstract

Very Long Baseline Interferometry (VLBI) has significant advantages in disentangling active galactic nuclei (AGN) from star formation, particularly at intermediate to high-redshift due to its high angular resolution and insensitivity to dust. Surveys using VLBI arrays are only just becoming practical over wide areas with numerous developments and innovations (such as multi-phase centre techniques) in observation and data analysis techniques. However, fully automated pipelines for VLBI data analysis are based on old software packages and are unable to incorporate new calibration and imaging algorithms. In this work, the researcher developed a pipeline for VLBI data analysis which integrates a recent wide-field imaging algorithm, RFI excision, and a purpose-built source finding algorithm specifically developed for the 64k×64k wide-field VLBI images. The researcher used this novel pipeline to process 6% ($\sim$ 9 arcmin^2 of the total 160 arcmin^2) of the data from the CANDELS GOODS-North extragalactic field at 1.6 GHz. The milli-arcsec scale images have an average rms of $\sigma \sim 10$ uJy/beam. Forty four (44) candidate sources were detected, most of which are at sub-mJy flux densities, having brightness temperatures and luminosities of $\geq 5\times10^5$ K and $\geq 6\times10^{21}$ W Hz^{-1} respectively. This work demonstrates that automated post-processing pipelines for wide-field, uniform sensitivity VLBI surveys are feasible and indeed made more efficient with new software, wide-field imaging algorithms and more purpose-built source-finders. This broadens the discovery space for future wide-field surveys with upcoming arrays such as the African VLBI Network (AVN), MeerKAT and the Square Kilometre Array (SKA).

Acknowledgements

I want to give thanks to all persons that have become a big part of this study directly or indirectly.

Firstly, I would like to thank the Almighty God for the strength and wisdom to complete this work.

To my family, especially my pretty girls, Nasya and Ann-Hallel for all the play times I missed with you in order to finish this study. Most importantly, I want to acknowledge my wife Audrey Marian Akoto-Danso for her patience, encouragement and love.

I would again thank my mother, siblings and in-laws for taking care of my pretty angels while I was pursuing this study. I really want to thank you all for the prayers and support throughout some of my terrible moments undertaking this study away from home.

My gratitude also goes to Ronel, who has been excellent in organising my many trips and for making sure my funding arrives on time. You really are a gem.

To my supervisor, Dr Roger P. Deane for your dedication and patience afforded me throughout this work. You really are extraordinary in terms of teaching the fundamentals and breaking difficult tasks down. I thank you for the advice, guidance and encouragement you gave me and for your support when I had to take some time off to go witness the birth of my second child. I am grateful to you. To Professor Oleg M. Smirnov, for giving me the funding and for assigning me to work with Roger. I am grateful to you for all the opportunities you gave me to learn, travel to workshops and conferences in order to help me acquire the necessary skills for this study. Sincere thanks also goes to Dr. Gianni Bernardi, Dr Jozsa I. G. Gyula and Dr Sandeep Sirothia for the many discussions we engaged in for the success of this work.

Many thanks also go to the other survey team members: Matt Jarvis (Oxford,UWC), Zsolt Paragi (JIVE), Mike Garrett (currently at Jodrell, Machester), Tom Mauch (SKA-SA), Stephen Bourke (Caltech), Ian Heywood (ATNF, Rhodes) and Peter Barthel (Groningen).

Thank you to the MIDPREP organisers for exposing me to the world of astronomy in the eyes of the LOFAR team. Thanks also go to my host Zsolt Paragi for making my stay worthwhile. Am also grateful to Professor Mike Garrett and Miriam Janssen for making my last day at ASTRON memorable. Sincere thanks also goes to Ardenne Arnold, for his intellectual discussions on the mid-frequency aperture array. I would like to mention that I enjoyed all the organisation Bob Campbell put in for the fun games and the wadlopen trip. My sincere gratitude also goes to Floor Broekgaarden for all her organising she did for those trips and for showing us around.

Lastly, to all the RATT research group members, I say a very big thank you for all your criticisms and talks: Lerato, Theo, Kela, Marcel, Etienne, Urich, Diana and Sam just to mention a few. Your inputs to this work are greatly recognised.

The financial assistance of the National Research Foundation towards this research is hereby acknowledged. Opinions expressed in this work and the conclusions arrived at, are those of the author, and are not necessarily to be attributed to the National Research Foundation.

Contents

List of Figures

List of Tables

Abbreviations

AEGIS	**A**ll-wavelength **G**roth **S**trip **I**nternational **S**urvey
AIPS	**A**stronomical **I**mage **P**rocessing **S**ystem
AVN	**A**frican **V**LBI **N**etwork
CANDELS	**C**osmic **A**ssembly **N**ear-Infrared **D**eep **E**xtragalactic **L**egacy **S**urvey
CASA	**C**ommon **A**stronomy **S**oftware **A**pplications
COSMOS	**COSM**mic Ev**O**lution **S**urvey
CDDIS	**C**rystal **D**ynamics **D**ata **I**nformation **S**ystem
DEC	**Dec**lination
ESA	**E**uropean **S**pace **A**gency
EOP	**E**arth **O**rientation **P**arameters
FITS	**F**lexible **I**mage **T**ransport **S**ystem
FITS-IDI	**F**lexible **I**mage **T**ransport **S**ystem - **I**nterferometry **D**ata **I**nterchange
FFT	**F**ast **F**ourier **T**ransform
FWHM	**F**ull **W**idth at **H**alf **M**aximum
GOODS-N	**G**reat **O**bservatories **O**rigins **D**eep **S**urvey-**N**orth
HDFN	**H**ubble **D**eep **F**ield **N**orth
HST	**H**ubble **S**pace **T**elescope
ICRF	**I**nternational **C**elestial **R**eference **F**rame
IONEX	**ION**osphere map **EX**change
IPP	**I**ntegrated **P**erformance **P**rimitive
LOFAR	**LO**w- **F**requency **A**rray
KAT-7	**K**aroo **A**ntenna **T**elescope-7
KVN	**K**orean **V**LBI **N**etwork
LADUMA	**L**ooking **A**t the **D**istant **U**niverse with the MeerKAT **A**rray
MeerKAT	**Meer** **K**aroo **A**ntenna **T**elescope
MIGHTEE	**M**eerKAT **I**nternational **G**igaHertz **T**iered **E**xtragalactic **E**xploration

MWA	**M**urchison **W**ide-field **A**rray
MPI	**M**essage **P**assing **I**nterface
NASA	**N**ational **A**eronautics **S**pace **A**dministration
NIR	**N**ear **I**nfra **R**ed
PAPER	**P**recision **A**rray for **P**robing the **E**poch of **R**eionization
PSF	**P**oint **S**pread **F**unction
PyBDSM	**Py**thon **B**lob **D**etection and **S**ource **M**easurement
RA	**R**ight **A**scension
RFI	**R**adio **F**requency **I**nterference
RIME	**R**adio **I**nterferometry **M**easurement **E**quation
RMS	**R**oot **M**ean **S**quare
SNR	**S**ignal-to-**N**oise **R**atio
TEC	**T**otal **E**lectron **C**ontent
VLBA	**V**ery **L**ong **B**aseline **A**rray
VLBI	**V**ery **L**ong **B**aseline **I**nterferometry
UKIDSS	**UK**IRT **I**nfrared **D**eep **S**ky **S**urvey
WFC3	**W**ide **F**ield **C**amera3
XMM	**X**-ray **M**ulti-Mirror **M**ission

Physical Constants

Speed of Light	c	$=$	$2.997\ 924\ 58 \times 10^{8}$ ms^{-1}
Boltzmann's Constant	k_B	$=$	$1.380\ 648\ 52 \times 10^{-23}$ m^2 kg /(s^2 K) (exact)
Solar Mass	$\mathrm{M}_\odot$	$=$	$(1.98855 \pm 0.00025) \times 10^{30}$ kg

Symbols

a	distance	m
P	power	W (Js^{-1})
$T_{\rm B}$	brightness temperature	K
ν	frequency	Hertz
L_ν	luminosity	W Hz^{-1}
D_L	luminosity distance	m or Mpc
S_ν	flux density	W m^{-1} Hz^{-1} or Jy
$\Delta\nu$	bandwidth	Hertz
I_ν	intensity or brightness	Watts/m^2
ω	angular frequency	$rads^{-1}$
θ	angular resolution	degree or arcsec
λ	wavelength	cm

This work is dedicated to the entire Akoto-Danso and Baidoo families whose immense support, prayer and encouragement has made it possible to achieve success in all my endeavours. I also dedicate this work to my wife, Audrey Marian Akoto-Danso and my two lovely daughters, Nasya and Ann-Hallel. Lastly, I dedicate this thesis to my mother Florence Ntow Akonnor and to the memory of my late Dad, Mr. Yaw Akoto-Danso.

Chapter 1

INTRODUCTION

Astronomical surveys of the sky often lead to discoveries of new objects, promote their investigation and consequently provide new insights into their morphology and astrophysical properties. Radio surveys of extragalactic sources provide additional unique information on the nature of astronomical and astrophysical phenomena in AGN. Very Long Baseline Interferometry (VLBI, see Section 1.3) has significant advantages in this regard due to its high angular resolution. Traditional VLBI observations, however, have comparatively small fields of view, which has largely restricted VLBI to targeted observations of bright sources in the half century that the VLBI technique has been used.

Surveys using VLBI arrays have only just become more practical (through innovation in correlation techniques) however, the software used to image such datasets still depends on a few decade-old algorithms and software packages. This project is focused on using new algorithms and techniques in calibration and imaging to develop a wide-field VLBI pipeline for current arrays, as well as the upcoming African VLBI Network and eventually the SKA.

In this chapter, a brief introduction to radio astronomy and the fundamental concepts of flux density and brightness temperature is provided. The sections that follow include a brief discussion on emission mechanisms, followed by a summary of the types of sources observed in radio astronomy. A detailed overview of the radio interferometry and aperture synthesis is reviewed after that. The researcher then proceed to give an overview of VLBI, review of past and future VLBI surveys and VLBI science. Lastly, the objectives for this work is presented.

1.1 Introduction to Radio Astronomy

Radio Astronomy is the study of radio emission from celestial objects or sources. The range of radio frequencies spans from approximately 1 MHz to 1 THz, which corresponds with

the low end of the electromagnetic spectrum. All objects emit some sort of radio waves through various mechanisms (Rohlfs & Wilson, 2013). As these radio waves travel through one point to the other they interact with the surrounding medium through the electric and magnetic fields. The regularly repetitive changes in these fields produce radio waves. The radio waves transport energy from one point to the other through space at the speed of light (in a vacuum).

Figure 1.1 shows the electromagnetic (EM) spectrum. It can be seen that radio waves cover a wide range of wavelengths compared to the others in the EM spectrum, however, can in principle be divided into mm,sub-mm, cm and m astronomy.

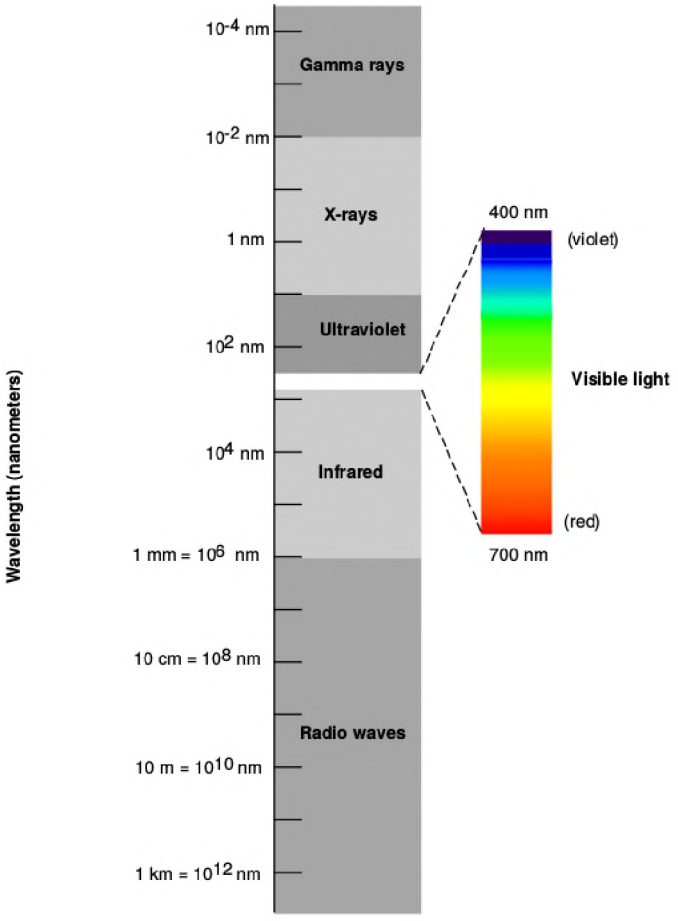

FIGURE 1.1: Electromagnetic spectrum. Credit: Miller (1998).

Radio waves have the longest wavelengths in the electromagnetic spectrum. Radio telescopes probe different astrophysical phenomena when compared to other wavelengths. These include lowest to highest energies, lowest to highest densities and among the weakest to the strongest magnetic fields.

Definitions of terms in fundamental radio astronomy is presented in the next section.

1.1.1 Brightness Temperature and Flux Density

Let's consider bundles of rays travelling on a linear path through a medium. These rays subtend an infinitesimal solid angle $d\Omega$, through an infinitesimal area element dA across an infinitesimal frequency width, $d\nu$. The energy carried through dA by the bundle of rays as can be seen in Figure 1.2 is given by

$$dE = I_\nu dA dt d\Omega d\nu \ , \tag{1.1}$$

where I_ν is the intensity (brightness) with units of $\mathrm{Wm^{-2}sr^{-1}Hz^{-1}}$.

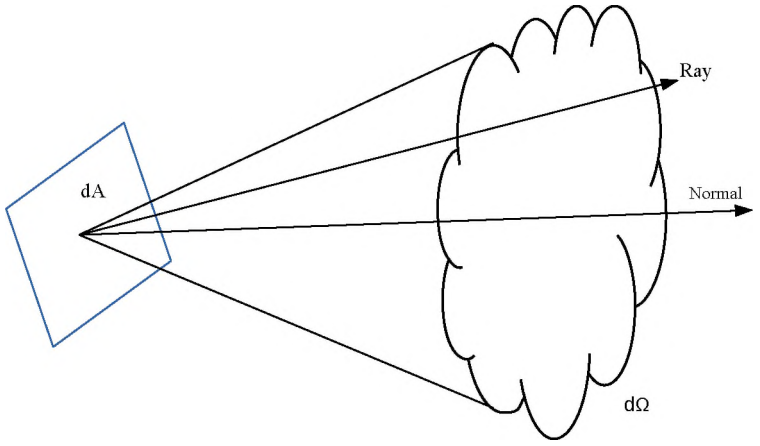

FIGURE 1.2: Schematic demonstration of intensity or brightness of a solid angle and a surface area. dA is normal to the source.

The specific intensity, I_ν defines the measure of radiated energy flow per unit area A, with time t, solid angle Ω and spectral frequency ν. Note that I_ν is also the power density, defined as the power per unit area, per unit solid angle, per unit bandwidth.

The flux density S_ν is defined as the quantity of incoming radiation energy through a cross-section of unit area, per unit frequency bandwidth, and per unit time. If a source subtends a well-defined angle then its flux density integrated over the solid angle is defined as

$$S_\nu = \int_{\text{source}} I_\nu(\theta, \phi) \cos\theta d\Omega \ , \tag{1.2}$$

where θ is the angle between a 'ray' of radiation.

Given that the angular size of the source is $\ll 1$ radian, then $\cos\theta \approx 1$ and so Equation 1.2 can be simplified to

$$S_\nu \approx \int_{\text{source}} I_\nu(\theta, \phi) d\Omega \ . \tag{1.3}$$

The distinction between the specific intensity or brightness and flux density of a source is that intensity is an intrinsic property of the source and is independent of the source's distance, whereas the flux density is dependent on the distance ($S_\nu \propto d^{-2}$) of the source and the observer.

In observational cosmology, the most important relationship is that between flux density and luminosity.

The specific luminosity of an astronomical object is defined as the amount of energy emitted by an astronomical object in a fixed time per unit bandwidth at a specified frequency interval. In contrast, the bolometric luminosity of an object is the specific luminosity (energy emission) integrated over all frequencies (or wavelengths). Luminosity alone can be an essential discriminant as to the astrophysical nature of a given radio source. For example, most sources with luminosity cores ($L_{1.4\text{GHz}} > 2.0 \times 10^{21}$ W/Hz) are classified as AGN, while those with lower radio luminosity cores are classified as starburst, as stated by Condon et al. (2002). Astronomers sometimes prefer to quote the luminosity by comparing it to the Sun's luminosity, which is $\sim 3.9 \times 10^{26}$ Watts.

In more general terms, for sources at cosmological distances, the full expression for radio luminosity (Sadler et al., 2002), assuming the emission is isotropic (Pracy et al., 2016), is given by

$$L_\nu = \frac{4\pi D_{\text{L}}^2 S_\nu}{(1+z)^{1+\alpha}} \ , \tag{1.4}$$

where z is the redshift and α is the spectral index ($\alpha = 0.7$, see Equation 1.5) . The above formulation (Equation 1.4) is as a result of the expansion of the Universe taken into account when calculating cosmological distances.

The spectral index (Randall et al., 2012) of a source is defined as

$$\frac{S_{\nu 2}}{S_{\nu 1}} = \left(\frac{\nu_2}{\nu_1}\right)^\alpha \ , \tag{1.5}$$

where $S_{\nu 1}$ and $S_{\nu 2}$ are the flux densities at frequencies ν_1 and ν_2 respectively.

The spectral index of the source gives an indication of its properties and the type of emission mechanism of the source. In the Rayleigh-Jeans regime, most non-thermal radio sources have spectral index in the range $-0.5 < \alpha < -1.5$ while that of thermal radio sources are typically $\alpha \geq 0$ (Sasao & Fletcher, 2005; Kraus, 1966). In other words, for thermal sources, the flux density of the radio sources increases or stays constant (especially when considering ionised sources) with increasing frequency (decreasing wavelengths), whereas for non-thermal radio sources, the reverse is true.

The brightness temperature, $T_{\rm B}$, of a source with intensity I_ν, is defined mathematically as

$$T_{\rm B} = \frac{c^2}{2k\nu^2} I_\nu \ , \tag{1.6}$$

where ν is the frequency, c is the speed of light, k is the Boltzmann's constant and I_ν is the source intensity. The expression of the brightness temperature (Equation 1.6) is an approximation to the Planck's Law, and is only valid where $h\nu \ll kT$.

A blackbody is a body which absorbs all radiation incident upon it. The brightness temperature is defined as the equivalent or effective temperature of a blackbody which radiates the same monochromatic intensity as the object at a given frequency (Miller, 1998).

If incoming radiation emanates from a sufficiently hot ($T_{\rm B} \geqslant$1 K) thermal source, without absorption or emission along the path of propagation, then $T_{\rm B}$ must correspond to the physical temperature, however, if the source is non-thermal, then $T_{\rm B}$ has little relevance to any real temperature. For example, non-thermal sources, such as masers and synchrotron sources, can have very high brightness temperatures (from 10^9 K for methanol masers to 6×10^{12} K for OH masers, and 10^{15} K for water masers.). In pulsars, for example, the brightness temperature can reach $> 10^{26}$ K (Kardashev & Slysh, 1988), whereas quasars at 5 GHz can have $T_{\rm B}$ of $\sim 10^{12}$ K (Tingay et al., 2001; Lister et al., 2011). High-resolution VLBI observations of Cygnus-A measures brightness temperature of $\sim 10^{10}$ K at 43 GHz (Krichbaum et al., 1998).

To put this into a more practical perspective, the brightness temperature in the rest-frame is related to the flux density by the relation

$$T_{\rm B} = \left(\frac{S_\nu}{\Omega_{\rm A}}\right) \frac{\lambda^2}{2k} \ , \tag{1.7}$$

where $\Omega_{\rm A}$ is solid angle of the source and λ is the wavelength the emitted wavelength which is dependent on redshift. Since the values of λ is fixed and k is a constant, for a given

observation it can be formulated from Equation 1.7 the relation

$$T_{\rm B} \propto \frac{S_\nu}{\Omega_{\rm A}} \tag{1.8}$$

$$T_{\rm B} = \frac{2\ln(2)}{\pi}\frac{c^2}{k}\frac{S_\nu(1+z)}{\nu^2 ab}\ , \tag{1.9}$$

where $T_{\rm B}$ has units of Kelvin, ν is the observing frequency in Hz, S_ν represents the flux density measured in Jy, a and b are the major and minor axes of the beam, respectively, in milli-arcseconds, and $(1+z)$ accounts for the cosmological effect on the brightness temperature.

From the above formulation, the brightness temperature for an AGN can be deduced if the angular sizes (solid angle, Ω), redshift (z) and the flux density are known.

It is however pertinent to mention that there is a brightness temperature limit of $T_{\rm B} \approx 1.0 \times 10^{12}$ K (Kellermann & Pauliny-Toth, 1981; Kellermann et al., 1998) known as inverse Compton limit (Readhead, 1994) in radio cores which occur as a result of inverse Compton cooling. The observation of compact radio cores with $T_{\rm B}$ exceeding the inverse Compton limit on the basis of their time variability is direct evidence of relativistic beaming (Readhead, 1994; Agudo et al., 2006) and this results in an Inverse Compton Catastrophe (Readhead, 1994).

Conversely, for a given flux density, the brightness temperature, $T_{\rm B}$, is proportional to $(\frac{\lambda}{\theta})^2$. This is because the resolution, θ, is proportional to $\frac{\lambda}{D}$. Therefore the maximum brightness temperature that can be measured by an interferometer depends only on the flux density and the baseline (Kellermann & Moran, Kellermann & Moran). Thus, the minimum detectable brightness temperature using the derivation by Thompson et al. (2017) is given by

$$(T_{\rm B})_{\rm min} = \frac{2}{\pi k} D^2 (S_\nu)_{\rm min}\ , \tag{1.10}$$

where D is the minimum baseline length of the array.

Given the limitations of the brightness temperature sensitivity, observations of thermal phenomena occurring in stars, compact regions of HII and molecular clouds are generally not feasible in VLBI (Walker, 1999). Typically, the brightness temperature sensitivity, $(T_{\rm B})_{\rm min}$, for a ∼8 hr observation with the VLBA at a wavelength of 18 cm, with a baseline of 8000 km, and with an image sensitivity of 11 μJy beam^{-1} is $(T_{\rm B})_{\rm min} \approx 10^5$ K.

One importance of brightness temperature is that it is a good diagnostic for determining the type of emission process in compact radio sources. Next, a discussion on the types of emission mechanisms is given.

1.1.2 Emission mechanisms

Electromagnetic radiation is typically produced as a result of accelerated charged particles- that is to say, they change either the speed and/or direction of their motion. There are two types of emission that result from their motion, namely, continuum emission and spectral line emission.

- Continuum emission: this is emission over a vast range of frequencies due to the acceleration of charged particles moving with a wide range of energies. Examples of continuum emission are thermal Bremsstrahlung, synchrotron radiation and thermal emission from galactic dust.
- Spectral line emission: this is produced as a result of emission of radiation at frequencies which correspond to the photon energy of the atoms or molecules that constitute the object observed. Examples of these types of emission are neutral hydrogen (HI) line or 21 cm hyperfine line, recombination lines of ionised hydrogen and heavier atoms. Specifically, radio line emission is useful in giving diagnostic analysis in the astrophysical properties of the radio sources. This is because the line strength, widths and emission profiles are powerful tools which are used to determine the physical conditions (e.g., density and relative abundance) and the kinematic state of the gas associated with the astrophysical objects (Garrett, 2015; Chevalier & Fransson, 2016).

This thesis will focus on a continuum survey. Sources of continuum emission can be subclassified into thermal and non-thermal processes. Brief descriptions of these emission processes is presented in the following subsections.

1.1.2.1 Thermal Emission

In general, accelerating charged particles (e.g., electrons in atoms) emit electromagnetic radiation, thus all objects with temperatures above zero [1] emit thermal radiation. Thermal emission is the emission of electrons which are dependent only on the temperature of the emitting object (black body radiation). In thermal emission processes, the energy distribution

[1] Absolute Zero =0 K = -273^{o}C

of the electrons involved can be described by the Maxwell-Boltzmann law (Garrett, 2015). The radiation from a black body in thermal equilibrium can thus be described by the Planck law (De Becker, 2007):

$$B_\nu(T) = \frac{2\mathrm{h}\nu^3}{\mathrm{c}^2}\frac{1}{e^{\mathrm{h}\nu/\mathrm{kT}}-1}[\mathrm{W.m^{-2}.sr^{-1}.Hz^{-1}}] \ , \tag{1.11}$$

where B_ν is the intensity, ν is the observing frequency, T is the temperature, c is the speed of light and h is the Planck constant.

In the radio spectrum, where $h\nu \ll \mathrm{k}T$, Planck's law reduces to the Rayleigh-Jeans approximation:

$$B_\nu(T) = \frac{2\nu^2\mathrm{k}T}{\mathrm{c}^2} \ . \tag{1.12}$$

The intensity of the radiation is completely described by T and so $\mathrm{k}T$ has units of energy. Hence, the intensity of the radiation emitted by a black body is given by $S_\nu = B_\nu(T)$.

The major type of thermal emission is free-free or thermal Bremsstrahlung. The thermal Bremsstrahlung mechanism involves the emission of photons by electrons due to acceleration caused by electrostatic interactions between electrons and ions. Details of the mathematical derivations are found in (Rohlfs & Wilson, 2013). Bremsstrahlung emission accounts for nearly 10% (Condon & Ransom, Condon & Ransom) of the 1 GHz continuum luminosity in most spiral galaxies and is the strongest component in the frequency range 30 GHz$\lesssim \nu \lesssim$ 200 GHz (Condon & Ransom, Condon & Ransom).

1.1.2.2 Non-thermal Emission

Non-thermal emission is emission whose emitted radiation is not dependent on the temperature of the sources or emitting body. In the next two subsections, details of the nature of these types of emission is given.

1.1.2.2.1 Synchrotron Emission

Synchrotron emission is generated by charged particles gyrating around magnetic field lines at relativistic speeds (Burke & Graham-Smith, Burke & Graham-Smith). Larmor's formula gives the total emitted power from the charged particles

$$P_\mathrm{S} = \frac{2q^2}{3\mathrm{c}^3}|\dot{\mathbf{v}}|^2 \ , \tag{1.13}$$

where q is the charge of the particle, $\dot{\mathbf{v}}$ is the acceleration in the instantaneous rest-frame.

In the relativistic scenario, the energy emitted does not only depend on the magnetic field alone but also on the energy of the particles (Kellermann & Pauliny-Toth, 1981; Petrosian et al., 2008). This type of radiation is not only important at radio wavelengths, but it is also observed in AGN at infrared (IR), optical, ultraviolet (UV) and X-ray wavelengths. Thus, a knowledge of synchrotron emission is essential for the study of AGNs.

Synchrotron emission is observed in astronomical sources such as supernovae and supernovae remnants (e.g., the Crab Nebula in the Milky Way- Garrett, 2015), jets of compact radio sources, galaxies and cluster halos.

1.1.2.2.2 Inverse Compton Scattering

In this emission process, higher-energy photons are produced by relativistic electrons through a scattering of lower-energy photons by higher-energy electrons. The process is called inverse Compton scattering because the relativistic electrons lose their energy rather than gaining while the low energy photons rather gain energy. Thus, the emitted power in this process is given by

$$\langle P_{\rm IC} \rangle = \frac{4}{3}\sigma_{\rm T} {\rm c} \gamma^2 \beta^2 u_{\rm rad} \ , \tag{1.14}$$

where $u_{\rm rad}$ is the energy density of the radiation field, $\gamma = E/mc^2$ is the Lorentz factor, $\beta = v/{\rm c}$, v is the speed of the electrons, ${\rm c}$ is the speed of light and $\sigma_{\rm T}$ is the Thomson cross-section.

For instance, in a compact synchrotron source, emitted photons can be inverse Compton scattered by the relativistic electrons. This process gives the photon a boost in energy by a factor of γ^2. The emergent radiation is therefore termed synchrotron self-Compton emission. Thus, as long as there are available relativistic electrons, photons generated by the synchrotron process can be scattered into the optical region and beyond by the inverse Compton process. This activity eventually leads to the inverse Compton catastrophe if $T_{\rm b} > 10^{12}$ K (if the power of inverse Compton emission exceeds the synchrotron emission).

The above-stated emission mechanisms are essential for the study of the most exotic regions of the Universe. The understanding of these mechanisms enables researchers to probe their behaviour, analyse the spectrum from distant astronomical sources and obtain the detailed information regarding the astrophysical conditions present in the regions of the Universe where this radiation traversed from. Moreover, the emission processes provide a fundamental

explanation for continuum spectrum of most galactic and extragalactic sources observed in the radio spectrum.

In the next section, summary of the sources which emit some of the emission mechanisms described in this section is presented.

1.1.3 Astrophysical Radio Sources

Radio sources are astronomical objects that emit radio waves. This radio emission is emitted from a wide range of sources. A summary of some of the radio sources; supernovae and supernovae remnants, radio galaxies, blazars and Seyfert galaxies are thus given below.

1.1.3.1 Supernovae and Supernovae Remnants

A supernova (SN) is simply the explosion of a star, which is one of the most energetic single events in the Universe as stated by Bartel (2009). Supernovae result in the emission of vast amounts of various types of radiation: ultraviolet, infrared, X-ray, gamma-rays and radio waves. In general, there are two main types of supernova, namely, Type I and Type II supernovae. Earlier observations by Greenstein & Minkowski (1973) and Kirshner et al. (1973) postulated that there are two major optical spectroscopic distinguishable differences between these supernovae:

- Type I supernovae (SN I) exhibit no hydrogen lines in their optical spectra, whereas in Type II supernovae (SN II), these hydrogen lines are present (van den Bergh & Tammann, 1991),
- Type I supernovae are typically the only type observed in elliptical galaxies, while Type II supernovae only occur in spiral and irregular galaxies (van den Bergh & Tammann, 1991).

There were, however, doubts about the classification scheme outlined above. This is because some Type I supernovae show many of the characteristics of Type II supernovae (e.g., Type Ib and Type Ic). Secondly, the classification was challenged on the basis that two types of supernovae could produce three distinct kinds of young supernovae remnants, as stated by van den Bergh & Tammann (1991).

Recent research has led to the refinement of the types of supernovae based on the types of stars that give rise to the supernovae. It is now accepted that there are two main types of

explosion mechanisms that produce supernovae, namely, core-collapse (Woosley & Weaver, 1986; van den Bergh & Tammann, 1991) and thermonuclear explosion (Woosley et al., 2002). Type II (Bietenholz et al., 2012), Type Ib (has strong He I absorption) and Type Ic supernovae (no He I and absent or weak Si I absorption; Bietenholz et al. 2010) are produced as a result of a catastrophic collapse of the core of a massive star. The Type Ia supernova (strong Si I absorption; Hillebrandt & Niemeyer 2000; Maoz et al. 2014) is produced as a result of a thermonuclear explosion that disintegrates a white dwarf star (Woosley & Weaver, 1986). Details of these two explosion mechanisms can be found in (Woosley & Weaver, 1986; Weiler et al., 1986; Weiler & Sramek, Weiler & Sramek; Weiler et al., 2007).

A supernova remnant is a structure resulting from the explosion of a star in a supernova. The explosion occurs when a supernova triggers a shock wave which ejects and heats the surrounding circumstellar material (CSM) and interstellar medium (ISM), forming a supernova remnant. There are distinct prototypical examples of the different supernovae that have been observed in our own Galaxy in the last millennium- SN 1006; SN 1054 which gave rise to Crab Nebula; SN 1181, which is associated with the supernova remnant 3C58; Tycho's supernova of 1572 (Minkowski, 1964; Woltjer, 1972); Kepler's supernova of 1604 and Cassiopeia A.

Radio emission in a supernova is generated by the shocks formed as a result of the interaction of the ejecta with the CSM. Radio emission, therefore, traces the fastest ejecta, unlike the optical emission, which traces massive but slowly-moving bulk ejecta (Bietenholz et al., 2010). Secondly, radio observations can be used to determine the distribution of supernovae remnants through the Galaxy[2].

Numerous supernovae that are observed in external galaxies resolving the supernovae in the first few decades of their life, however, require milli-arcsecond (mas) resolution. Thus, VLBI observations provide the most direct way of measuring the expansion velocity of the shock front which is a fundamental characteristic for distinguishing different supernovae (Bietenholz, 2008; Bietenholz et al., 2012). Secondly, the size and perhaps the geometry of the radio emission region of supernovae can be measured and this can only be done using VLBI (Bietenholz et al., 2012).

It is noteworthy that only supernovae with relatively dense CSM produce detectable radio emission and so far, only core-collapse supernovae; Type Ib/c and Type II, can be studied with the VLBI (Bartel, 2009; Bartel & Bietenholz, 2003).

Additionally, VLBI studies of supernovae is a unique tool for directly measuring the supernovae rate, and thus star formation rate, in star-forming regions, which typically are highly obscured in the optical spectrum of the EM (Bietenholz, 2005, 2008). Specifically, the

[2]The Galaxy is composed of a massive collection of stars, planets, and other astronomical objects.

observed rate at which massive stars ($M \gtrsim 8\ M_{\odot}$;Woosley & Weaver 1986) die due to core-collapse supernovae (CCSNe), can be used as a direct measure of the current star formation rate (SFR) in galaxies and provides unique information on the initial mass function (IMF) of massive stars (Pérez-Torres et al., 2009; Wang et al., 2015). This is made possible because VLBI, which provides high angular resolution of few milli-arcsecond at cm-wavelengths, can detect individual radio supernovae at vast distances in the local Universe.

No radio emission has yet been detected from Type Ia supernovae (Wang et al., 2015). Potentially, the increased sensitivity of the SKA in addition to a global VLBI array, particularly in the southern hemisphere, will allow detection of many more supernovae and also conduct follow-up of individual supernovae for much longer (Bietenholz, 2008; Wang et al., 2015).

Having described the radio source (supernovae; Section 1.1.3.1) above, the dominant type of extragalactic radio sources detected with current VLBI arrays; AGNs, are summarised in the next sections.

1.1.3.2 Active Galactic Nuclei

An AGN is a compact region located at the centre of approximately 10% of active galaxies (Treister et al., 2012). An AGN contains a massive ($> 10^5\,M_{\odot}$) accreting black hole (BH) whose luminosity ($L_{\rm bol} > 10^{46}$ erg/s) rivals or even surpasses its host galaxy, and sometimes dominates the emission such that the host galaxy is obscured. An AGN is believed to be the most luminous persistent source of electromagnetic radiation in the Universe, as stated by Loh (Loh). AGNs emit largely non-thermal radiation from the BH accretion disk (Kormendy & Ho, 2013). Another characteristic of an AGN is that the supermassive black hole (BH) at its centre has gravitational potential energy which is the ultimate source of its luminosity. AGNs are powerful energy sources and principal probes of the Universe, hence understanding them is essential to studying the formation and evolution of the Universe. AGN can be classified into two physically distinct classes; radio-loud (RL) and radio-quiet (RQ). The observed distinctions between them are:

1. radio-loud objects are large jets and lobes, with kinetic power of the jet being a significant fraction of the bolometric luminosity of $L_{5\rm GHz} > 10^{25}\ {\rm Wsr^{-1}Hz^{-1}}$ (Klöckner et al., 2009) while radio-quiet objects have weak radio ejecta ($L_{5\rm GHz} < 10^{24}$ ${\rm Wsr^{-1}Hz^{-1}}$) and are energetically insignificant (Fanaroff & Riley, 1974)

2. radio-loud AGN are typically associated with elliptical galaxies which have undergone recent mergers (Chiaberge et al., 2015) while radio-quiet AGN are typically associated with spiral galaxies and

3. the space density of radio-quiet AGN at a given optical luminosity is ≈ 10 times higher than that of a radio-loud AGN (Heckman & Best, 2014).

Despite the differences between the radio-loud and radio-quiet AGN, both are associated with non-thermal emission (Chiaberge et al., 2015). An AGN is typically classified using the unified model. The unified model of the AGN is shown in Figure 1.3.

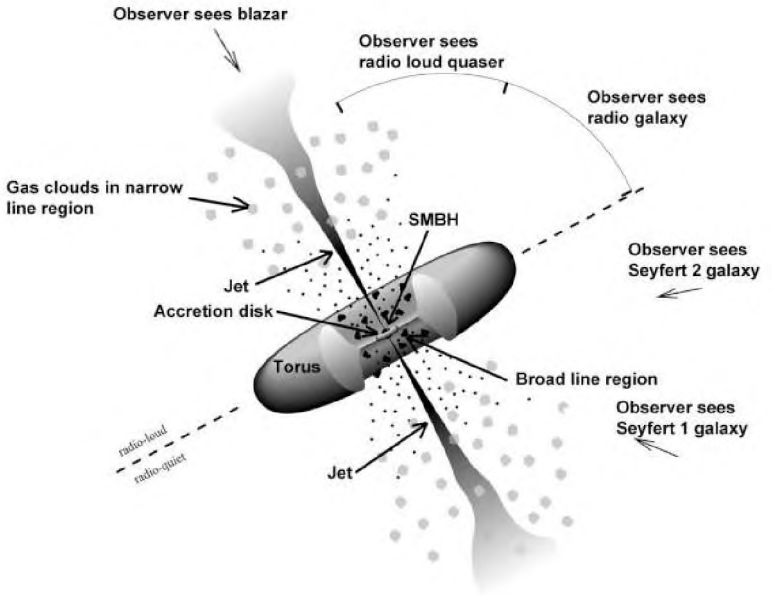

FIGURE 1.3: This shows the main features of a "unified model" for active galactic nuclei. Image Credit: Robert Findlay.

According to Netzer (2013) an object is classified as AGN if it fulfils at least one of the following criteria:

1. It contains a compact nuclear region much brighter than a region of the same size in a normal galaxy.
2. It shows clear signature of non-stellar (non-thermal) continuum emitting process in its centre.
3. It shows strong emission lines.
4. It shows variability in line and/or continuum emission on relatively short timescales.

Based upon the viewing angles from the unified model, the observed spectra will appear different leading to the different classification of these objects. The sub-classification of radio sources as AGNs in the unified model presented in Figure 1.3 into various groups is directly

related to one of the preceding four criteria. For example, radio galaxies are AGNs because of point 2, LINERS and blazer are AGNs because of point 3 and point 4 respectively. A summary of these objects is given in the next four subsections.

1.1.3.2.1 Radio Galaxies

Radio galaxies are radio emitters driven by non-thermal emission. Local Universe archetypes include Centaurus A (Müller et al., 2011, 2014) and Messier 87 (Chang et al., 2010). The host galaxies are typically large elliptical galaxies. Radio galaxies are sometimes defined as galaxies with luminosity or power, $L_{1.4\mathrm{GHz}} > 2 \times 10^{23}$ WHz^{-1} (Fanaroff & Riley, 1974; van Velzen et al., 2014). There are varieties of morphologies of radio galaxies but the basic division in structure types of Fanaroff and Riley classification (Fanaroff & Riley, 1974) has stood the test of time.The underlying principle of the Fanaroff and Riley classification is that radio sources have two basic morphological types, which is based entirely on radio structures that exist on large-scale radio morphology, from few to several hundred kilo-parsec to Mega-parsec. The basic types are the FR I and FR II galaxies, and the following are the essential differences between them:

- Edge-darkened FR I type radio galaxies have lower radio luminosities ($L_{1.4\mathrm{GHz}}$<10^{25} W Hz^{-1}) whereas the edge-brightened FR II type radio galaxies have higher radio luminosities. The value of the radio luminosities transition is dependent largely on the host galaxies as it tends to increase with the host optical luminosities (Saripalli, 2012; de Gasperin, 2017).
- The orientation of the magnetic field of FR I galaxies is often perpendicular to the jet apart from the inner regions while that of FR II galaxies have a magnetic field which is parallel to the jet (Bridle, 1984).
- The jets in FR II radio galaxies are generally smooth, mostly one-sided and have hotspots at the ends in well-separated lobes; FR I galaxies, however, are two-sided with radio structures which are often distorted and plum-like (Kembhavi & Narlikar, 1999). The smooth FR II jets are thought to be indicative of highly supersonic flows, while FR I jets have subsonic flows, which makes them susceptible to distortions in interaction with the ambient medium (Laing & Bridle, 2013). This problem arises because the jets in the radio galaxies are postulated to be produced in similar central engines, which emerge with supersonic speeds from the engine and are then slowed down to subsonic speeds when there is sufficient interaction.

Although there are other source morphological classification types, they are understood within the Fanaroff-Riley classifications as stated by Saripalli (2012). For example, the taxonomic classification approach to radio morphological classification attempts to recognise recurrent patterns that could provide useful phenomenological information about the emission mechanisms involved, as stated by Miley (1980). The taxonomic classification approach to studying the morphological difference in radio galaxies is based on three gross structure properties, namely; bending at the outer extremities, edge-brightening and rotational symmetry (Miley, 1980).

1.1.3.2.2 Blazars

Blazars are radio-loud AGN which are highly polarised, have high luminosity, and show highly variable time characteristics. Blazars are also compact, flat-spectrum [3] radio sources with continuum emission distinguished by relativistic jets orientated close to the observer (Sambruna et al., 1996; Urry, 1999; Giroletti et al., 2004). Blazars show luminosity variations across the electromagnetic spectrum (Ojha et al., 2010; Piner et al., 2010; Taylor, 2010) and are one of the most energetic objects found in the Universe (Karamanavis et al., 2016). The main classes of blazars are BL Lacertae and Flat-spectrum radio quasars (FSRQs). A brief description of the differences between the FSRQs and BL Lacertae groups will be given in the next paragraph.

The distinguishing characteristic of FSRQ from BL Lac objects is that they have strong and broad optical emission lines, while the BL Lac objects reveal no emission lines or have weak emission lines. Secondly, FSRQs have higher luminosities than the BL Lacs (Sambruna et al., 1996). Also, on average, FSRQ have a lower polarised radio and optical emission than the BL Lac objects (Padovani, 2016).

VLBI monitoring of blazars provide the only direct measure of relativistic motion in AGN jets, and this allows calculation of intrinsic jet properties like jet speed, doppler factor, opening and inclination angles (Ojha et al., 2010). Secondly, VLBI monitoring of blazars provides the possibility of identifying the location and extent of emission regions (Ojha et al., 2010), specifically concerning gamma-rays (e.g., Taylor 2010; Agudo et al. 2011).

1.1.3.2.3 Seyfert Galaxies

Seyfert galaxies are low luminosity ($M_{\rm B} > -21.51 + 5{\rm log}h_o$[4]) AGN with quasar-like nucleus

[3] A flat spectrum is defined as satisfying $\alpha > -0.5$, with $S_\nu \propto \nu^\alpha$.

[4] $h_o = \frac{d}{10}$, where d is the luminosity distance in parsec.

except that the host galaxy is detectable. Seyfert galaxies are characterised by spiral-like morphologies with point-like nuclei in the centre and show non-thermal continuum. Seyfert galaxies form about 10% of galaxies and are among some of the most studied astronomical objects in astronomy (Maiolino & Rieke, 1995). Seyfert galaxies have supermassive black holes at their centres and are classified into two subclasses;

- Type 1 Seyfert galaxy typically have two sets of emission lines, superimposed on each other and has lower luminosities ($L < 2 \times 10^{11} L_{\odot}$) and ais seen nearby, where its host galaxies can be resolved (Urry & Padovani, 1995). These are the 'broad lines' and 'narrow lines'. These two sets of emission stem from the broad and narrow line regions respectively. The former is closer to the SMBH (size of BLR[5] is ∼10-100 light days; Wandel et al. 1999; Kaspi et al. 2000) and has high velocities (2000-10,000kms^{-1}; Netzer 2013) but is more easily obscured by the central torus. The latter extends further away from the black hole (size of NLR is ∼1000-5000pc; Bennert et al. 2006), beyond the dusty torus and is therefore mostly unobscured and has a narrower emission line width due to lower velocities (1200 kms^{-1}; Netzer 2013). Type 2 Seyfert galaxies have narrow lines.
- Type 2 Seyfert galaxy has weak continuum and no broad emission lines because the broad line region is obscured from view by a dust torus or by absorbing clouds (Urry & Padovani, 1995).

Seyfert galaxies provide avenues to study the interplay between AGN activity and their host galaxy properties, since the host galaxy is visible in these systems (LaMassa, 2011) and have comparable luminosity.

1.1.3.2.4 Quasars

Quasars are visible at large cosmological distances and so they have high luminosity ($L > 2.0 \times 10^{11} L_{\odot}$). The flux densities of quasars have short timescale variability (as short as hours) and this indicates that their enormous energy output originates from a compact region. Quasars are strong emitters at almost all wavelengths, have strong and broad emission lines of highly ionised elements (e.g., Mg, O, Ca) and these are the most distinct observational characteristics from stars and normal galaxies. Quasars also have optical spectra which are similar to Seyfert 1 galaxies while their morphology is similar to FR-II sources. The host galaxies of quasars are observed to be spirals or ellipticals. The radio emission from quasars is due to synchrotron emission from relativistic particles moving through a weak magnetic

[5]BLR is acronym for broad-line region.

field (Kellermann & Verschuur, 1988). Moreover, quasars are typically classified into radio-loud (RLQ) and radio-quiet (RQQ). Summary of these sources is found in (Antonucci, 1993; Netzer, 2015; Blandford et al., 1990) and will not be discussed here.

It is worth mentioning that understanding the nature of energetic cores of sources such as quasars and galaxies are crucial for unravelling the origin and evolution of the objects in which they reside (Preston et al., 1985). High-redshift quasars (HRQs) have significant importance for galactic studies and cosmology because they provide essential information on supermassive black hole growth and accretion processes of AGNs (Zhang et al., 2017).

1.1.3.3 Star-Forming Galaxies

A galaxy is defined by and observed through its stellar content. The conversion of gas into stars forms an important fundamental for galaxy formation. Stars then become the building blocks for galaxy formation and this involves various astrophysical processes. In an extragalactic radio (cm) continuum survey, there exists two main populations of sources, namely, star-formating galaxies and AGN. The evolution measure of both AGN and star formation in galaxies deepens our understanding of galaxy evolution.

The past decade has seen an unprecedented number of observations which were planned towards understanding star formation on all scales. A significant number of facilities such as the *Spitzer Space Telescope*, *Herschel Space Observatory*, the Galaxy Evolution Explorer (GALEX), *Hubble Space Telescope (HST)*; and a host of ground-based telescopes in the optical, infrared (IR), submilliter and radio have been involved in this quest. These new facilities provide detailed study of the major physical and evolutional process that lead to the formation of stars in the interstellar clouds.

Radio observations, in particular, provide information on star formation in the form of atomic and molecular gas, respectively revealed by 21-cm and cm-to-submillimetre radio observations. At frequencies of 1.4 GHz, flux densities ≥ 50 mJy, about 95% of sources are identified as AGN (classical radio galaxies), while below this flux density, there is an increasing number of star-forming galaxies as stated by Condon (1989). High angular resolution instruments such as the VLBI, therefore holds a unique advantage to disentangle AGN from star formation emission particularly at high redshifts.

Star-forming galaxies can be classified using the type of emission. The radio luminosity of star-forming galaxies can be typically be explained by synchrotron radiation from supernovae remnants which are produced at the rate less than about $\frac{1}{\mathrm{yr}}$. Most of the episodic bursts of star formation are apparently triggered by galaxy-galaxy interaction. Star-forming galaxies are also strong radio surveys in bright spiral galaxies. Radio continuum observations such as

the VLBI can thus provide key information on star formation, particularly via an unbiased unobscured dust measurement of star formation rate.

These quests to unearth the formation of stars in the interstellar clouds also extends the study to reach integrated measurements of star formation rates (SFR) of a significant number of distant galaxies (Kennicutt Jr et al., 2012). Star formation rate is defined as the total mass of stars formed per year, often measured in solar masses per year ($\mathrm{M}_{\odot}\mathrm{yr}^{-1}$). Based on observations over the past years, it has been accepted generally that the total SFR of a galaxy is determined by its ability to form dense molecular clouds (Mo et al., 2010). There is a tight correlation between SFR from FIR and radio continuum.

For radio continuum, SFR is calculated using equation:

$$SFR_{1.4} = \frac{L_{1.4}}{1.81 \times 10^{21}\mathrm{WHz}^{-1}}\mathrm{M}_{\odot}\mathrm{yr}^{-1} \ , \tag{1.15}$$

where $\mathrm{M}_{\odot}$ is the solar mass.

This relation (Equation A) by Condon (1992) is dervied from supernovae rate, hence the SFR can be derived directly from the radio luminosity.

Following the above outline of the types of AGN sources radio telescopes detect, a description of how these radio sources are observed and the techniques involved are presented in the next section.

1.2 Radio Interferometry and Aperture Synthesis

Radio signals from astrophysical objects or EM waves are measured with radio telescopes, which are designed to study the radio frequency portion of the EM spectrum in the same manner as optical telescopes, are used to study optical waves from astronomical objects. Radio telescopes are typically parabolic dishes, though other types exist, such as the Low-Frequency Array (LOFAR, van Haarlem et al., 2013) and the Precision Array for Probing the Epoch of Re-ionization (PAPER, Pober et al., 2013; Ali et al., 2015) which are quasi-omnidirectional antennas has been introduced for observation at low frequencies.

In the past, radio astronomy was conducted using single dish telescopes with angular resolution of order ~ 1 degree. Building larger telescopes with increased angular resolution is impractical given the longer construction time, higher cost and increased complexity in operating such large telescopes. A practical way to achieve higher angular resolution is then to build many smaller telescopes separated by distances much larger than the size of an individual antenna, which can then be connected as an interferometer array.

In simple terms, a radio interferometer consists of pairs of radio telescopes (elements) whose voltage outputs are cross-correlated. The telescopes in the array can be widely separated and connected via coaxial cables, optical fibres or transmission lines. Most of these antennas are physically connected (connected-element) whereas others such as VLBI are not. A simple example of a radio interferometer is presented in Figure 1.4. Some examples of existing connected-element interferometers are Karoo Array Telescope-7 (KAT7), MeerKAT, Very Large Array (VLA), Westerbork Synthesis Radio Telescope (WRST), and the upcoming highly sensitive Square Kilometre Array (SKA). Some VLBI arrays include the European VLBI Network (EVN), Korean VLBI Network (KVN), Very Long Baseline Array (VLBA), and the upcoming African VLBI Network (AVN).

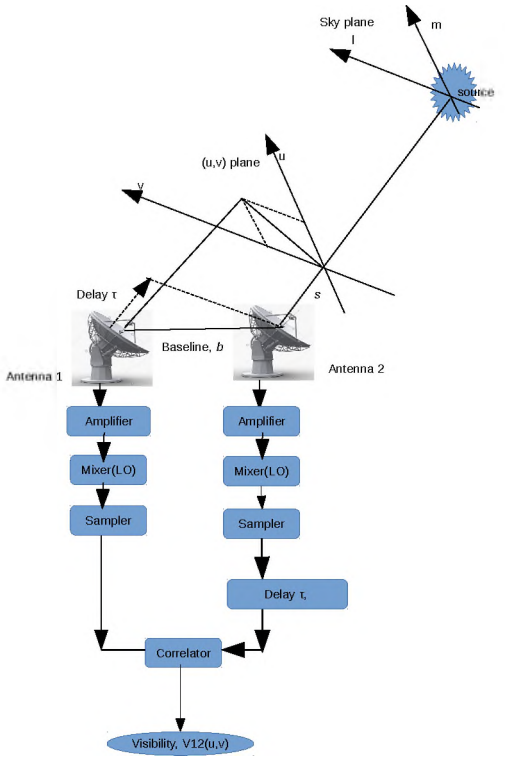

FIGURE 1.4: A two-element array demonstrating the key components of radio interferometry.

Figure 1.4 demonstrates a simple two element interferometer. As previously stated, radio telescopes detect electromagnetic radiation from various astronomical sources in the sky, which can be cross-correlated to form visibilities. By making the following assumptions, we can derive mathematical equations for the output of the above two-element interferometer:

- the distance d, to the sources is much larger than the physical separation **b** between antenna 1 and 2;
- the bandwidth $\Delta\nu$ is much smaller than the observing frequency ν; and

- the wave is monochromatic (electromagnetic wave with a single frequency).

The signal from the astronomical sources is represented by electric fields, $E(\overrightarrow{r})$. The voltages v_1 and v_2 are deemed proportional to the electric field produced by the astronomical source multiplied by the complex voltage gains of antenna 1 and antenna 2. The plane electromagnetic wave of amplitude v_1 induces a voltage V_1, at antenna 1 given by

$$V_1 \propto v_1 e^{i2\pi\nu t} \ , \tag{1.16}$$

while inducing another voltage V_2 at antenna 2 given by

$$V_2 \propto v_2 e^{i2\pi\nu(t-\tau_g)} \ , \tag{1.17}$$

where $\tau_{\rm g} = \frac{\mathbf{b}.\mathbf{s}_0}{c}$ is known as the geometric delay.

Equations 1.16 and 1.17 can be rewritten in trigonometric form as

$$V_1(t) = v_1 \cos(2\pi\nu \mathrm{t}), \tag{1.18}$$

$$V_2(t) = v_2 \cos[2\pi\nu(\mathrm{t} - \tau_{\rm g})] \ . \tag{1.19}$$

These signals are then amplified, down-converted and then digitised. The signal is down-converted to a lower frequency before correlation because it is more computationally efficient to process electronic signals at lower frequencies. The digitised data are then correlated yielding

$$\begin{aligned} V_{12}(t) &= V_1(t) \, . \, V_2(t) \\ &= (v_1 \cos[2\pi\nu t]) \, . \, (v_2 \cos[2\pi\nu(t-\tau_g)]) \\ &= \frac{1}{2} v^2 \cos(2\pi\nu\tau_g) \ . \end{aligned} \tag{1.20}$$

Denoting the radio brightness or intensity by $I(\mathbf{s})$ in the direction of the unit vector $\mathbf{s}$ at a frequency ν, then the total (signal) power received in bandwidth $\Delta\nu$, from the source solid angle $d\Omega$ is given as $A(\mathbf{s})I(\mathbf{s})d\Omega$, where $A(\mathbf{s})$ is the effective collecting area of both antennae in the direction $\mathbf{s}$ of the source. Hence, the correlator output for the signal in terms of solid angles can be represented by

$$dr = A(\mathbf{s})I(\mathbf{s})\Delta\nu \cos(2\pi\nu\tau_{\rm g}) \ , \tag{1.21}$$

Integrating and writing Equation 1.21 in terms of baseline and source position will yield

$$r = \Delta\nu \int_S A(\mathbf{s}) I(\mathbf{s}) \cos \frac{2\pi\nu \mathbf{s}.\mathbf{b}}{c} \, d\Omega \ , \tag{1.22}$$

Denoting the baseline coordinates **b** by (u,v,w) and the angular coordinates of the sky which are the direction cosines measured with respect to the axes u and v by $\mathbf{s} = (l, m, \sqrt{1 - l^2 - m^2})$, then the response of the narrow band phase-track to spatially incoherent electromagnetic radiation from the far field can be expressed by the relation between the visibility function $V(u, v, w)$ and the radio brightness, $I(l, m)$ (**?**) as

$$V(u, v, w) = \iint_s \frac{A(l, m) I(l, m)}{\sqrt{1 - l^2 - m^2}} \mathrm{e}^{-2\pi i(ul + vm + w(\sqrt{1-l^2-m^2}-1))} \ dldm \ , \tag{1.23}$$

where $\sqrt{1 - l^2 - m^2}$ is the third direction cosine measured with respect to the w axis and $\frac{dldm}{\sqrt{1-l^2-m^2}}$ is equal to $d\Omega$ in Equation 1.22.

Since the observation is typically confined to the *uv* plane, $w = 0$. This leads to

$$V(u, v) = \iint_s \frac{A(l, m) I(l, m)}{\sqrt{1 - l^2 - m^2}} \mathrm{e}^{-2\pi i(ul + vm)} \ dldm \ , \tag{1.24}$$

The primary beam is typically limited to a small region of the sky (small solid angle), this implies $\sqrt{1 - l^2 - m^1} \simeq 1$. Hence Equation 1.24 is modified to

$$V(u, v) = \iint_s A(l, m) I(l, m) \mathrm{e}^{-2\pi i(ul + vm)} \ dldm \ , \tag{1.25}$$

The Fourier transform relation, therefore, suggests that the radio brightness $I(l, m)$ can be recovered from the visibility function $V(u, v)$ by merely applying the inverse Fourier transform. The inverse Fourier transform (FT) of equation 1.25 is

$$I(l, m) = \iint_s \frac{1}{A_\nu} V(u, v) \mathrm{e}^{-2\pi i(ul + vm)} \ dldm \ . \tag{1.26}$$

The above (Equation 1.26) is the fundamental relationship between the visibility function and the source brightness distribution which is the basis of radio interferometry. In the optical regime, this relationship is referred to as the van Cittert-Zernike theorem (McCutchen, 1966; Ostrovsky et al., 2009).

The visibilities obtained (equation 1.25) are functions of the source structure, source distribution, and the interferometer baseline. Secondly, each given observation of the source with a given baseline corresponds to two measures of the visibility because the sky brightness is a real function and symmetric, so a measure gives the conjugate (i.e., $V(u,v) = V(-u,-v)$) thereof as well.

The principle behind the technique of interferometry is to estimate as accurately as possible the sky brightness distribution by measuring the amplitudes and phase of the visibility function at different points of the *uv*-plane by increasing the *uv*-coverage. The *uv*-coverage is increased when the earth's rotation continuously changes the relative orientation through the *uv*-plane, building up an elliptical *uv*-track to sample the sources. The method by which this is achieved is called aperture synthesis (Guyon & Roddier, 2001; Rohlfs & Wilson, 2013; Carozzi & Woan, 2009). Details of aperture synthesis can be found in (Högbom, 1974; Levanda & Leshem, 2010; Garrett, 2012; de Vaate et al., 2014).

Thus far, interferometers and aperture synthesis where individual antennae are connected in real time by optical fibres, cables, and microwave links have been described. An extension of this scenario is VLBI, where because of the large separation of the antennae, it is impractical for physical connection.

1.3 Very Long Baseline Interferometry

Very Long Radio Interferometric (VLBI) is one of the many techniques used to observe astrophysical sources through the 'radio window'. The observations of these sources are simultaneously performed by all the radio telescopes, synthesising a telescope with the size equivalent to the maximum separation.

In VLBI, multiple radio telescopes separated by up to thousands of kilometres at different locations of the earth collect radio signals from astronomical objects. The received radio signals are recorded at each participating telescope. All the recorded data are then time-stamped using very stable and precise time signals obtained from hydrogen maser clocks at each participating station and are additionally locked onto a GPS time standard. These time-stamped data are then sent to a correlation centre by shipping or e-shipping them over secured network links for cross-correlation. The majority of electronic transfer of the raw VLBI data is transmitted from each participating station to the correlator to determine the instrumental delays and to check that each piece of equipment is working properly. At the correlator, all the recorded data from each participating stations are played back. The values of the *a priori* delay, τ_g and delay rate, $\Delta\tau_g$ are then applied to the stations' data stream.

Here, the correlator performs calculations using the cross-correlation function $R(\tau_g, \tau_m, t)$[6] or Equation 1.20 to produce the visibilities. The cross-correlation can be performed using various types of correlators such as FX, XF (Romney, 1999).

1.3.1 VLBI And Connected-Element Interferometry

The two distinctions of VLBI from the more typical connected-element radio interferometers are (a) independent clocks at each station; and (b) (inter-)continental, rather than few kilometre baselines lengths.

Secondly, the independent atmospheres of the antennas involved in VLBI can give rapid phase variations and large gradients compared to connected-element interferometers. This problem is even exacerbated by low source elevations in VLBI compared to connected-element interferometers, given the large baseline lengths. A comparison of the differences in atmospheric effect between VLBI and connected-element interferometers is shown in Figure 1.5

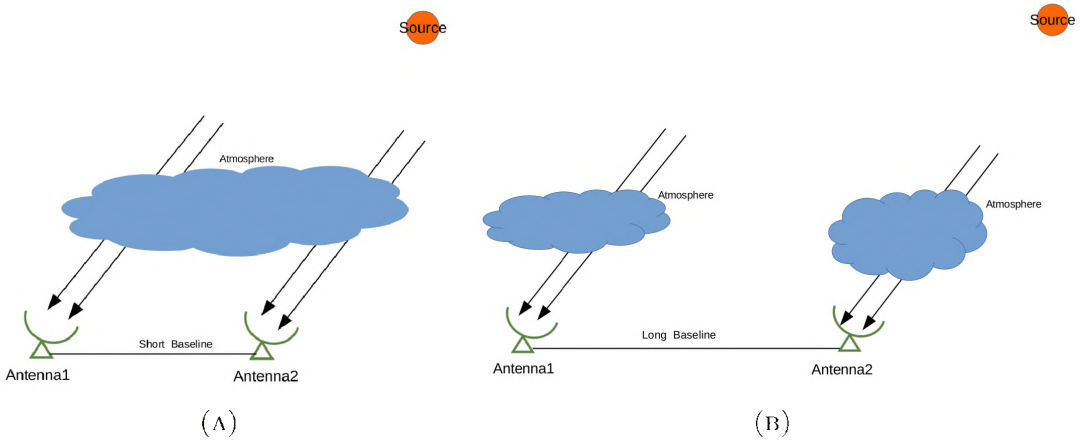

FIGURE 1.5: (a) connected-element interferometer illustrating that each antenna is affected by the same atmospheric (b) Large separation distance between the antennas in VLBI affected by different atmosphere over each antenna. The atmospheric fluctuations over each antenna cause delay errors which are more difficult to deal with in VLBI. In comparison, the delays in connected-element interferometers are minimal because almost all the antennas suffer from the same atmospheric delays.

There are also large correlation model uncertainties in VLBI when compared to connected-element interferometry on a relative scale. These uncertainties include source positions, station locations, and the earth orientation parameters (EOPs).

There are also no real absolute flux density and polarisation calibrators in VLBI in comparison with connected-element interferometers. This problem exists because most VLBI calibrator sources are resolved and more importantly, variable.

[6]The cross-correlation function, R, is given by $R(\tau_g) = \lim_{T\to\infty} \frac{1}{2T} \int_{-T}^{+T} E_1(t) E_2^{\dagger}(t - \tau_g) dt$

Having described the fundamental VLBI operational concepts, an overview of past and future VLBI surveys and the science objectives that can be achieved with the VLBI in the next three subsections is given.

1.3.2 Science With VLBI

One of the main scientific goals of VLBI observations is the study of AGN, given their high brightness temperature ($T_{\rm B} > 10^6$ K) and their high luminosity ($L_{1.4\rm GHz} > 2 \times 10^{21}$ Wm^{-2} Hz^{-1}; Kellermann et al., 1998; Padovani, 2016; Kellermann et al., 1998) in the core. This can be broken down into areas of VLBI research, such as the study of jets and its associated phenomena around AGN and collapsed stars (Walker, 1999).

VLBI observations can be used for cosmological evolution of galaxies, black holes (BHs) and AGN feedback. For example, radio jets are known to be associated with supermassive accreting black holes, which play a pivotal role in the evolution and formation of galaxies through feedback processes (Britzen et al., 2008) and feedback of AGNs in the early Universe. The evolution of AGN is important for understanding the mechanism of accretion onto SMBHs (Tremaine et al., 2002; Falcke et al., 2004; Croton et al., 2006; Giroletti et al., 2015; Lu et al., 2016) and the corresponding evolution of the host galaxy (Raimundo & Fabian, 2009; Dotti et al., 2012).

VLBI can be used to study the radio evolution of gamma-ray sources at mas resolution, such as structural changes of AGN jets (Pohl et al., 1995).

VLBI observation can also be used to study low redshift absorption lines of compact radio sources of which most are either FR-I or FR-II (Tingay et al., 1996; Readhead et al., 1996; Venturi et al., 1996) in distant galaxies and to study the ISM and circumnuclear gas (Tilanus et al., 2014).

Additionally, VLBI can be used to study transient sources (Lu et al., 2016; Paragi, 2016) such as supernovae, gamma-ray burst (GRB, Mesler et al., 2012; Taylor et al., 1999), fast radio bursts (FRB, Takefuji et al., 2016) and micro-quasars such as X-ray binaries (XRB) to study behaviour and parallaxes (Gwinn et al., 1986; Paragi et al., 2012) especially at higher frequencies (mm-wave and submm-wave).

Furthermore, VLBI can is used for testing cosmology. The compact jets of high-redshift quasars, in particular, can be used for cosmological tests by probing the apparent proper motion and angular size relations as stated by Zhang et al. (2017).

Absolute positions of sources (to ~ 10 μarcsec accuracy) can also be recovered by astrometric methods of VLBI (Bartel et al., 1986; Lanyi et al., 2005; Ros, 2005; Deller, 2009; Dodson & Rioja, 2009).

Science with VLBI also involves the study of positions and movements of objects on earth and in the solar system for the international celestial reference frame (ICRF) (Ojha et al., 2004). Researchers can also study the proper motions, the parallax of pulsars and the interstellar scattering and emission region sizes of pulsars (Paragi et al., 2014).

Gravitational lens systems can be observed (Porcas & Patnaik, 1996; Ros et al., 2000; McKean et al., 2015) with VLBI. This observation was done by Porcas & Patnaik (1996) wherein they made a detailed study of the mas structures of these lens systems using multi-wavelength data. Studying the gravitational lensing can be used to perform an unbiased probe of dark matter substructures using VLBI (Blandford & Narayan, 1992; Deane, 2017). VLBI can also be used to perform studies of SMBHs at high redshifts using gravitational lensing (McKean et al., 2015).

VLBI techniques can be used to test the fundamentals of high energy physics (Kopeikin, 2003). These include testing of gravity (Hees et al., 2016) using pulsar binary systems and testing black hole event horizon (Goddi et al., 2017; Blecher et al., 2017).

Magnetic field orientation can also be estimated in the radio regime with the VLBI if it is observed in the linear and circular polarisation mode (Gabuzda & Gomez, 2001; Pollack et al., 2003).

Several physical quantities in AGN can also be measured directly using VLBI. These include:

- obtaining luminosity directly from flux densities of sources using the relation in Equation 1.4;
- computing redshift-corrected brightness temperature (Condon et al., 1982, 1991; Klöckner et al., 2009) directly using the flux density (S_ν) of sources and the interferometer resolutions (Ros, 2012; Lee et al., 2016) using the expression in Equation 1.8; and
- measuring the difference in position angles of jets in parsec-and kiloparsec-scales.

The next section is a summary of some past VLBI surveys.

1.3.3 Past VLBI Surveys

VLBI observations have been performed since 1967. The first was performed using a 26-meter radio telescope at the Dominion Radio Astrophysical Observatory located at south-west of Okanagan Falls, British Columbia, Canada and another telescope at the Algonquin Radio Observatory located in Ontario, Canada with a maximum baseline of 3074 km (Clark, 1999). Nearly two decades after, the VLBA was constructed to augment the existing VLBI array with much more higher sensitivity and resolution. The EVN, the Long Baseline Array (LBA), the KVN, etc. were added to the arrays above after that. VLBI has been used to observe most of the sources described in Section 1.1.3 in the past. A summary of some of these surveys is given in the paragraphs below.

In the past decades, wide-field post-processing applications to VLBI was a computationally expensive task to perform due to the resulting large datasets. These large VLBI datasets were thus averaged in both time and frequency. This averaging meant that the processed field of view was restricted to only regions of about a few arcsec away from the phase centres of these fields of interest, which does not typically impact the scientific output for short observations, given the VLBI sky source density ($N_{\rm VLBI} \lesssim 1 \sim$ deg.$^{-2}$ for $S_{\rm VLBI} \gg 1$ $\sim$mJy). These challenges were, however, abated by new developments in data analysis, enhanced computing processing and increased data storage capabilities.

Garrett et al. (1999) took advantage of these developments to make wide-field VLBI imaging possible. In their work, Garrett et al. (1999) used the EVN to survey the VLA Faint Images of the Radio Sky at Twenty-cm (FIRST) field at $\lambda = 18$ cm and detected two faint radio sources with an image sensitivity of ~ 0.4 mJy/beam. These pioneered the path toward more wide-field VLBI surveys. Notwithstanding the successes achieved, there were still challenges with the field of view of the VLBI interferometer and problems with the image fidelity when performing data averaging in both time and frequency as stated by Garrett et al. (1999). A follow-up study was then performed on the *Hubble* Deep Field (HDF) using the EVN to study AGN and starburst galaxies at higher redshifts. In their work, Garrett et al. (2001) detected three sources. Their results demonstrated clear potential for future VLBI imaging of sub-mJy beam^{-1} source populations. This paved the way for more wide-field VLBI surveys to be conducted. Other VLBI wide-field studies similar to that of Garrett et al. (1999) and Garrett et al. (2001) were also conducted (Pedlar et al., 1999; Muxlow et al., 1999; Leisawitz et al., 2001; Garrett et al., 2005; Cornwell et al., 2008; Chang et al., 2010).

Although there were significant improvements in the above mentioned wide-field surveys, data sets were still correlated in single phase centre mode with high temporal (2 seconds) and frequency resolution (0.5 MHz) which allowed imaging of significant fraction (10^{-4}) of the entire primary beams (Garrett et al., 2001). However, these methods resulted in massive data volumes. This problem was, however, solved by Deller et al. (2011), by developing a more

flexible, efficient and robust software correlator called the Distributed FX (DiFX) correlator (details in Chapter 2). The DiFX which uses the FX type of correlator architecture runs with a generic multiprocessor computing environment (Deller et al., 2007), and this makes it easy to interface it to modern hard disk-recording systems (e.g., Mark5, Mark5a, Mark5b, Mark5c systems), replacing the old tape-based recording systems. Deller's work made it possible to correlate a large number of phase centres in a single correlation pass and even allows cost-effective upgrading capabilities of the correlators with new and wider recording systems (Deller et al., 2011).

Even though the DiFX was implemented successfully by improving the temporal and spectral resolution which allowed somewhat wider fields of view (Deller et al., 2011), this resulted in increased cost of expanded data volume, as stated by Deller et al. (2011). A solution to this problem is provided by Morgan et al. (2011) who imaged small areas around known sources, by a process called '*uv*-shifting' (see Section 2.2.4). In their work, Morgan et al. (2011) implemented and tested for the efficiency of imaging the large VLBI datasets by using the DiFX software correlator to generate high time and frequency resolution datasets, transformed and then averaged these large datasets multiple times to generate smaller data sets, each with different phase centres. In their work, a four-station VLBI observation of 8.4 GHz in a field containing multiple sources was performed. They used the observations of the calibrator source 3C346 for the preliminary tests of the shifting algorithm and detected one source (1320+299A) which was subsequently used as a phase-reference calibrator to search for more sources in this field. There were, however, no other detections of sources aside from the quasar, 1320+299A (Morgan et al., 2011). These results confirmed the interpretation by Cornwell et al. (2008), who suggested that the source is a head-tail galaxy. The study by Morgan et al. (2011) demonstrated the accuracy of the method and predicted that this method could drastically increase the number of sources which can be studied using the *uv*-shifting method.

Following the success of previous works by Deller et al. (2011) and Morgan et al. (2011), Middelberg et al. (2011) took advantage of this progress to conduct studies on the *Chandra* Deep Field South (CDFS). In their work, Middelberg et al. (2011) conducted a 9-hour VLBA observation of all 96 known (i.e., detected at arcsec scale) radio sources in this field. The survey was carried out at a frequency of 1383 MHz with a baseline sensitivity of 3.3 mJy using 256 Mbps data recording rate. This survey design resulted in a phase centre image rms of about 32 $\mu\mathrm{Jy/beam}$. A new version of the DiFX which included the new multi-field capability was used for the correlation of the data. Naturally weighted images of 8192×8192 pixels were made yielding a resolution of 28.6×9.3 mas^2. Middelberg et al. (2011) were able to detect 20 sources with the VLBA owing to the calibration using wide-field observation technique and extensions made to the DiFX. An additional source was also tentatively detected by Middelberg et al. (2011).

Middelberg et al. (2013) conducted yet another wide-field survey of the Lockman Hole/ XMM. This observation was carried at 1.4 GHz at four (4) different epochs (June 3, July 5 and July 16 and September 3 of 2010) with a data recording bitrate of 512 Mbps yielding a normalised sensitivity of 24 $\mu\mathrm{Jy/beam}$ towards the pointing centre of the antenna. The DiFX software in its multi-field centre mode was used to perform the correlation of the data which resulted in ∼320 datasets per each epoch. Multi-field self-calibration, primary beam correction in addition to standard VLBI calibration was performed. Image sizes of 8.192×8.192 arcsec^2 were made using natural weighting and resolution of 1 mas using the CLEAN algorithm (details in Chapter 3). The images were made centred on pre-selected sources (known position of VLA-detected sources) from arcsec radio maps having flux densities >100 μJy and using ancillary data from other wavelengths. The multi-wavelength data includes GMRT 610 MHz data, providing spectral indices, deep Spitzer/SWIRE data, deep XMM-Newton data and optical coverage with the Large Binocular Telescope and the Subaru telescope. In all, sixty five (65) sources were detected and classified using the sources' morphology, spectral index and ancillary data. It was concluded from this work that the novel multi-field self-calibration scheme greatly improved the coherence of data significantly.

Rampadarath et al. (2015) and Ruiz et al. (2016) also conducted wide-field surveys using multi-phase centre technique. Ruiz et al. (2016) set out to search for RQQs in the Cosmological Evolution Survey (COSMOS) using the VLBA at 1.4 GHz and obtained mas resolution images at 10 μJy/beam in the centre of the COSMOS field. In their work, Ruiz et al. (2016) observed ∼3000 radio sources to statistically study the AGN components of the radio population. They detected 468 radio sources with a signal-to-noise (SNR) higher than 5.5. At a later stage of the project, Ruiz et al. (2016) searched for RQQs on the (Schinnerer et al., 2010) COSMOS field to investigate if they could detect any of these sources with the VLBA. Out of the 18 RQQs found by Schinnerer et al. (2010), Ruiz et al. (2016) were able to detect 3 using the VLBA with a high SNR of 16.4, 8.2 and 7.5 respectively. They concluded that the compact radio flux present in the three detected sources are consistent with the notion that radio emission of RQQ cores provide the dominant contribution to sub-mJy radio source population and that in some RQQs the radio emission come from non-thermal AGN activity as stated by Padovani et al. (2011).

All of the work on imaging larger fractions of field-of-view for other standard VLBI observation contribute to a strong foundation to move to wide-field VLBI surveys in the future. The next section is a summary of some upcoming surveys of VLBI.

1.3.4 VLBI Surveys Of The Future

To perform VLBI surveys in the Southern Hemisphere, the radio community requires a dedicated VLBI array, such as the future AVN (Gaylard et al. 2014; Loots 2015; Copley et al. 2016). The Southern Hemisphere arrays will dramatically improve the long baseline coverage (Figure 1.6) when combined with the EVN for equatorial and northern sources; and will enable surveys of the southern extragalactic fields/targets. Ghana, together with its South African partners, has completed the conversion of a previously decommissioned 32 m telecommunications antenna into a radio telescope to join global VLBI arrays such as the EVN (Wild, 2017). The locations of the stations across Africa, such as Ghana, would significantly improve the image fidelity of VLBI observations as their geographical location will enhance sensitivity to angular scales on the sky that are not typically sampled using current global configurations available (Copley et al., 2016; Wild, 2017). The improved *uv*-coverage with the addition of Ghana's station is shown in Figure 1.6. Another station that will extend VLBI coverage in the Southern Hemisphere when added to the AVN is MeerKAT.

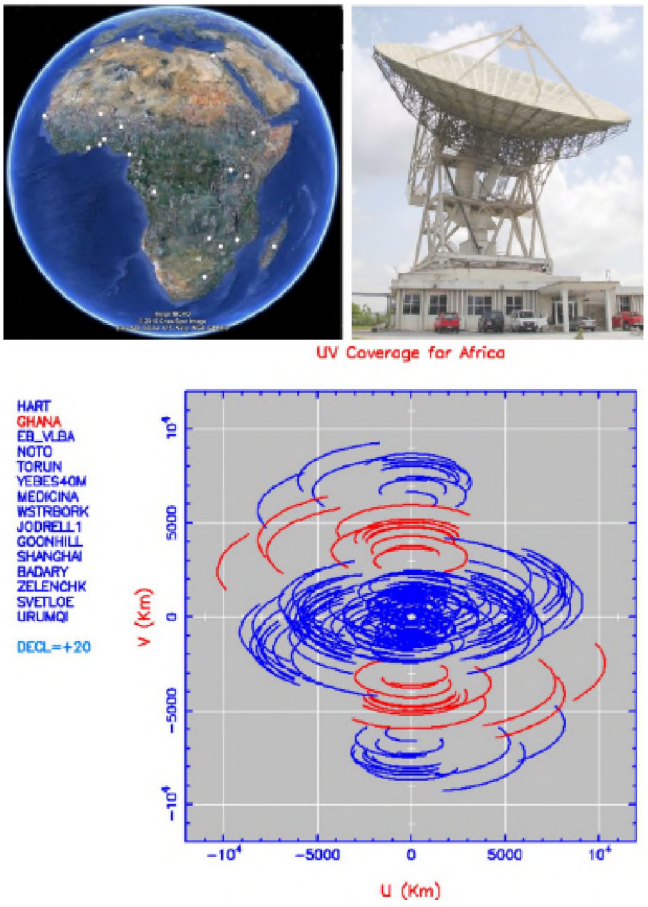

FIGURE 1.6: The diagram on the top left corner shows locations of identified large Satellite Earth Station antennas in Africa which were initially considered for conversion to join the AVN for radio astronomy (Gaylard et al., 2014). The right top corner is Ghana's 32-meter antenna that is in the final stage of conversion to a radio telescope. On the bottom of this image is European VLBI Network *uv*-coverage improvement when two of the AVN telescopes in Ghana and South Africa were added. The blue arcs at the centre of the diagram represent the European-only and Hartebeesthoek Radio Astronomy Observatory (HartRAO) baselines. The *uv*-coverage is further improved (see the red arcs) by the addition of the Ghana station at Nkutunse (Credit: Michael Bietenholz).

MeerKAT is an array of 64 interlinked receptors whose configuration is determined by its scientific goals. It is expected and highly anticipated that MeerKAT will participate in global VLBI surveys in the future. This is poised to add significant sensitivity to existing VLBI networks, especially on the longest baselines (>7000km, Deane, 2017). MeerKAT will add this sensitivity to the EVN and the Australian LBA, and this will strengthen the contribution of HartRAO in regards to gaining higher sensitivity in this part of the *uv*-plane (Deane, 2017). A few of the VLBI surveys that the MeerKAT telescope will be involved in is discussed next.

MeerKAT International GigaHertz Tiered Extragalactic Exploration (MIGHTEE) is a Large Survey Project with MeerKAT to create deep images of the extragalactic sky to explore the cosmic evolution of galaxies at an observing frequency of 1.4 GHz and aims to probe much fainter flux densities (0.1-1 μJy/beam rms, Norris et al., 2013) although it will hit the natural confusion limit of ~ 2 μJy/beam. A component of the MIGHTEE survey is to carry out VLBI

observations which are known as the MIGHTEE-VLBI survey of the relevant extragalactic fields. The following are some of the key scientific contributions of the MIGHTEE-VLBI survey:

- multi-epoch imaging to select astronomical sources based on their mas flux variability as stated by Deane (2017); and
- VLBI polarimetry which will contribute immensely to the MIGHTEE radio continuum and polarimetry surveys by providing detailed information on the sub-kiloparsec magnetic fields and jet physics (Agudo et al., 2015; Deane, 2017).

The involvement of MeerKAT in the MIGHTEE-VLBI observations would, therefore, be enhanced by matched sensitivity VLBI observations across a fraction of the selected field, as stated by Deane (2017).

Potential MIGHTEE-VLBI observations could be commensally carried out with other surveys, such as the Looking at the Distant Universe with the MeerKAT Array (LADUMA; Holwerda et al., 2012; Baker, 2015; Baker et al., 2017). The LADUMA, which is an ultra-deep survey to detect neutral hydrogen gas as a function of redshift and stellar mass will include a deep, albeit confused continuum surveys (Deane, 2017).

VLBI using the SKA has been discussed in previous works by Garrett et al. (1999),200 (2000), Paragi et al. (2014) and Agudo et al. (2015). Their studies outlined the distinctive and remarkable benefits VLBI would add to radio astronomy and the broader astronomical community. With the advent of real-time electronic VLBI operations (e-VLBI, Giroletti et al. 2011), the SKA can be involved in the pursuit of VLBI observations with baselines exceeding 10,000 km as suggested by Norris et al. (2013). In this pursuit, the SKA long baselines and the VLBI, will play a major role in surveys ear-marked to distinguish between AGN (Falcke et al., 2004; Frey et al., 2011, 2012; Dotti et al., 2012; Deane et al., 2014, 2015) and star-forming galaxies (Croton et al., 2006).

The SKA will also be involved in measuring the flux densities and polarisation properties of compact sources and will be used as VLBI calibrator sources, as the availability of calibrator sources has been a challenge to VLBI surveys (Paragi et al., 2014).

This thesis is relevant to these upcoming arrays and surveys, particularly the use of arcsec-scale algorithms which will increase and introduce significant adaptability to standard VLBI post-processing (Deane, 2017).

In the next sections, the research problem, the motivation for the thesis, the objectives of the thesis and the relevance of this work is stated.

1.4 Statement of the Research Problem

The Cosmic Assembly Near-infrared Deep Extragalactic survey (CANDELS) is an HST legacy survey spread across five different fields of the sky to study the distant Universe. One of these five fields is the Great Observatories Origins Deep Survey (GOODS)-North field. Previous VLBI observations of the GOODS-North (details in Section 2.1) field, had highly non-uniform sensitivity across the field and chose to focus on pre-selected sources, either detected with arcsec-scale radio observations or at other wavelengths. It is, however, known that 'radio emission is a relatively unbiased tracer of star formation and can, therefore, probe heavily obscured active galactic nuclei (AGN) – objects that are missed by even the deepest X-ray surveys' as stated by Morrison et al. (2010b). Radio observations of this field will, therefore, allow us to fully exploit the wealth of data taken at X-ray–through–millimeter wavelengths and ultimately expect a significant scientific yield from this uniform sensitivity 'wide' and 'deep' survey. This survey will provide a unique extinction-free probe of galaxy evolution and growth through the detection of starbursts and AGN (Morrison et al., 2010b).

To survey such a wide and deep field like the GOODS-North field requires the use of wide-field imaging which is useful for efficiently conducting large-area VLBI surveys. There are, however, challenges associated with performing wide-field VLBI surveys of the GOODS-North field

- processing challenges to alleviate time and bandwidth smearing (Bridle & Schwab, 1989);
- data processing is generally computationally expensive;
- a lack of the required efficiency in wide-field imaging in standard data reduction packages; and
- current source finding algorithms are not efficient for 64k×64k wide-field images and do not include multi-wavelength information.

The time and bandwidth smearing were mitigated by the survey design using the multiphase centre technique (details in Chapter 2) where each phase centre represents independent visibility data are phase-rotated to user-specified locations and then averaged down (Middelberg et al., 2011; Deller et al., 2007; Middelberg et al., 2013). The time and bandwidth smearing

mitigation was solved by the principal investgator, Dr. Roger P. Deane.

1.5 Thesis Objectives

The thesis objectives are drawn from the challenges of performing wide-field VLBI survey. Hence, a proposed solution to the post-processing challenges of this wide-field VLBI survey are to:

- develop a wide-field VLBI data reduction pipeline including imaging, source finding, cataloguing and multi-wavelength cross-identification. We will incorporate third-generation calibration approaches (Smirnov, 2011); and
- verify the results of the pipeline using the twelve detections from the work of Chi et al. (2013) by comparing the flux values and positions from both surveys.

It is anticipated that solutions proposed will accurately and efficiently enhance the performance of post-processing of wide-field and high sensitivity VLBI radio observations. This is because current VLBI data reduction are still AIPS-based and there is no existing pipeline with a modern software package like CASA.

In this thesis, an attempt is made to demonstrate methods to perform the post-processing of wide-field VLBI data more efficiently and so open discovery space. This is in preparation for more wide-field VLBI programmes with existing and future VLBI arrays en route to the full SKA.

1.6 Scientific Motivation

To conduct VLBI studies of the GOODS-North, the VLBA has been chosen because it is a dedicated VLBI array which provides a continuous operational mode (observations are carried out all year round) unlike EVN or LBA. On a longer term, this makes it possible regarding time domain for structures and evolution of AGNs to be well studied. Secondly, the VLBA has a wider FOV (Field of View) than all the three major VLBI arrays (VERA, EVN and LBA) and its antennas are homogeneous. The homogeneity makes VLBI calibration easier and straightforward.

The GOODS-North field was chosen for this study due to the wealth of multi-wavelength data (Simmons et al., 2011) available, previous VLBI observations, and declination well-suited to the VLBA ($+62^{o}$).

This is the first survey of an extragalactic field with quasi-uniform sensitivity over the entire field. Two of the primary advantages of such a 'uniform field' approach are the potential to detect highly variable AGN and to use stacking techniques.

1.7 Thesis Layout

Chapter One of this thesis gives a background to this work. Chapter Two is a description of the VLBA survey of the GOODS-North field and a literature review of VLBI survey design. In Chapter Three, a description of the calibration and imaging methods used and a host of descriptive details of the algorithms used in this work are given. A description of a newly developed source finder for wide-field VLBI is also mentioned. Chapter Four presents the primary results of this work. Radio images of the known detections and new VLBI candidate sources are also presented. A brief discussion of the candidate sources comparison with multi-wavelength ancillary data is presented. Chapter Five is a summary of the work done and future work to be undertaken. A summary of the detections and what it means for the future of wide-field VLBI is also discussed in Chapter Five.

Chapter 2

The VLBA SURVEY

The supervisor for this work, Roger Deane was the principal investigator (PI) for this survey. Except for the design and planning of the survey and the development of the purpose-built source finder, all the actual work presented in this thesis was done by the author.

Past VLBI surveys were limited by astrophysical challenges such as biases introduced by bright flat-spectrum radio sources (Wrobel et al., 2001) and limited 'field of view' (FOV). The limited FOV issue was addressed using wide-field techniques proposed by Garrett et al. (1999). Using the wide-field technique, Garrett et al. (1999) surveyed the HDF-N and HFF and detected two sources (details in Section 1.3.3). Another wide-field VLBI observation was performed on the HDF-N and HFF by Chi et al. (2013) and they detected 12 sources above 5σ level (details in Appendix A). These two wide-field VLBI observations were however conducted in a conventional VLBI mode and were thus limited by spectral and temporal resolution. Another limitation to these surveys was the primary beam which could only be partially imaged.

Challenges faced by Garrett et al. (1999) and Chi et al. (2013) have been addressed with development of new observational techniques, imaging algorithms, calibration, data correlations techniques (DiFX, Deller et al., 2007, 2010, 2011) as well as improvements in hardware such as antenna sensitivity proposed by Deller et al. (2010). In this work the multi-phase centre approach that makes use of the advanced capabilities of the DiFX correlator was used. The multi-phase method makes it possible to image the entire primary beam of the VLBA. In this way hundreds of previously-unidentified sources can be studied in a single wide-field VLBI observation at mas resolution, without generating extremely large datasets.

Secondly, the key observational difference between this survey and previous wide-field VLBI surveys using multi-phase centre correlation approach such as the *Chandra* Deep Field South survey (Middelberg et al., 2011), the Lockman Hole/XMM survey (Middelberg et al., 2013),

the Cosmic Evolution Survey (COSMOS, N et al., 2017) and GOODS-North survey (Radcliffe et al., 2016) is that the phase centres for this survey were not pre-selected based on any previous radio or X-ray detections. Phase centres for this survey were, however, placed on a regular grid across the field (see Figure 2.1) and the entire survey area is imaged.

This chapter deals with the VLBI survey of the CANDELS GOODS-North field using the VLBA and how it was conducted to achieve a quasi-uniform sensitivity over the entire field. A summary of the CANDELS GOODS-North field is discussed in Section 2.1. Next, in Section 2.2, a discussion of the details of the key technical concepts used in designing this survey is presented. Section 2.3 describes the specific VLBI array used for the survey and the data acquisition technique. A summary of the survey strategies used in order to achieve the quasi-uniform sensitivity across the GOODS-North field is provided in Section 2.4.

2.1 CANDEL's GOODS-North Field

The VLBA survey of the CANDELS (Koekemoer et al., 2011; Grogin et al., 2011) GOODS-North field is a deep and a wide field survey covering $\sim$160 arcmin^2 centred on the *Hubble* Deep Field (HDF;Williams et al. 1996)[1] at 1.6 GHz down to 10 μJy/beam by utilising 205 uniformly spaced phase centres (details in Section 2.2.4). The area covered by the deep CANDELS survey encompasses five well-studied extragalactic fields namely; the All-wavelength Groth Strip International Survey (AEGIS; Davis et al. 2007; Noeske et al. 2007) field, the COSMOS field, the United Kingdom Infrared Telescope (UKIRT[2]) Infrared Deep Sky Surveys (UKIDSS[3]) Ultra Deep Survey (UDS) field and the GOODS Northern and Southern fields.

The GOODS (Giavalisco et al., 2004; Momjian et al., 2010) Survey unites extremely deep observations from NASA's space telescopes (*Spitzer, Hubble, and Chandra, ESA's Herschel and XMM-Newton*), and the most powerful ground-based telescopes, to survey the distant universe to the faintest flux limits across the electromagnetic spectrum (Morrison et al., 2008). This survey presents a high resolution uniform sensitivity VLBI observation of faint sub-mJy radio sources within the CANDELS GOODS-North which is one of the most data-rich survey areas on the sky (Giavalisco et al., 2004). The VLBA GOODS-North field is shown as Figure 2.1.

[1]The *Hubble* Deep Field covers a relatively large area of $\sim$5 arcmin^2.
[2]http://www.ukirt.hawaii.edu/
[3]http://www.ukidss.org/

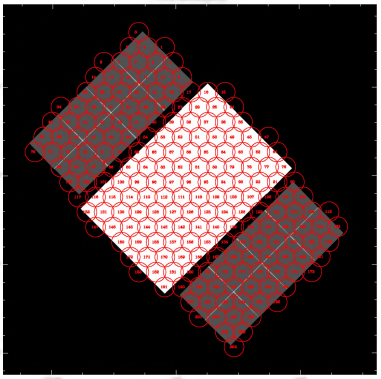

FIGURE 2.1: HST F105W (Dressel, 2012) on-sky chip positions for the CANDELS GOODS-North Deep (white rectangle) and wide (dark grey) fields. The red numeric labels indicate the proposed configuration of the 205 phase centres chosen to optimise uniform sensitivity. The over-plotted red circles indicate the distances of ∼35 arcsec at which 10% cumulative time and bandwidth smearing occurs. (Credit:Dr. Roger Deane, Rhodes University.)

The primary objective of this survey is to compare the host galaxy of VLBI-selected AGNs to those of X-ray-selected sources in order to probe the cause of radio-jet triggering in relation to AGN activity. Several studies have used the resolving power of the *HST* to examine host morphologies of X-ray selected AGN at higher redshifts (z∼1.3). Results from Kocevski et al. (2011) indicate that most major merger traits are likely to be untraceable by an onset of AGN activity, or at least by the time an X-ray emission that indicates AGN activity becomes observable. Numerical simulations by Hopkins et al. (2006) however suggest that initial AGN activity may be Compton-thick which give an indication of what stage the AGN cycle can be observed. Thus, this deep VLBI observation of the GOODS-North field presents a possibility to observe the AGN activity closer to the initial triggering, which will allow observations of host galaxies at a more relevant time. Secondly, understanding the impact of AGNs on their host galaxies will provide answers to key questions in observational cosmology. Mergers which are known to play important roles in triggering AGN activity, are obscured and may be missed by even the deepest X-ray surveys (Kocevski et al., 2011). These obscured quasars remain an elusive population in other multi-wavelength surveys as well, despite their significant cosmological importance. Results from Middelberg et al. (2011) shows that 7% (7 radio cores) of the total number of AGN in the CDFS were not previously detected as AGN at other wavelengths. These 7 objects represented 35% of the total VLBA-selected detected AGN. Thus, their results strongly advocate for a deep, uniform sensitivity VLBI survey to search for obscured systems not traced at other wavelengths.

Additionally, it is only such deep and wide-field VLBI observations which provides the capability to discern between radio emission generated by star-forming processes and AGN activities in distant dust-obscured systems (Middelberg & Bach, 2008). Moreover, VLBI is still the only interferometer technique capable of imaging sub-parsec structures in extragalactic radio sources and to spatially resolve its associated jets on parsec scales (Middelberg

& Bach, 2008).

The details of the multi-wavelength observation of the CANDELS GOODS-North is given in Appendix A.

2.2 Key Technical Concepts in VLBI Survey design

In this section, a summary of the key technical concepts considered in designing our VLBI experiment is given.

2.2.1 Phase Referencing

In order to produce images using aperture synthesis, it is optimal that the amplitude and phases of the visibility at different points in the *uv*-plane is sampled and then Fourier inversion and deconvolution of the data (Beasley & Conway, 1995) is performed thereafter. These visibility phases are corrupted by short-time scale atmospheric variations leading to loss of signal to noise over the course of an observation especially when observing weak sources (Radcliffe et al., 2016). The factors affecting the visibility phases can be classified as phase errors, delays and delay rates. The interferometer phase (Cotton, 1995) is related to the delay by the relation

$$\phi_{t,\nu} = 2\pi\nu\tau_t \ , \tag{2.1}$$

where, $\phi_{t,\nu}$ is the interferometer phase, ν and t are observing frequency and time dependence respectively, while τ_t is the interferometric delay.

After differentiating Equation 2.1, the first order expansion of the error in the interferometer phase can be written as

$$\Delta\phi_{t,\nu} = \phi_0 + \left(\frac{\partial\phi}{\partial\nu}\Delta\nu + \frac{\partial\phi}{\partial t}\Delta t\right) \ , \tag{2.2}$$

where ϕ_0 is the phase error at the reference frequency, $\frac{\partial\phi}{\partial\nu}$ is the delay and $\frac{\partial\phi}{\partial t}$ is the delay rate.

One way of dealing with the effects of phase, delay and delay rate errors is by estimating and removing them from the data using the method of fringe fitting and/or self-calibration (Asaki et al., 2007). However, the absolute positions are lost during self-calibration and self-calibration procedures also require sufficient SNR (SNR$\sim$ 7 per baseline; Beasley &

Conway, 1995) to find/fit accurate solution in delay/delay-rate space. We thus employ phase referencing as an initial approach.

The technique of phase referencing involves applying determined phase corrections from a frequent observation of a nearby calibrator to the target visibility data in order to compensate for any phase variations due to the atmosphere (Asaki et al., 2007).

By correcting for time variable errors, the SNR in long integration improves and, therefore, weak sources can be detected.

The process of phase referencing technique involves :

- observing a sufficiently strong calibrator source near a target in the sky which lies within $\sim 7°$; (Beasley & Conway, 1995) of the target source typically when observing at $\gtrsim 10$ cm wavelength;
- solve for the atmospheric and instrumental complex gains using the calibrator source;
- apply the solutions derived from calibrator to the target source; and
- finally, the target dataset is Fourier transformed to produce a phase-referenced map.

For instance, if the calibrator source is observed at time t_1, the target source is observed at time t_2, and then the calibrator source is observed again at time t_3, then the measured phase from any of these observations can be written mathematically as

$$\phi_{\rm mea} = \phi_{\rm vis} + \phi_{\rm inst} + \phi_{\rm pos} + \phi_{\rm ant} + \phi_{\rm iono} + \phi_{\rm atmo} \ , \tag{2.3}$$

where $\phi_{\rm vis}$ is the phase due to the visibility; $\phi_{\rm inst}$ is the instrumental phase error due to the independent frequency standards, transmitting electronics cables, etc.; $\phi_{\rm iono}$ is the phase error due to dynamic components of the ionosphere; $\phi_{\rm pos}$ is phase error due to uncertainties in the *a priori* source position in the sky; $\phi_{\rm ant}$ is the phase error from thermal noise in the antenna; and $\phi_{\rm atmo}$ is the effect of the atmosphere.

In order to correct the phase of the target source, the measurements on the calibrator at t_1 and t_3 is interpolated to estimate the value of the calibrator phase as if it was measured at t_2. The interpolated phase is then subtracted from the measured phase for the target source. By assuming that the positions of the target and calibrator sources are adequately close on the sky, the visibility phase is zero and calibrator source is marginally resolved (Thompson et al., 2017), then the corrected phase of the target reduces to

$$\phi^{\rm t} - \tilde{\phi}^{\rm c} = \phi^t_{\rm vis} + \left(\phi^t_{\rm pos} - \tilde{\phi}^{\rm c}_{\rm pos}\right) \ , \tag{2.4}$$

where the superscripts c and t represents the calibrator and target sources respectively and the tilde ($\tilde{}$) represents the interpolated values.

There were two calibrator sources observed in this survey, J1234+619 and J0927+390. Two scans of J0927+390 was observed, each for a period of ~ 5 minutes. The calibrator source and the target source experience similar corruptions if the angular distance is kept small ($\lesssim 7^{\circ}$, at $\gtrsim 10$ cm wavelength). Even though J0927+390 was a stronger source it was undesirable to use as a phase calibrator because it is $\sim 42^{\circ}$ away from the VLBA target region, otherwise its phase solutions cannot be transferred accurately to the target source due to differential atmospheric propagation effects. J0927+390 was selected as a fringe-finder. A fringe-finder which is also referred as a delay calibrator, is a strong source (> 1 Jy) which is typically used to fit the excess residual delay and delay rate after applying the correlator model at correlator time.

J1234+619 was used as a phase referencing calibrator as it was only $\sim 0.4^{\circ}$ away from the antenna pointing centre. Target observations were interspersed by ~ 2 minutes long observations of J1234+619 and last ~ 4 minutes, giving a 6 minute switching cycle time (see Figure 2.2). The phase referencing in this work was carried out by alternating the scans of the target field and the calibrator for two (2) hours. This alternate scanning of the target and the calibrator is termed *switching cycle time*[4], $T_{\rm swt}$ (Fomalont & Kopeikin, 2002) and this process reduces the residual temporal phase variations sufficiently. Two main advantages of this method is that it allows imaging of sources fainter than the baseline sensitivity limit specified and it also helps to preserve the absolute sky position information, especially if the position of the calibrator is well known.

Figure 2.2 is a diagrammatic representation of phase referencing showing alternate scans of the target source and the phase calibrator.

[4]The switching cycle time is the observation period from the beginning of the calibrator scan to the target scan and then back to the beginning of the calibrator scan.

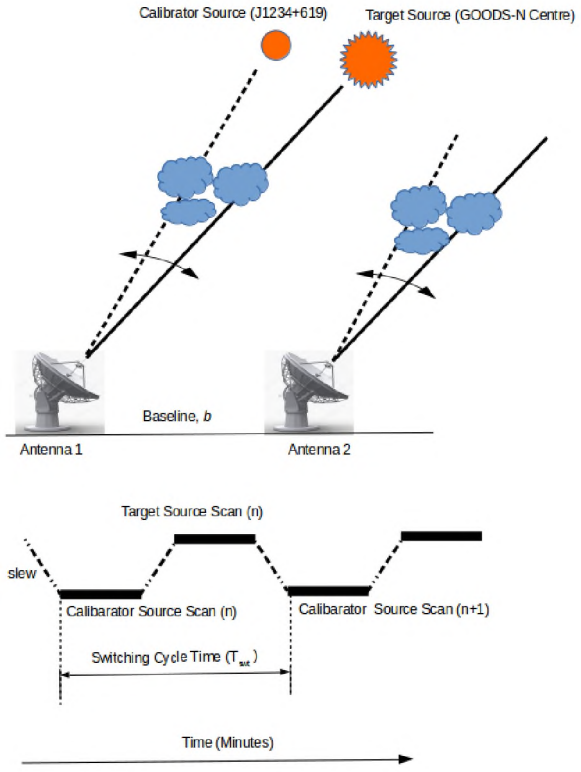

FIGURE 2.2: Schematics of phase referencing showing alternate scans made on the target and phase referencing calibrator. The broken line depicts the slewing of the antenna from the calibrator to the target field and the thick continuous lines represent a scan of either the target source or the phase reference calibrator. The observation period from the beginning of the calibrator scan to the target scan and then back to the beginning of the calibrator scan is referred to as the switching cycle time, $T_{\rm swt}$.

2.2.2 Sensitivity

In radio interferometry and especially for homogeneous interferometers, the image sensitivity is thus determined as the combined sensitivity of all the interferometer combinations of the array integrated over the full time on target. An in-depth knowledge of the sensitivity of the antenna array is therefore key to determining what can be observed in any VLBI survey. The higher the sensitivity of an array, the better it's ability to detect details of fainter sources such as stars, galaxies, etc.

Sensitivity is defined mathematically as

$$\Delta I_{\rm m} = \frac{1}{\eta_{\rm s}} \frac{SEFD}{\sqrt{n(n-1)\Delta\nu\tau_{\rm int}}} \ , \tag{2.5}$$

where $\Delta\nu$ is the bandwidth in Hz; n is the number of antennas involved in the observation; $SEFD$ is the antenna system equivalent flux density; $\tau_{\rm int}$ is the on-source integration time in seconds; and $\eta_{\rm s}$ is the antenna efficiency, which accounts for various losses in the electronics

and digital equipment. The definition of sensitivity (Equation 2.5) is for homogeneous interferometers.

The SEFD is defined as the flux density of a radio source required to produce an antenna temperature equal to the system temperature (Thompson et al., 2017). The system equivalent flux density (SEFD) can be defined mathematically as

$$SEFD = \frac{2\mathrm{kT_{sys}}}{A_{\mathrm{eff}}} \ , \tag{2.6}$$

where k is the Boltzmann's constant, T_{sys} is the system temperature and A_{eff} is the aperture efficiency.

SEFD is a useful and meaningful measure of the sensitivity of a radio telescope (Ellingson, 2011).

To obtain a uniform sensitivity over as wide a field as possibly intended in this work, the phase centres were laid out with partial overlap as can be seen in Figure 2.1.

2.2.3 Time And Bandwidth Smearing

Intrinsically, visibilities in radio interferometry are sampled at some interval in time and frequency. But since we are always limited by increasing data storage capabilities, these visibilities are averaged over time and frequency bins. The averaging of the visibilities typically leads to 'decorrelation'[5] which translates itself in the image domain as smearing especially if the visibilities are not appropriately calibrated. In deep and wide-field observations, smearing becomes a limitation because it smears out emission from a target into the images and this effect reduces the observed amplitudes of off-phase-centre sources (Cotton, 1989; Atemkeng et al., 2016; Thompson et al., 2017).

There are two main types of smearing, namely, time-average and bandwidth smearing. Theoretical estimates of the magnitude of these effects can be found in Thompson et al. (2001). A brief description of these two effects and their solutions will be given in the next two sections.

[5] A 'decorrelated' visibility is a visibility which has been averaged over a too long time/frequency interval which leads point source sensitivity loss especially when visibilities are over-averaged as stated by (Morgan et al., 2011).

2.2.3.1 Bandwidth Smearing

When observations are performed with a finite bandwidth $\Delta\nu$, the visibilities are usually averaged over a finite region of the uv-plane. Smearing of sources occur when there are significant visibility changes in the region over which this averaging is done. An example of the schematics of the effect of this is presented as Figure 2.3.

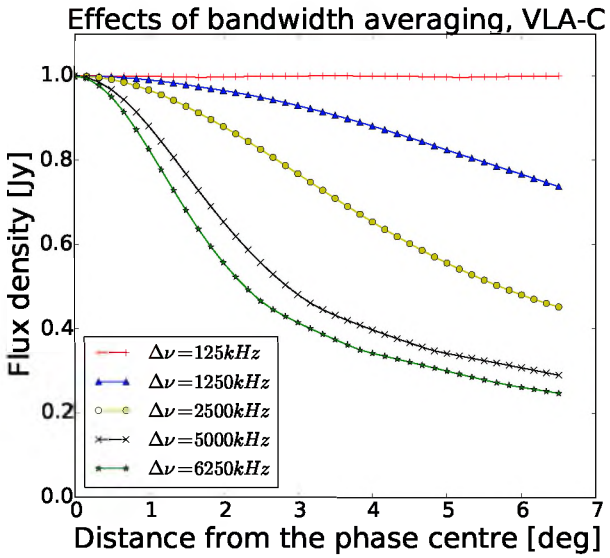

FIGURE 2.3: Effects of bandwidth averaging as seen by the VLA-C at 1.4GHz; showing the apparent intensity of a 1 Jy point source, as a function of distance from the phase centre with a time interval fixed at 1 s and with varying frequency intervals **(Credit: Atemkeng et al., 2016)**.

As can be seen from Figure 2.3, finite channel width causes loss of coherence at large angles, because the amplitude of the interferometer fringes are decreased with increasing angular distance from the phase centre. There are, however, computational methods which allow us to predict the level of sensitivity loss, but it cannot be recovered. The practical solution is to observe with a small channel width, however this will increase the data volume. The effect of bandwidth smearing can be parametrised by the relation

$$\frac{\Delta\nu}{\nu}\frac{\theta}{\theta_{res}} \ll 1 \ , \tag{2.7}$$

where $\Delta\nu/\nu$ is the fractional bandwidth and θ/θ_{res} is the source offset in units of the fringe separation, λ/B.

The best solution is to observe with lots of narrow channels which can be achieved with modern correlators like the DiFX (details given in Section 2.2.4).

2.2.3.2 Time-Average Smearing

Time or time-averaging smearing is defined as the degradation of the reconstructed image of any observed celestial body by an interferometer that occurs as a result of large integration time. The effects of time-average smearing is shown in Figure 2.4.

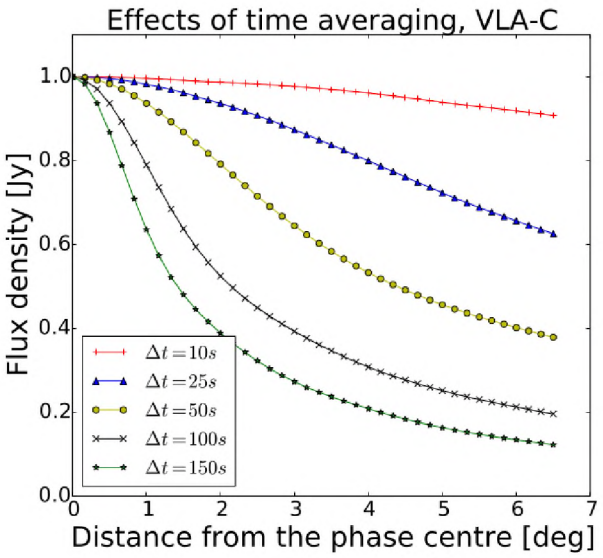

FIGURE 2.4: Effects of time averaging as seen by the VLA-C at 1.4GHz; showing the apparent intensity of a 1 Jy point source as a function of distance from the phase centre at 125 kHz with a varying time intervals **(Credit: Atemkeng et al., 2016)**.

For example, to achieve a desirable processed[6] FoV of 2° across with the VLA in C configuration at 1.4 GHz (Figure 2.4), we can only use an integration time of $\Delta t < 10$ seconds, else we achieve an undesirable smearing of >10%. One solution is to reduce the integration time but this results in large datasets, more I/O[7] time and more processing. The condition for minimal time loss is given as

$$t \ll \frac{\lambda}{\omega_{\mathrm{e}} B \theta} = \frac{D}{\omega_{\mathrm{e}} B} \, , \tag{2.8}$$

where ω_{e} is the fringe rotation rate about the centre and B the given baseline.

A proven strategy used in observations to curb time averaging and bandwidth smearing of the 160 arcmin^2 field can be shown in Figure 2.5.

[6]The processed FoV is also known as the Field of Interest (FoI), which is defined as the fractional region/portion of the primary beam of interest.

[7]Input/Ouput

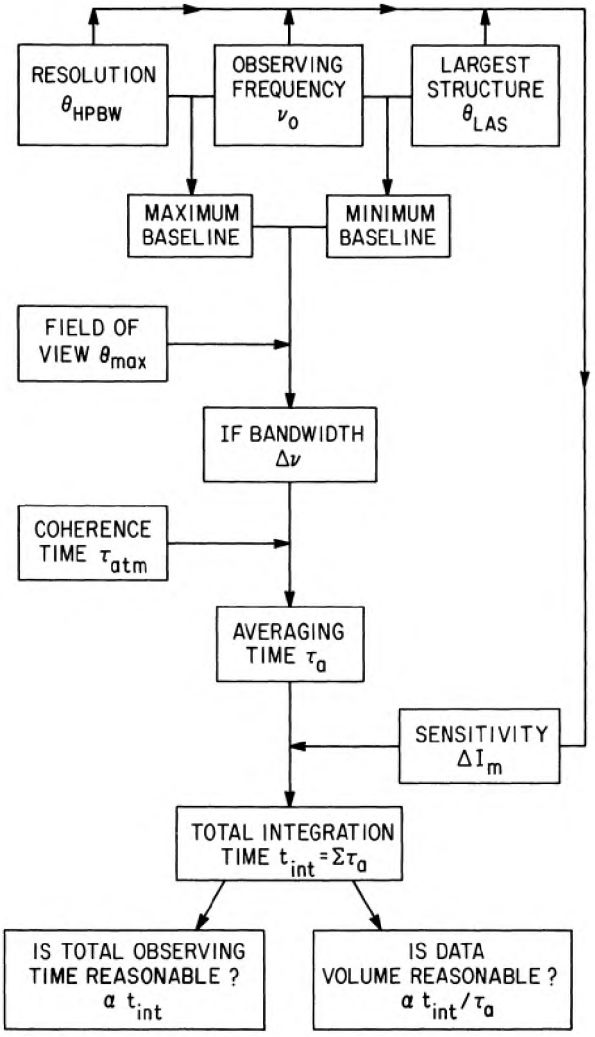

FIGURE 2.5: Schematics of factors considered for continuum observing strategy- a suggested decision tree **(Credit: Bridle, 1989)**.

The effect of smearing is exacerbated in VLBI because it limits the usable FOV which is smaller than the primary beam as in the case of the VLBA or homogeneous interferometers or of the largest telescope in the array in the case of heterogeneous interferometers. For example, imaging an entire primary beam of about 30 arcmin with a 25 m dish at 1600 MHz at VLBI resolution is computationally impractical to achieve because it requires 10s or 100s of TB of visibilities to be produced but majority of the images would be empty (Deller et al., 2011). But that is not desirable, hence, for practical reasons, the typical VLBI correlator will produce visibilities with time resolution of a few seconds and a frequency resolution of ∼100s of kHz. Thus, the visibilities produced are much smaller- a few Gigabytes.

In this work, we resorted to using multi-phase centre technique during correlation which drastically reduces the large datasets to sizable visibilities which can then be imaged using less computational processing. This was achieved using the DiFX correlator (Deller et al., 2011).

2.2.4 DiFX Correlator

In radio astronomy a correlator is basically a digital device that combines Nyquist-sampled two-station baseline pair voltage time series and computes the cross-correlation function (footnote 7 in Section 1.3) as a function of time lag to produce sets of complex visibilities, V_{ij}. An example of a correlator is shown in Figure 2.6.

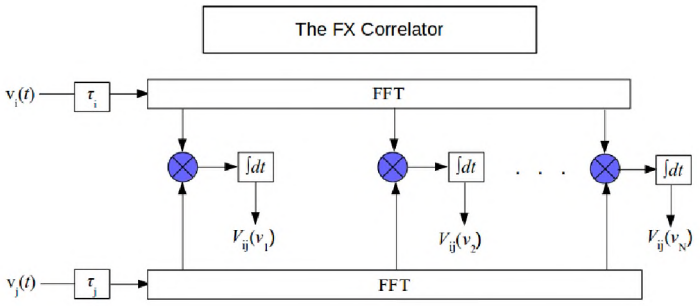

FIGURE 2.6: Schematics of a simple FX correlator: Signals from the pair of antennas are first Fourier transformed, cross-multiplied (blue symbol) and thereafter integrated.

The Correlator used in this survey is the DiFX correlator as already mentioned in Chapter 1. DiFX is a Distributed FX software correlator written by Deller et al. (2007) in C++. It uses the FX fundamental operation in correlation as shown in Figure 2.6. Detailed descriptions of the FX are found in (Thompson et al., 2001; Romney, 1999).

The procedure implemented by the DiFX correlator is given as Figure 2.7.

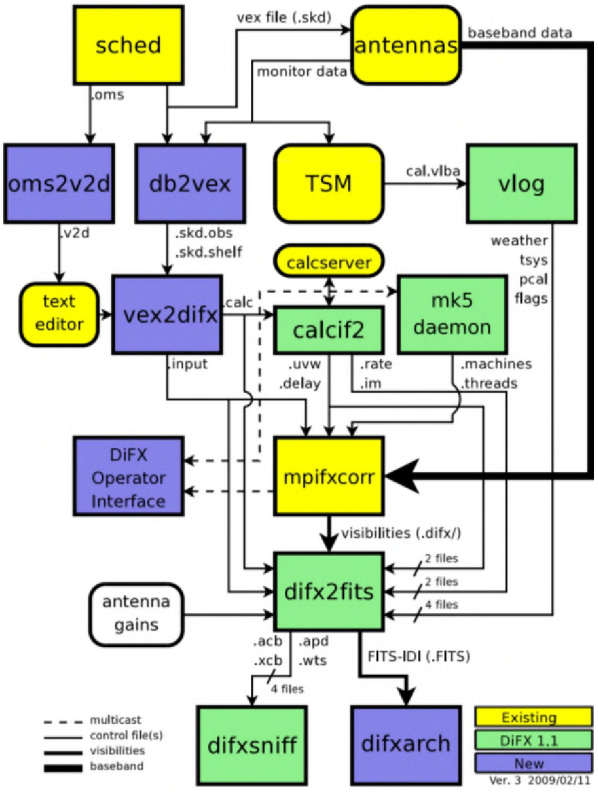

FIGURE 2.7: DiFX procedure for Correlation of Observed data. **vex2difx** takes *.v2d* file as input and produces *.input* and *.calc files*, then **calcif2** takes *.calc* file as input and produces model files (*.uvw, .delay* etc.), **mpifxcorr** writes output files to *.difx* directory and finally **difx2fits** converts the output to FITS **(credit: Whitney 2006).**

In this work, to convert hundreds of TB of baseband data into ∼4 TB of visibilities, the dataset is read into memory first and once from disks. Then **vex2difx** (Deller et al., 2010; Brisken, 2010; Deller et al., 2011) is used to specify the number of phase centres to be correlated. The correlation is initially carried out with high frequency resolution which is also sufficient to minimise bandwidth smearing and high time resolution periodically to minimise sensitivity loss due to smearing across a larger field of view. A model of each of the phase centres is then computed and passed to the correlator and then a *uv*-shifting is subsequently performed. A *uv*-shifting (Morgan et al., 2011) requires a rotation of the visibility phases of each baseline by an amount which is equal to the difference in geometric delay between the final and initial source directions, multiplied by the sky frequency (Middelberg et al., 2011). The phase rotation is performed repeatedly for each desired source direction. After the phase shifting is applied, the visibilities are then averaged in frequency and time. The DiFX correlator in its multi-phase mode then produces independent FITS (Hanisch et al., 2001) or FITS-IDI (Greisen, 2009) files containing different phase centres. In a single pass 205 independent phase centres were generated for each epoch, each of which were written out as independent data files, just as if the correlator has been run 205 times. Consequently, this results in an array of 'normal-sized' visibility datasets, for each of which there is a 10% loss at a radius of 35 arcsec.

The first FITS-IDI file of each schedule block (SB) contains the first phase centre (PC000) together with the gain calibrator and the fringe-finder. The subsequent FITS-IDI files of each epoch however, contain only the respectively listed phase centres (PC001 to PC204). In addition to the visibility function measurements and its associated meta-data, the FITS-IDI files include amplitude and phase calibration measurements, weather data (WX), and editing flags that are logged at the VLBA station (Ulvestad, 1999).

A diagrammatic comparison between traditional VLBI and multiphase centre approach is shown as Figure 2.8. Here we illustrate that multiple phase technique leads to a dramatic decrease in the amount of data stored when compared to a single pointing of the same field at very fine time and frequency resolutions. The values in the caption of Figure 2.8 were calculated using the online EVN wide-field calculator[8].

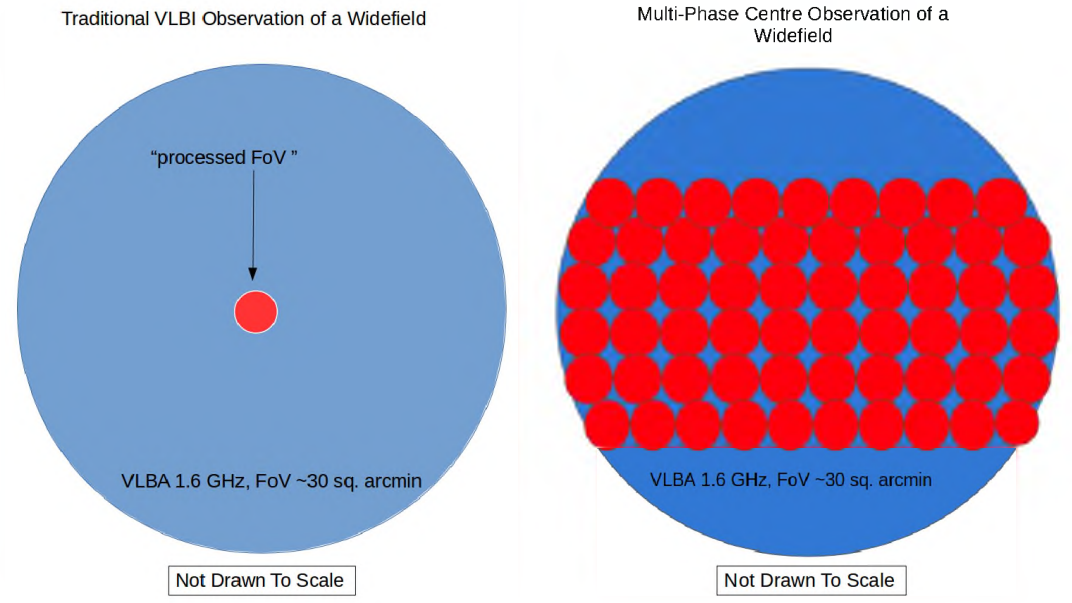

(A) (B)

FIGURE 2.8: Illustration of the differences between traditional VLBI and Multi-phase centre approach. The FoV of the VLBA with an 8-hour observation time (48 mins on-source integration time) at a frequency of 1.6 GHz, maximum baseline of 9000 km, 2 seconds integration time (equivalent of using 108 channels to obtain the same FoV limited by bandwidth-smearing), 2048 Mbits/s aggregate bit rate and a 2 bit sampling rate will produce ∼10.93 GB of output data after correlation. (a) To conduct a survey using the traditional VLBI observation of a total field of 160 arcmin^2 for this same 8-hour run will produce >500 TB of data. (b) Using a multi-phase centre approach on the other hand to process about 533 phase centres to cover the entire 160 arcmin^2, for an 8-hour run will yield a correlated data size of $\sim$ 533 X 10 GB = $\sim$ 5.33 TB. Note that all the parameters for both scenarios are the same except for the integration time and the values for the data outputs are calculated for 10% loss in the response of the point source sensitivity using the EVN calculated.

FoV of 30 sq. arcmin specified in Figure 2.8 represents the FoV of every 25 m antenna.

[8]http://www.evlbi.org/cgi-bin/EVNcalc

2.3 VLBA

The Very Long Baseline Array (Frey, 2006) is an array of 10 dishes, each with a diameter of 25 meters, distributed across North America from Mauna Kea (MK) in Hawaii to St. Croix in the Virgin Islands. Its maximum baseline is ∼8600 km and it operates between 0.3 and ∼87 GHz achieving an angular resolution between 25 and ∼0.08μ arcsec respectively. To put this in a more practical perspective, for an 8-hr duration observation at 18 cm, the VLBA is easily able to detect signals from sources with sensitivity of $\sim 10\ \mu$Jybeam^{-1} which corresponds to brightness temperatures above $T_{\rm b} > 10^5$K (Dodson & Rioja, 2009; Romney et al., 2010; Deller & Middelberg, 2014). The VLBA has a 3.5 m diameter Cassegarian sub-reflector. Moreover, the VLBA is a *dedicated* VLBI instrument which offers sufficient observing time in a continuous operational mode (Walker, 1995). The VLBA observations are scheduled using the program SCHED[9] [10] (Walker, 2015). It uses the DiFX correlator for its correlation. The VLBA uses a Polyphase Filter Bank (PFB) back-end which provides sixteen 32 MHz channels with a fixed recording rate of 2048 Mbps. These channels can be selected between two VLBA Intermediate Frequency (IF) inputs and the area restricted to 32 MHz steps. The observational parameters used in this survey are given in Table 2.1.

TABLE 2.1: Observational configuration.

Observing Parameter	Details
Observation Date	13 Oct 2013 to 02 Nov 2013
Frequency	1.6 GHz
Bandwidth	32 MHz
Channels per spectral window	128
Spectral Window	8
Pointing Centre	RA, DEC= 12h36m55.0s, +62d14m15.0s
Polarisation	Dual
Sensitivity	10 μJy/beam
Back-end system	PFB system
Aggregate bit rate	2048 Mbits/sec

Next, a summary on the survey strategy used by the VLBA on the CANDELS GOODS-North field is presented.

[9]The SCHED program is a program for planning and scheduling the VLBA and most VLBI observations.
[10]The SCHED program is used, among other tasks, to determine Green Sidereal Time (GST) range during which time the VLBI target sources are visible at the participating stations and it can also be used to evaluate the *uv*-plane coverage and synthesised beam.

2.4 Observational Strategy

The observation for this work was carried out at 12 epochs, from September 13, 2013 to November 2, 2013 using a standard VLBA continuum observing setup with a frequency at 1392 MHz to 1744 Mhz centred on RA=12:36:55.0 and Dec=+62:14:15.0. A total of 24 hours observing time was split into twelve 2-hour runs. The observational strategy was to observe the same field at the 12 different epochs in order to obtain a better *uv*-coverage. Eight spectral windows, bandwidth of 32 MHz and 128 MHz channels were used in this observation, both with the right and left circular polarisation and aggregate bit rate of 2048 Mbps, assuming 2 bit sampling. An integration time of ∼2.05 seconds was used in order to reduce time smearing. The distance between each phase centre (∼35 arcsec) was also calculated in order to limit the cumulative band and time-smearing losses to 10%. The angular offset (∼35 arcsec) was chosen as a recompense between the data volume of the raw VLBI visibility datasets, subsequent image processing requirement, correlator capacity and the sensitivity loss within a given phase centre. Secondly, the maximum image size was a key consideration. A first calibrator source, J0927+390 [11] (Krips et al., 2007) with a flux density of $S_{1.7}$ ∼2.37 Jy/beam (Fey et al., 2015) was used as fringe-finder. The calibrator source, J1234+619 which is a well-known source from the novel VLBI observation of HDF-North with a flux density of $S_{1.4}$ ∼20 mJy/beam (Chi, Garrett & Barthel, Chi et al.; Chi et al., 2013) was used as the phase gain calibrator as well as a nodding on 10-minute duty cycles.

All observations were performed in continuum mode. On the average 9 out of 10 antennas were operational in all 12 observations (epochs), while in 2 of the observations all 10 antennas were in full operation. The observation of the HDF-North field was performed in a phase referencing mode as described in Section 2.2.1 while the data was correlated at the Pete V. Domenici Science Operations Center (SOC) in Socorro, New Mexico. The correlation of the data was performed in the multi-phase centre mode using the DiFX correlator at SOC as described in Section 2.2.4.

The survey of the CANDELS GOODS-North produced a total of 2460 individual datasets for the total duration of 24 hours for the entire 12 epochs/SBs. The raw data set size for each phase centre is ∼1.5 GB, yielding about ∼ 390 GB per epoch. The total amount of raw data from our observation is ∼4 TB, for all 12 epochs, indicating significant amount of computing effort in the data processing stage. In VLBI, because of the high brightness requirement, most of the primary beam field will principally be empty but may significantly contain a number of compact sources (Thompson et al., 2017). One unique attribute of this survey is the use of the multi-phase centre technique to achieve quasi-uniform sensitivity

[11] Flux density for J0927+390 at 2.771 Ghz was given as 2.37 Jy/beam (Fey et al., 2015) and found to be $S_{1.6}$ ∼2 Jy/beam in this work respectively.

across the entire field as already stated. The calibration and imaging of the datasets is discussed in the next chapter.

Chapter 3

VLBI CALIBRATION PIPELINE

The data calibration pipeline aside, the development of the purpose-built source finder was developed by the student.

It is factual that few data reduction pipelines for VLBI have already been developed and some are still being developed. However, none of these pipelines are able to meet all the calibration demands.

For example, the VLBI data processing pipeline developed by Reynolds et al. (2002) to automate data reduction for VLBI experiments at the Joint Institute for VLBI ERIC[1] (JIVE) for EVN[2] run entirely within AIPS (using AIPS tasks and facilities) but it is not completely automated, although it greatly speeds up the calibration process. Secondly, the VLBI data reduction pipeline developed by Sjouwerman et al. (2005) for VLBA projects runs only in AIPS and does not include automatic flagging of observing conditions such as high levels of radio-frequency interference. The pipeline does not process data from correlators aside VLBA and does not perform interactive flagging. Moreover, other pipelines such as those developed by Hodgson et al. (2016) are only able to handle single polarisation KVN data, while that developed by Zhang (2016) does not incorporate multi-wavelength data. All the above-mentioned pipelines fall short of meeting all the data calibration demands for future wide-field VLBI surveys.

In this chapter, we present the wide-field VLBI data reduction pipeline that we developed for calibration, imaging, source finding and analysis for the VLBA GOODS-North data. The wide-field VLBA pipeline is loosely based on an existing pipeline developed by Sjouwerman et al. (2005) but also implements several additional features compared with a standard AIPS-based pipelines such as the EVN pipeline. Additionally, the wide-field VLBA pipeline uses more efficient and current algorithms for calibration, imaging, source finding, and incorporates multi-wavelength data.

[1] European Research Infrastructure Consortium
[2] European VLBI Network (http://www.evlbi.org/)

The data processing strategy developed for this work is shown in Figure 3.1.

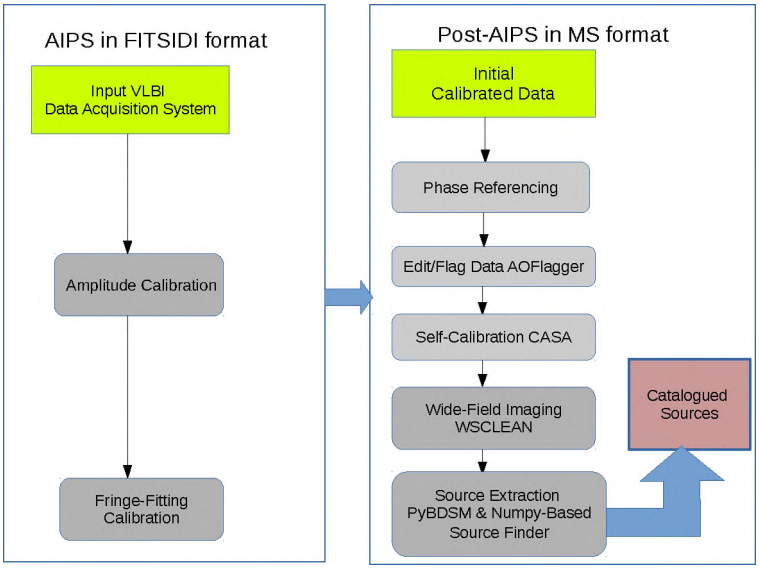

FIGURE 3.1: Flowchart of data processing strategy: All initial processing of data including fringe-fitting is performed in AIPS (data in FITS-IDI format) whiles post fringe-fitting is performed using newly developed algorithms (data in the MS format).

3.1 General Calibration

In radio astronomy, calibration is defined as the process of solving and removing instrumental and atmospheric effects embedded in the signal during its propagation toward and within the interferometer. The instrumental propagation effects consist of transmission errors accumulated in the signal processing system, while the atmospheric effects include ionospheric and tropospheric errors, along with effects, such as antenna pointing errors.

In the absence of any propagation effects, the visibilities measured by a radio interferometer are given by Equation 1.25. However, in practice, because of propagation effects, the measured visibilities must take propagation effects into account. This can be done in the framework of the RIME[3] (Smirnov, 2011; Hamaker et al., 1996) formulation as

$$\mathbf{V}_{pq}^{\text{obs}} = \mathbf{J}_p \left(\iint_{lm} \mathbf{B} e^{-2\pi(u_{pq}l + v_{pq}m)} dl\, dm \right) \mathbf{J}_q^H \ , \tag{3.1}$$

where $\mathbf{V}_{pq}^{\text{obs}}$ is the observed visibility, $\mathbf{B}$ is a 2×2 brightness matrix which describes the brightness distribution as a function of the direction l, m, $\mathbf{J}_p$ and $\mathbf{J}_q$ are the Jones matrices associated with antennas p and q which encode the propagation effects that affect the signal on its path to antennas p and q respectively.

[3]RIME is the radio interferometer measurement equation.

Equivalently, the RIME can be written as

$$\mathbf{V}_{pq}^{\text{obs}} = \mathbf{J}_p \mathbf{V}_{pq}^{\text{True}} \mathbf{J}_q^H \ , \tag{3.2}$$

where $\mathbf{V}_{pq}^{\text{True}} = \mathbf{V}(u_{pq}, v_{pq})$ is the 'true' visibility as e.g. given by Equation 1.25.

We can break $\mathbf{J}_p$ into a chain of propagation effects:

$$\mathbf{V}_{pq}^{\text{obs}} = \mathbf{G}_p \mathbf{E}_p \mathbf{P}_p \mathbf{T}_p \mathbf{Z}_p \mathbf{V}_{pq}^{\text{True}} \mathbf{Z}_q^H \mathbf{T}_q^H \mathbf{P}_q^H \mathbf{E}_q^H \mathbf{G}_q^H + \mathbf{RFI} \ , \tag{3.3}$$

where, $\mathbf{G}_p$ is a diagonal matrix representing electronic gains, $\mathbf{E}_p$ are the effects introduced by the optical components of the telescopes, such as the collecting area's elevation dependence, $\mathbf{P}_p$ is parallactic angle rotation, $\mathbf{T}_p$ are the tropospheric phase delays, $\mathbf{Z}_p$ are the ionospheric phase delays caused by excess pathlength as a result of refraction and **RFI** represents addictive noise from radio frequency interference (RFI). The order of the RIME represents the causal order of effects.

The Jones terms are determined via a non-linear fit of the measured visibilities to the model visibilities. The corrected visibilities can then be obtained by applying the inverse of the estimated Jones matrices to the measured or observed visibilities as:

$$\mathbf{V}_{pq}^{\text{True}} = (\mathbf{J}_p)^{-1} (\mathbf{V}_{pq}^{\text{obs}}) (\mathbf{J}_q^H)^{-1} \ , \tag{3.4}$$

where $()^{-1}$ denotes a matrix inverse.

The rest of this chapter is dedicated to the post-processing pipeline developed for this work.

3.2 VLBI Calibration Pipeline

In this section we describe the initial calibration performed using the Astronomical Image Processing System (AIPS) software to correct for phase errors and perform fringe-fitting along with data flagging. Further calibration was done using the Common Astronomy Software Applications (CASA). Imaging was done with both CASA and WSCLEAN. Lastly, we describe the source finding algorithm implemented.

3.2.1 Data Calibration In AIPS

The first stage of calibration was carried out using the Astronomical Image Processing System (AIPS; Wells 1985; Palmer 1996; Fomalont 1981; Greisen 1990). AIPS is a data

reduction software developed by NRAO[4] for interactive data calibration, editing and imaging of interferometric data using Fourier synthesis. It is the primary data package for VLBA observations performed in both continuum and spectral line modes (Greisen, 1990).

Figure 3.2 is a flowchart describing the calibration procedure.

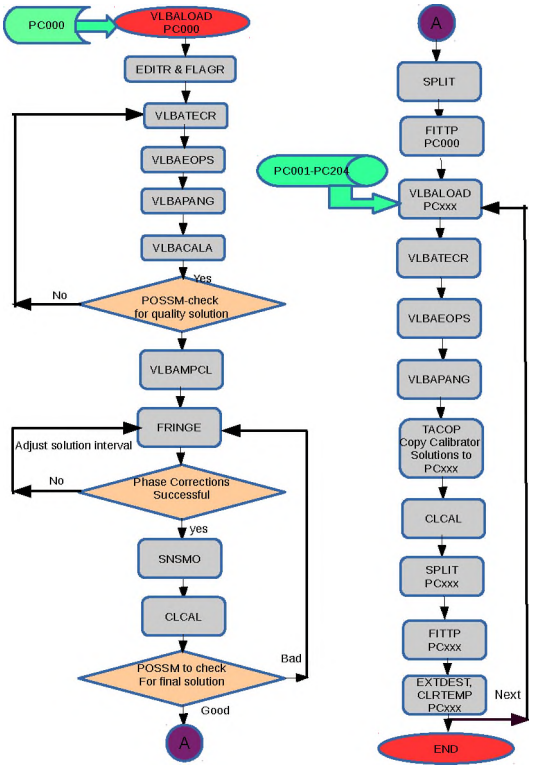

FIGURE 3.2: Flowchart of the initial calibration in AIPS. The phase centre PC000 contain the calibrator sources while the phase centres PC001-PC204 are just phase centres within the FoV centred on GOODS-North.

We developed the initial pipeline in AIPS which is composed of python programs based on the AIPS interface, POPS (Kettenis et al., 2006), to perform the calibration up to fringe-fitting when the data is exported to a UVFITS format. POPS is an inbuilt AIPS language that permits basic routines to be performed instead of laborious manual repetitions.

To use the already existing procedure in AIPS for the wide-field VLBA pipeline, we first activate the AIPS task VLBAUTIL (Sjouwerman et al., 2005). The VLBAUTIL task uses a procedure called VLBARUN which uses the VLBA calibration procedures to calibrate VLBA data[5]. The data are then loaded into AIPS with the task VLBALOAD by specifying the path to the directory of the stored raw data. The VLBALOAD task calls FITLD, TACOP, TAMRG and INDXR tasks. The FITLD task uploads the corrected output

[4]http://www.nrao.edu/

[5]The out data from the correlator for this work are in Flexible Image Transport System Interferometry Data Interchange (FITS-IDI;Greisen 2009) format.

FITS-IDI data into AIPS. Then the task TACOP is used to copy the gain curve (GC), pulse-cal (PC), weather (WX) and system temperature (TY) tables which are read in by the AIPS ANTAB and sent to the line data file. The task TAMRG merges the GC, PC and TY[6] tables and removes redundant calibration (CL[7]) table entries and sorts the data by time and baseline. The task INDXR is then used to make an index (NX)[8] table and a calibration file (CL) where no calibration has been applied.

It is essential to inspect the details of the data before beginning the actual calibration; this is done using the task LISTR which gives information for each observed band about the names of the sources, coordinates and integration time. The first step of manual flagging is then performed on the fringe finder source, which was observed for a short scan. This was achieved by inspecting the dataset using the AIPS task EDITR and FLAGR interactively to remove any outliers.

After inspecting the data, the *uv*-coverage is plotted to have a further look of the visibilities, and especially the calibrator sources. The *uv* coverage for the gain calibrator, J1234+619 is shown in Figure 3.3.

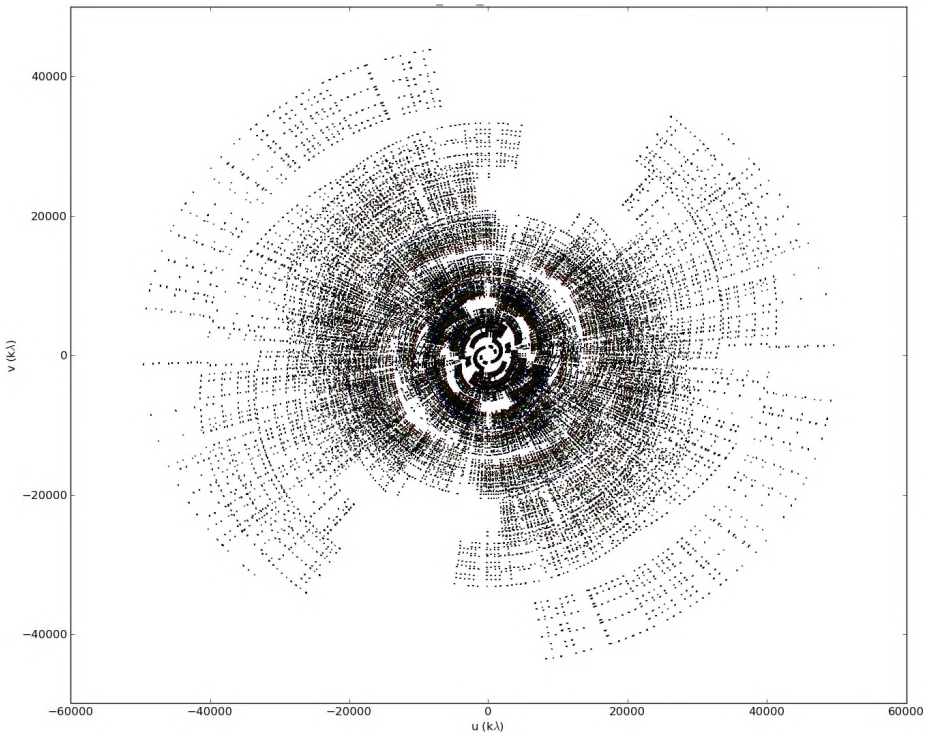

FIGURE 3.3: UV coverage of the gain calibrator of the 12 epochs concatenated together in order to attain a better *uv*-coverage for imaging.

[6]TY is the system temperature tables. The system temperature is used to determine the sensitivity and the SEFD which are used for amplitude correction.

[7]CL: calibration table containing all the current calibration information that is intended to be applied to the data.

[8]NX is an index table which contains various information about each scan and a summary of the data.

After the initial inspection of the data, the actual calibration process then follows. The next sections deals with the main AIPS calibration.

3.2.1.1 Ionospheric Corrections

The atmosphere typically contains water vapour which is poorly mixed with trace gases (O_2, N_2). Given that there is a different troposphere (water vapour at an altitude of about 6–10 km) over each VLBI antenna, tropospheric delays and turbulence are typically a problem at higher frequencies (> 8 GHz). However, ionospheric (free electrons at 100-1000 km altitude) delays dominate at low frequencies (2 GHz and lower) and this can cause large unmodelled dispersive delays, which is seen as rapid phase wrapping. This is of particular importance in phase referencing observations, which is implemented in this work, where phases must be interpolated over weak sources (Thompson et al., 2001).

An electromagnetic wave with frequency ν passing through the ionosphere undergoes a phase shift given by

$$\Delta\phi = -8.45 \left(\frac{\mathrm{TEC}}{1\ \mathrm{TECU}}\right)\left(\frac{\nu}{1\ \mathrm{GHz}}\right)^{-1} \mathrm{rad}\ , \tag{3.5}$$

where TEC is the integrated electron density in TEC units (1 TECU $=10^{16}$ electrons m^{-2}).

The Total Electron Content (TEC) is defined as the total number of electrons present along a path between a radio telescope and a source.

An interferometer measures phase differences and so the signal measured is distorted if the ionospheric electron content above its antennas differs (Mevius et al., 2016).

One method of removing the mean ionospheric phase error is by applying a global ionospheric model derived from Global Position System (GPS) measurements taken simultaneously with the radio observation. In AIPS the ionospheric phase correction is achieved using the task VLBATECR. VLBATECR uses a global model of the total electronic content to correct ionospheric dispersive delays by automatically downloading the needed IONEX (IONosphere map EXchange) files from the Crystal Dynamics Data Information System (CDDIS[9]) archive by using the task TECOR. TECOR corrects and calculates dispersive delays and then creates a calibration table (CL).

An example of the phase corrections derived from the TEC information contained in the IONEX file is shown in Figure 3.4.

[9] http://cddis.nasa.gov/

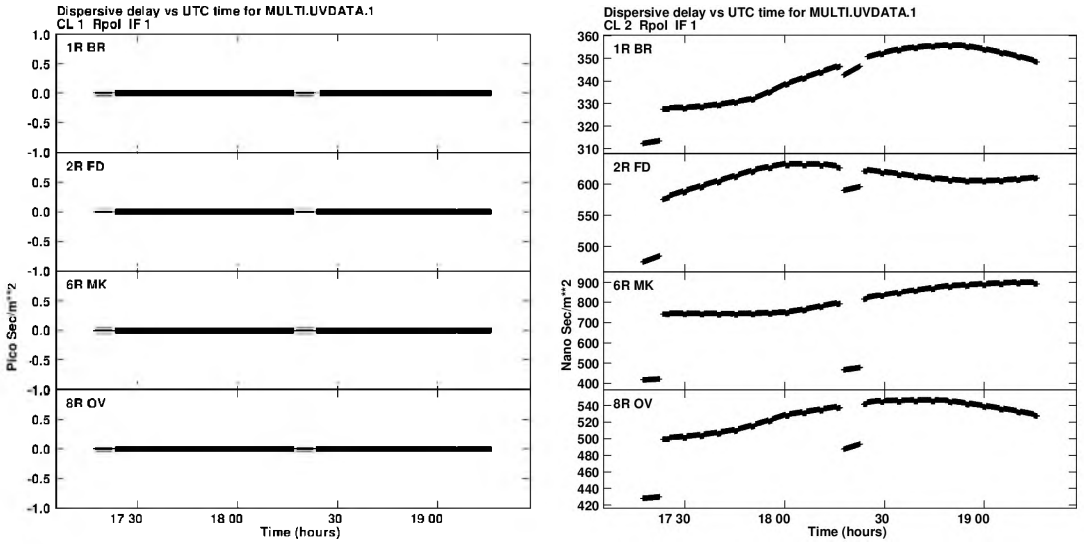

(A) First calibration table (B) Ionospheric delay corrections

FIGURE 3.4: Ionospheric delay corrections (CL2) applied to the first calibration table (CL1) of phase centre PC000, for the VLBA antennas Brewster (BR) , Fort Davis (FD), Owens Valley (OV) and Mauna Kea (MK). The plot only show the corrections applied to one spectral window and an RR polarisation, however, in reality we applied the corrections to all the antennas, spectral windows and the two polarisations.

3.2.1.2 Corrections To The Earth Orientation Parameters

The rotation of the Earth is not even and so any motion can cause a retardation or acceleration of the rotation, or a change in the Earth's axis. Such movements sometimes result in noticeable changes which cause errors in radio astronomy observations.

An accurate determination of the Earth's rotation is therefore important to mitigate incorrect source positions and to prevent smearing of the target sources in phase referencing experiments like the one applied in this work. The Earth Orientation Parameters (EOP) describe irregularities of the Earth's rotation. These parameters include polar coordinates, universal time and nutation. Details of the description of these parameters can be found in (Thaller et al., 2007).

The EOPs change slowly with time and therefore the EOPs used by the correlator must be continually updated. To correct for the effect of the EOP we used the AIPS task VLBAEOPS. The VLBAEOPS task automatically downloads EOP file and runs the task CLCOR which applies the corrections to the EOP using the CT (CALC table) . This ensures that the position of the target source is maintained and there is no smearing of the target source. CT calculates the difference between the old EOPs and the new EOPs and then applies it to the data.

3.2.1.3 Parallactic Angle Corrections

When using antennas with multiple feed systems, there is a need for a correction angle which is required to maintain a constant orientation with respect to the equatorial coordinate system. This correction angle is referred as the parallactic angle. Parallactic angle thus describes the rotation of the feeds of an ALT-AZ [10] telescope (such as the VLBA), with respect to the celestial sphere as the telescope tracks an astronomical object across the sky. This rotation is purely a geometric effect and can be fixed by adjusting the phases (assuming R/L feeds).

The parallactic angle feed rotation which is the *P*-Jones in the RIME formulation (see Equation 3.3) is given as

$$P_i^{\odot} = \begin{bmatrix} e^{-j\alpha} & 0 \\ 0 & e^{j\alpha} \end{bmatrix}, \tag{3.6}$$

where $j = \sqrt{-1}$ and α is the parallactic angle.

The parallactic angle for an alt-az mount antenna is

$$\alpha = \tan^{-1}\left(\frac{\cos(lat)\sin(ha)}{\sin(lat)\cos(dec) - \cos(lat)\sin(dec)\cos(ha)}\right), \tag{3.7}$$

where lat is the antenna latitude, dec is the declination of the source and ha is the hour angle of the source.

The orientations of the VLBA feeds are mechanically adjusted and the exact values of the parallactic angles may not be known and thus it must be determined using calibration methods (Cotton, 1999).

For full or partial polarisation experiments, the parallactic angle contribution to the phase is typically removed at the very beginning of the phase calibration. This correction is important in phase referencing experiments, because the parallactic angle difference between the calibrator and target is different at different stations which leads to an extra phase error which must be corrected (Thompson et al., 2001). In this work the parallactic angle corrections were performed with the AIPS task VLBAPANG. VLBAPANG procedure uses the task CLCOR to copy the CL table versions and applies the phase correction using Equation 3.7.

[10] ALT-AZ means Altitude-Azimuth mount type telescope. Also known as Az-El mount type telescope

3.2.1.4 Absolute Amplitude Calibration

In amplitude calibration, a source with known parameters (source position, flux density, source structure) is used to convert the measured signal into physical units such as Janskys. This approach is possible with connected-element interferometry, but is very difficult to implement in VLBI. This is because of the unavailability of appropriate calibrator sources, since most VLBI sources are variable, and/or resolved and with no simple polarisation position angles.

The amplitudes of the visibility obtained in a VLBI observation in a baseline between the telescopes i and j has a form of a normalised cross-correlation coefficient and is calibrated using the formula below

$$S_{ij} = \rho \frac{A}{\eta_s} \sqrt{\frac{T_{\mathrm{si}} T_{\mathrm{sj}}}{SEFD_{\mathrm{i}} SEFD_{\mathrm{j}}}} \,, \tag{3.8}$$

where S_{ij} is the flux density on baseline $i-j$, ρ, the measured correlation coefficient, A is the correlator scaling factor, η_s is system efficiency including digitisation losses, T_s is the system temperature, which includes receiver, spillover, atmosphere and blockage, $SEFD_i$ and $SEFD_j$ are the system equivalent flux density at each antenna (see Section 2.2.2).

In this work antenna gain curves (measured every few months or years) and system noise temperatures measured during the observation were used to perform the amplitude calibration. The task ANTAB reads and creates gain curve (GC) and system noise temperature (TY) tables, which are used in VLBACALA procedure to apply a-priori amplitude corrections to the VLBA data.

The VLBACALA task determines amplitude corrections for digital sampling effects and applies a-priori corrections using TY, WX and GC tables. The VLBACALA task removes any outliers in the data and then applies these derived corrections to the highest numbered CL table. The VLBACALA procedure uses the tasks ACCOR, APCAL, SNSMO and CLCAL. Here, ACCOR corrects amplitudes in cross-correlation, then APCAL generates calibrated solutions (SN) using a default correction faction (APARM[1]=B) to correct any unwanted amplitude visibility offsets. SNSMO then smooths and filters these solutions. Outliers in the derived amplitude corrections are clipped and then finally CLCAL applies the smoothed solutions to the selected entries of the appropriate CL tables. An overview of the procedure contained in VLBACALA for the amplitude calibration steps applied in this work is shown as Figure 3.5.

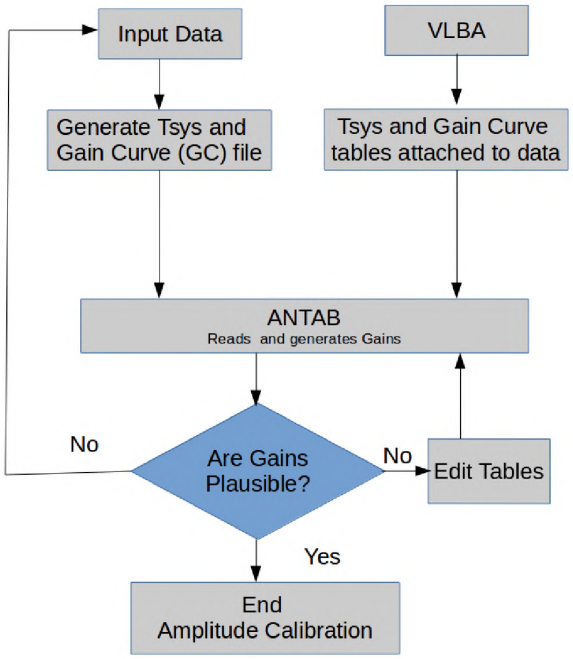

FIGURE 3.5: Block diagram of the steps involved in amplitude calibration of continuum data in AIPS.

The system temperature information for one of the epoch for this survey is presented here as Figure 3.6. Once the corrections are applied, the final $T_{\rm sys}$ values are then used to convert the data values from arbitrary units into Janskys (Jy).

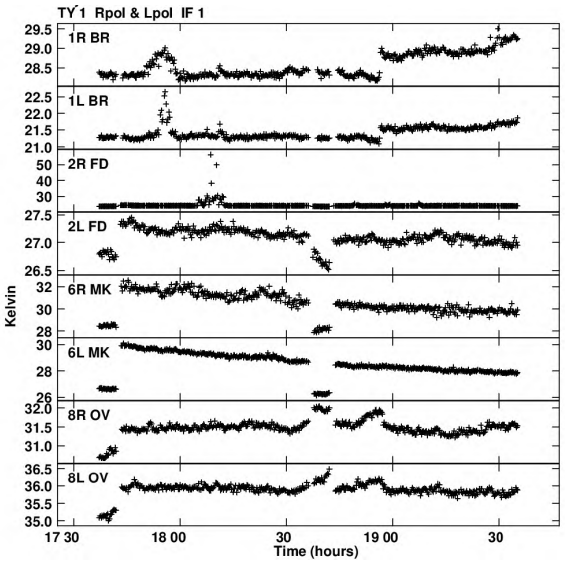

FIGURE 3.6: The plot shows the different system temperatures for an entire observation run for one of the epochs of four selected antennas, Brewster, Fort Davis, Owens Valley and Mauna Kea (BR , FD, OV, MK). The different temperatures are related to the amplitude calibrators, whereas the small ripple during the run is the change of $T_{\rm sys}$ between the target and the phase-reference source. The systematic errors (strange jumps) are smoothed and flagged out by the AIPS task SNSMO.

The successful implementation of the amplitude calibration is shown in Figure 3.7.

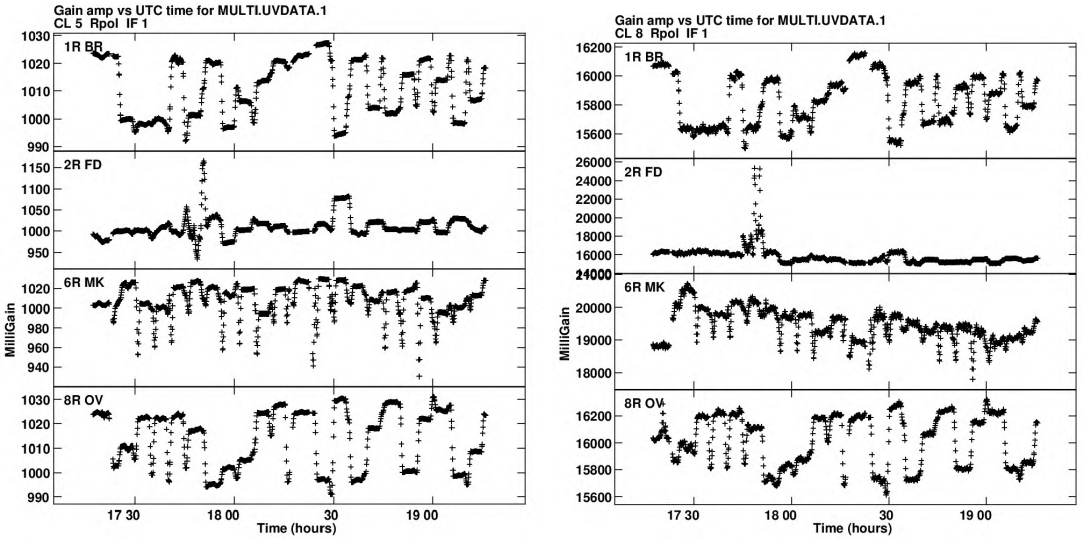

(A) (B)

FIGURE 3.7: Comparison of the gain curves (KJy^{-1}) before and after amplitude calibration of the gain calibrator on some selected antennas. (a) Uncalibrated amplitude of the gain calibrator source. (b) Increased amplitude of the scattered visibility demonstrating a successful implementation of amplitude calibration using the weather tables, system temperature and gain curves of the gain calibrator.

It can be seen from Figure 3.7 that as APCAL corrects amplitudes of the visibilities, the resultant scatter of the amplitudes has also increased by the scaling factor $\leqslant$B.

3.2.1.5 Delay And Rate Calibration

One of the methods used for phase calibration is phase referencing which has been described in Section 2.2.1. There are however other methods used for the phase calibration, namely, fringe-fitting and delay calibration. The next two subsections give details of these methods.

3.2.1.5.1 Instrumental Delay Calibration

Radio signals captured at the antenna receivers traverse through chains of electronic systems before they are finally correlated. These signals are transmitted through a range of different radio-electric devices (e.g. amplifiers, mixers, waveguides, cables) of which are neither identical nor at the same temperature across the different VLBI sites. These non-identical components and temperatures cause instrumental delays between IFs, polarisations and stations. There are two ways to estimate these instrumental delay:

- using pulsed phase-cals; and

- solving for delay only using bright sources.

Typically, the pulsed phase-cal systems injected into the signal path should correct for all the delays the signal undergoes during its transmission but in practice the phase-cal system itself is affected by spurious signals which can cause additional phase distortions. Mismodelling the phase distortion may cause major downstream phase error budgets as stipulated by Petrov (2000). The pulsed phase-cal system consists of a pulse generator and a sine-wave detector which are injected into the signal path at the receiver to correct phase offsets between the two station or oppositely polarised signal channels (Thompson & Bagri, 1991; Fomalont & Perley, 1999). The phase-cal system generates short pulses which are injected into a feed horn every microsecond. The phase of these phase-cal signals in the individual channels of the radio-electronics device is then used to measure the delay.

The second method used for estimating the instrumental delay is by using the AIPS task VLBAMPCL. The VLBAMPCL task calculates and applies manual instrumental phase calibration. This task also uses FRING and CLCAL and prepares the data for the actual fringe-fitting.

3.2.1.5.2 Fringe-Fitting

In a VLBI correlator, the recorded data are time-stamped and the correlator model (which is made up of a number of geometric corrections) determines which timestamps from the different stations are cross-correlated. Any remaining phase residuals or delay offsets due to an imperfect model are corrected for in post-processing. These imperfections are typically caused by:

- independent clocks with non-zero Allan variance (AVAR);
- tropospheric and ionospheric delays;
- imperfect antenna positions in the correlator model; and
- errors associated with the source positions.

Fringe-fitting is the process of solving the delay and/or rate residuals that may result from the above mentioned sources of errors. Simply put, fringe-fitting is performed by solving Equation 2.2, to obtain the errors via observation of a bright calibrator (phase referencing). The methods used for fringe-fitting are:

- baseline-based fringe-fitting; and
- global fringe-fitting.

Global fringe-fitting is a calibration technique for minimising the difference between model phases and the measured phases for station-based instrumental phases, its time slope (fringe rate) and the frequency slope (delay) (Schwab & Cotton, 1983; Cai et al., 1993). In this work we used global fringe-fitting. The motivations for choosing global fringe-fitting are:

- global fringe-fitting method preserves closure of the derived instrumental delays and rates whereas baseline based fringe-fitting does not; and
- global fringe-fitting approach lowers the threshold for flux density of the minimum detectable point source.

The general method of global fringe-fitting uses Equation 2.2 and all data to jointly estimate the antenna-based phase, delay and rate (Cotton, 1995). There are two methods involved in global fringe-fitting; a least square formulation method (Walker, 1995; Pearson, 1995) and Fourier transform method. The Fourier transform method uses a standard correlator-based fringe search approach to generate a starting guess for the least squares method (Schwab &

Cotton, 1983). The Fourier transform method also involves calibration of the phases within the intermediate frequencies.

The least-square formulation of this is to minimise

$$S(\mathbf{x}) = \sum_{\substack{0<k<n_t \\ 0<l<n_\nu}} \sum_{1\leq i<j\leq n} w_{ijkl} \| V_{ij}^{\text{obs}}(t_k, \nu_l) - a_i a_j V_{ij}^{\text{true}}(t_k, \nu_l) \varepsilon_{ijkl} \|^2 , \tag{3.9}$$

where $\mathbf{x}$ is the column vector of the unknown parameters given as $\mathbf{x} = \text{col}'(a_1 \ldots, a_n, \phi_{10}, \ldots, \phi_{n0}, r_1, \ldots, r_n, \tau_1, \ldots, \tau_n)$, the prime denoting an omission of antenna-based parameters[11]; w_{ijkl} denotes weight factors.

In this work, phase slopes were fitted in both frequency and time using the AIPS task FRING which utilises a global fringe-search method. This is achieved by setting an appropriate solution interval (SOLINT) and selecting a reference antenna [12] (REFANT) that is mostly present all of the time over the entire observation and close to the geographical centre of the array (Cotton, 1995).

The delay and rate results from FRING are typically stored in an AIPS solution table (SN)[13]. The solution tables are then either edited or smoothed (using the task SNSMO) in a variety of ways and then applied (using the AIPS task CLCAL) to the data. The schematics of the various steps used for fringe-fitting in this work are shown in Figure 3.8.

[11] The antenna parameters are antenna phases, rates and delays.
[12] Reference antenna, which by definition, is assigned, a zero phase (and delay) gain
[13] Solution table:contains solutions from AIPS tasks-e.g., FRING

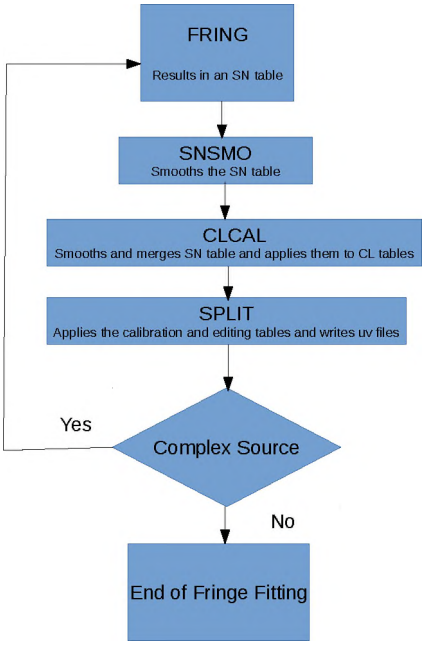

FIGURE 3.8: Block diagram of the steps involved in continuum VLBI fringe fitting. The details of the fringe fitting task can be found in Greisen (2003).

Figure 3.9 shows cross-power spectra of the raw phases and corrected phases in the data of the phase calibrator source from some selected baselines before and after implementation of fringe-fitting of one of the schedule blocks of the observation.

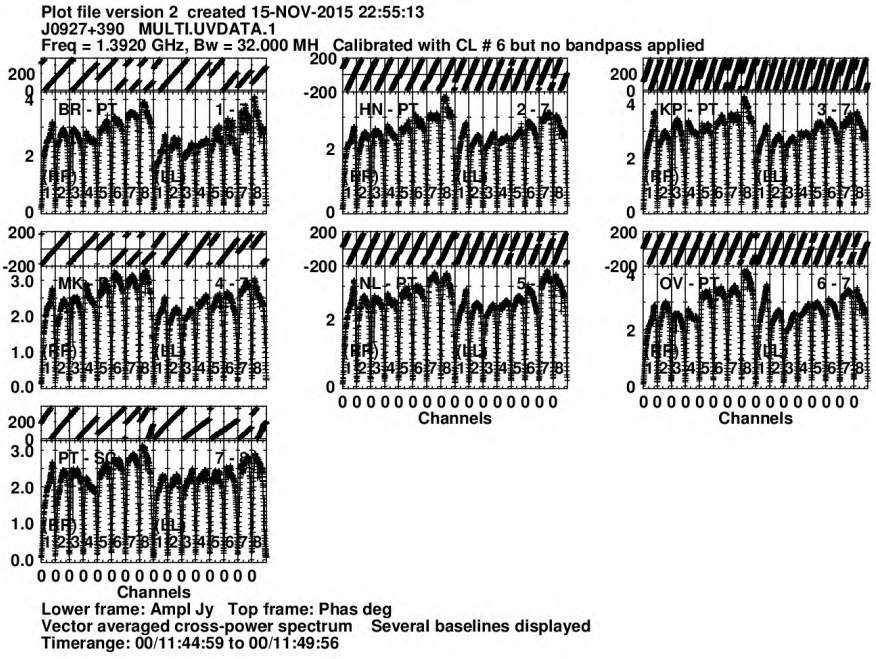

(A)

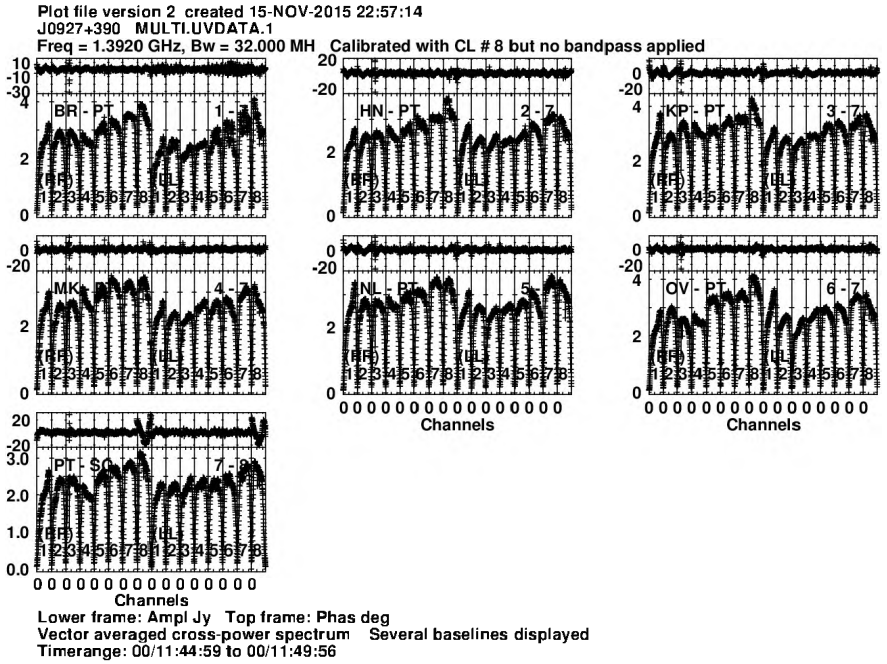

(B)

FIGURE 3.9: Fringe-Fitting: the plots of VLBI observation performed with 8 IFs of some selected VLBA baselines of the gain calibrator. The upper panels shows phase variations with frequency in degrees while the lower panels are the uncalibrated amplitudes in Jy. (a) The upper frame plot shows uncalibrated phase variations with frequency, within each IF. There are small phase slope caused by residual delay errors in the correlator model. (b) The upper frame plot shows the same data after a successfully corrected delay and fringe rate. The phases as a function of frequency are aligned around zero as expected although a few issues remain (e.g., IF8, PT-SC).

The waterfall[14] plots of the phases and amplitudes of the gain calibrator for one of the schedule blocks (C3) are shown in Figure 3.10. An inspection of Figure 3.10 reveals that the phases and amplitudes are uniform across all baselines.

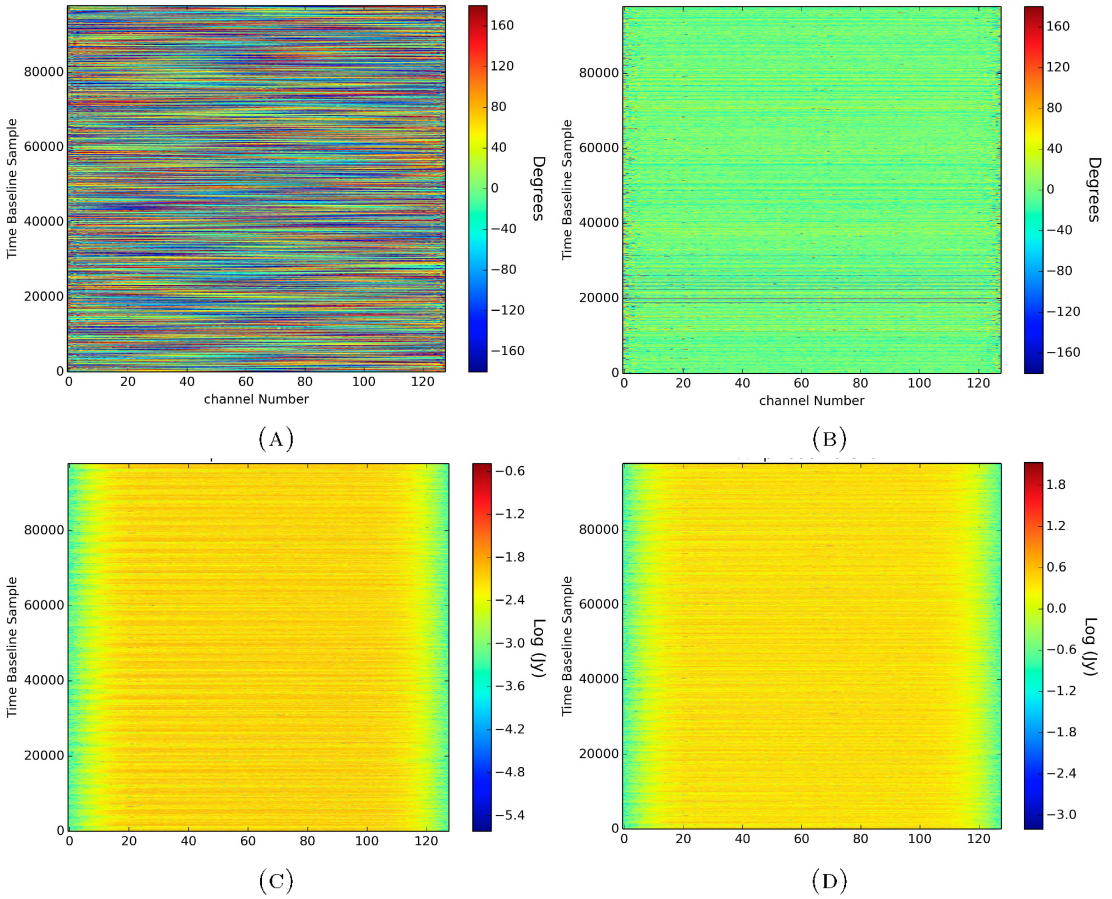

FIGURE 3.10: Waterfall plots of the fringe finder. (a) Waterfall plot of phase of the calibrator before fringe-fitting. (b) Phases of the calibrator sources after fringe-fitting. (c) Original amplitude of the calibrator sources before fringe-fitting. (d) Increased amplitude of the calibrator sources after fringe-fitting.

Figures 3.9 and 3.10 demonstrates how fringe-fitting corrects for delay and rate errors for on the phase calibrator(J0927+390).

3.2.1.6 Bandpass Calibration

Bandpass calibration is the process of solving and correcting for the frequency-dependent term of the complex gains in Equation 3.3. Any variations in the antenna gains must be corrected before averaging the different frequency channels. A good bandpass calibration is key for accurate measurement of spectral features in sources. Bandpass is dependent on electronic devices in individual antennas and their transmitting systems.

[14]Waterfall plot is a plot of time baseline sample versus channel numbers

Bandpass calibration is performed by observing a bandpass calibrator, whose spectral properties are well known. A good bandpass calibrator source is bright ($\geqslant 1$ Jy) with a flat spectrum. The bandpass gains are computed from the bandpass calibrator and then transferred to the target data.

In this work a bandpass source, J0927+390, was used as bandpass calibrator. The AIPS task BPASS was used to perform the bandpass calibration. After inspection and examination of the bandpass solutions, we discovered that there were too many failed solutions and the phases of the visibilities had worsened. In view of this, the bandpass solutions were not applied to the datasets.

3.2.1.7 Applying The Solutions

The final step of calibration in AIPS was to apply the full accumulated calibration solutions and tables from Section 3.2.1.1 up to Section 3.2.1.5.2 using the task SPLIT. The task SPLIT was used to split the multi-source files by applying the derived calibration tables into single-source *uv* files. Finally, the datasets are exported into UVFITS format using the task FITTP in preparation for further processing. This ends the calibration in AIPS. Next we describe post fringe-fitting calibration.

3.2.2 Post Fringe-Fitting Processing

In this section we describe all post fringe-fitting data processing. The data processing consists of self-calibration, RFI excision, wide-field imaging and source extraction. We also give a detailed description of the wide range of new algorithms and software packages used for the purpose of efficient post fringe-fitting processing.

The first step in the post fringe-fitting data processing is to convert the data from UVFITS format to measurement set (MS) format using CASA. The CASA task IMPORTUVFITS was used to achieve this. All subsequent processing of the visibilities (e.g. self-calibration, imaging) is performed in the MS format. Initial imaging of the gain calibrator and known VLBI sources is performed using CASA. WSCLEAN is then used to make wide-field images. The flow chart of the post fringe-fitting calibration of the data from self-calibration, through primary beam correction to imaging and source extraction is shown below

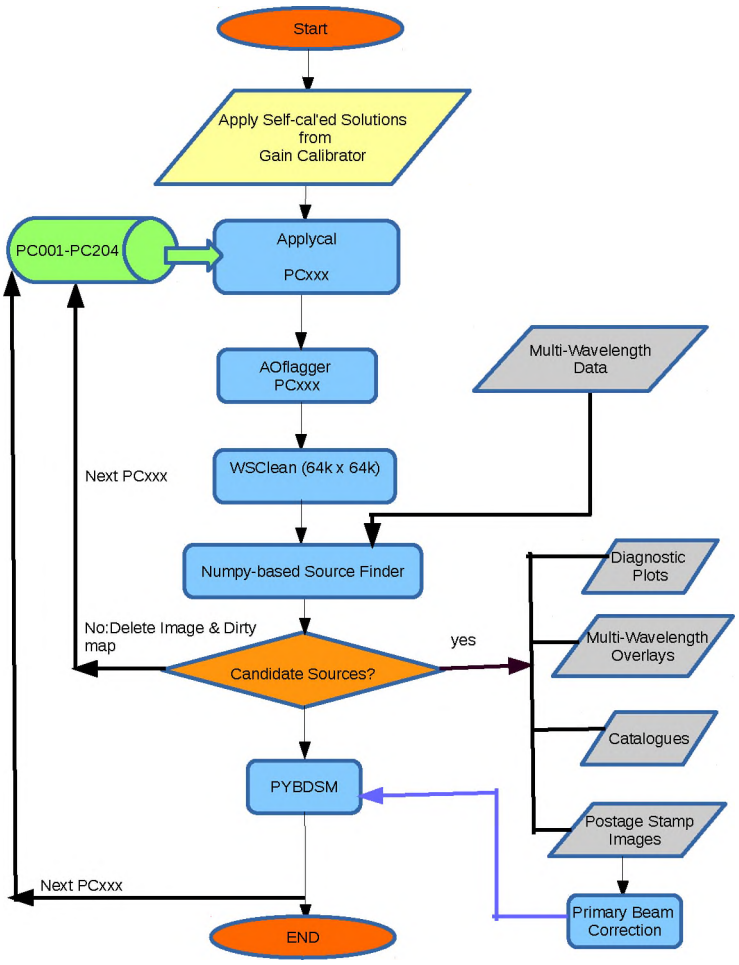

FIGURE 3.11: Post fringe-fitting calibration strategy.

3.2.2.1 RFI Excision

Radio Frequency Interference (RFI) is defined as unwanted signals in the radio spectrum picked up by a radio telescope, that typically interfere with the often weak astronomical signals. The major contributing factor to RFI is man-made sources of radio signals, such as wireless networks, satellites, cell phones, etc. RFI can suppress weak astronomical signals that are being studied (Rohlfs & Wilson, 2013) and thus have a detrimental impact on astronomical observations.

To detect RFI during scans of the gain calibrator and the target sources, we used AOFLAGGER (Offringa, 2010) which operates on visibilities in the MS format. Comprehensive details of the steps involved in AOFLAGGER are found in (Offringa et al., 2010, 2012, 2015). The various steps for the flagging are combined into one automated strategy which may be performed multiple times and with different combinations of the steps. We used the default

flagging strategy for all the datasets in this work since there is currently no specific RFI strategy for VLBA in AOFlagger.

An overview of the AOFlagger flagging implementation is presented in Offringa et al. 2010. The flagger is executed on the available amplitude information in the MS of each polarization of a single sub-band of each baseline (Offringa et al., 2010).

Figure 3.12 shows the implemented AOFlagger strategy for a single baseline during a scan of the fringe finder (J0927+390).

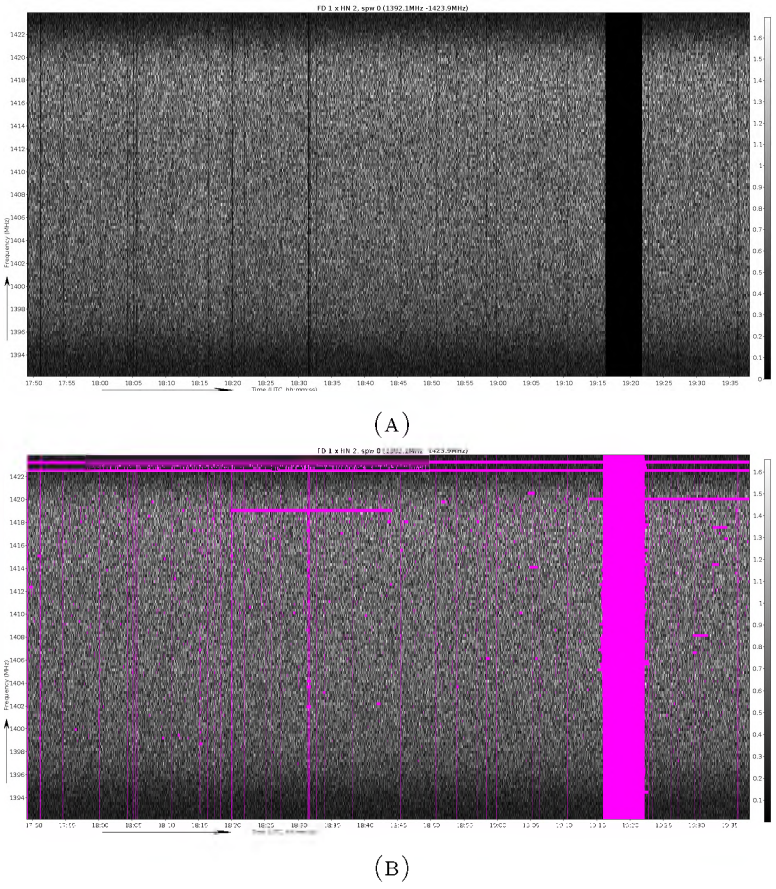

(A)

(B)

FIGURE 3.12: Comparison of an unflagged and flagged visibility of the phase centre PC000. (a) Unflagged visibility of the calibrator source with frequency on the y-axis and time on the x-axis. (b) Successfully flagged visibility of the target field PC000. The pink samples were set by the SumThreshold algorithm and flagged appropriately.

The statistics of the data flagged in two selected epochs of the twelve selected phase centres is shown in Table 3.1.

TABLE 3.1: Comparison of RFI strategy in both polarisations for selected schedule blocks. The percentages represents the amount of data which were flagged by AOFLAGGER.

Percentage of RFI Flagged				
Phase Centre	RR Polarization (%)		LL Polarisation (%)	
Schedule block	A2	C3	A2	C3
PC049	11.1	6.4	10	5.4
PC055	11.2	5.3	9.9	4.2
PC081	10.7	5.3	10.2	4.2
PC085	10.6	5.3	9.9	4.2
PC097	10.5	5.2	9.3	4.1
PC110	10.5	5.2	9.4	4.2
PC111	10.7	5.2	9.6	4.1
PC156	10.9	5.2	10.3	4.1
PC160	10.7	6.8	10.1	5.7
PC164	11.1	6.9	9.8	5.8
PC182	11.1	5.5	10.2	4.4
PC183	11.0	6.2	10.2	5.1

Schedule blocks ABCDE represents elevations during the observation. Schedule block C has the highest elevation. The next higher elevation are schedule blocks B and D, while A and E have the lowest.

Schedule block A has lower elevation[15], and has a higher probability of being affected by RFI and this reflects in the higher fraction of flagged data as can be seen from Table 3.1.

3.2.2.2 CASA Self-Calibration

VLBI visibilities obtained directly from correlators are of very little use in making images of astronomical sources (Pearson & Readhead, 1984) because even after fringe-fitting, averaging and RFI removal, calibration errors on sub-scan intervals remain. One method used to solve for this phase variation is self-calibration. Self-calibration is the process of using available source structure information to improve the antenna phase and amplitude gain solutions. The visibility data set, corrected with the improved gains, is then used to produce an updated model of the source. This typically results in decreasing image rms. Self-calibration is based on the assumption that all the errors in the visibility phase can be described as antenna based (Pearson & Readhead, 1984). This is generally valid because each baseline gives independent information about the sources: using this information allows us improve the gain estimates. One approach for improving the gain estimate is the least-square method. The least-squares procedure involves fitting for the complex antenna gains:

$$\Delta S = \sum_{k} \sum_{i,j}^{i \neq j} w_{ij}(t_k) \| \mathbf{V}_{ij}^{\mathrm{obs}}(t_k) - \mathbf{J}_i(t_k) \mathbf{V}_{ij}^{\mathrm{model}}(t_k) \mathbf{J}_j^*(t_k) \|^2 , \tag{3.10}$$

[15]The elevation values can be inferred from the source coordinates, station coordinates and the time, all recorded as meta-data in the MS.

where $\mathbf{V}_{ij}^{\text{model}}(t_k)$ are the model visibilities at time t_k, $\mathbf{V}_{ij}^{\text{obs}}(t_k)$ are the observed visibilities, and w_{ij} denotes a-priori weight of each data point at time t_k.

It is good practice that solution intervals are kept relatively short so as to track atmospheric phase changes with a high degree of accuracy (Walker, 1995). This also means there will be more free parameters and it becomes easier for the solver to find best fit solutions, if sufficiently high SNR is available (Cornwell & Fomalont, 1989a).

The algorithm used for the self-calibration in this work is shown in Figure 3.13.

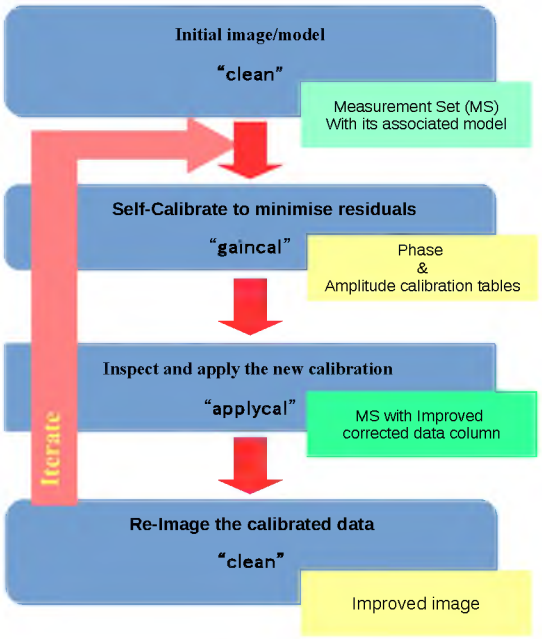

FIGURE 3.13: Self calibration procedure used on the gain calibrator J1234+619.

The details of the self-calibration approach in Figure 3.13 are summarised by the following steps:

1. A well-resolved calibrator source with a known flux of 17 mJy (measured in this work and Chi et al., 2013, survey) was used as an starting model, $\mathbf{V}_0^{\text{model}}$ (by setting the parameter SMODEL = 17 mJy in GAINCAL[16]) to find a gain matrix $\mathbf{J}_0$, that minimises Equation 3.10 by a least square method and then computes the corrected data using

[16] GAINCAL is a task in CASA that determines temporal gains (time-dependent or frequency-independent complex gains) from a calibrator source

Equation 3.4 by applying the gain solution using the CASA task APPLYCAL. A solution interval of 15 minutes is chosen for the initial phase-only self-calibration (using the GAINCAL parameters CALMODE='p' and SOLINT='15mins') because solution intervals greater than 15 minutes did not improve the image as the true phase variations are on significantly shorter time scales.

2. An improved model, $\mathbf{V}_{i-1}^{\mathrm{model}}$ is extracted from the corrected visibilities by making CASA CLEAN image of the calibrator source.

3. The improved model from Step **2**, $\mathbf{V}_{i-1}^{\mathrm{model}}$, is then used in another round of calibration step and a new gain matrix, $\mathbf{J}_{i-1}$, then compute the corrected visibilities.

4. Steps **2** and **3** is repeated by performing a phase-only calibration (by setting CALMODE='p' and SOLINT='5mins') and then repeatedly decreasing the solution interval to 2 min, 1 min and finally to 30 sec in order to re-calibrate with the improved image as model. The number of iterations was set to 100 (NITER=100) to avoid artefacts in the model.

5. The procedure from Step **1** to Step **4** is then repeated for all 12 epochs.

6. After removing the instrumental phases, the improved visibilities are used to generate an updated model using all the corrected visibilities of the calibrator source from all epochs. The updated model was obtained by making a clean image of the gain calibrators with the full datasets from all 12 epochs.

7. A new, improved model for each epoch is then made by using the updated model in Step **6**. This was achieved by making images from each epoch.

8. Step **1** to Step **4** is also repeated for each epoch using two cycles of a 10 min and 5 min solution intervals for the amplitude & phase solutions.

9. Finally, the derived phase calibrator gains from Steps **1** to **8** are then applied to the target source datasets.

Images of the gain calibrator are shown below

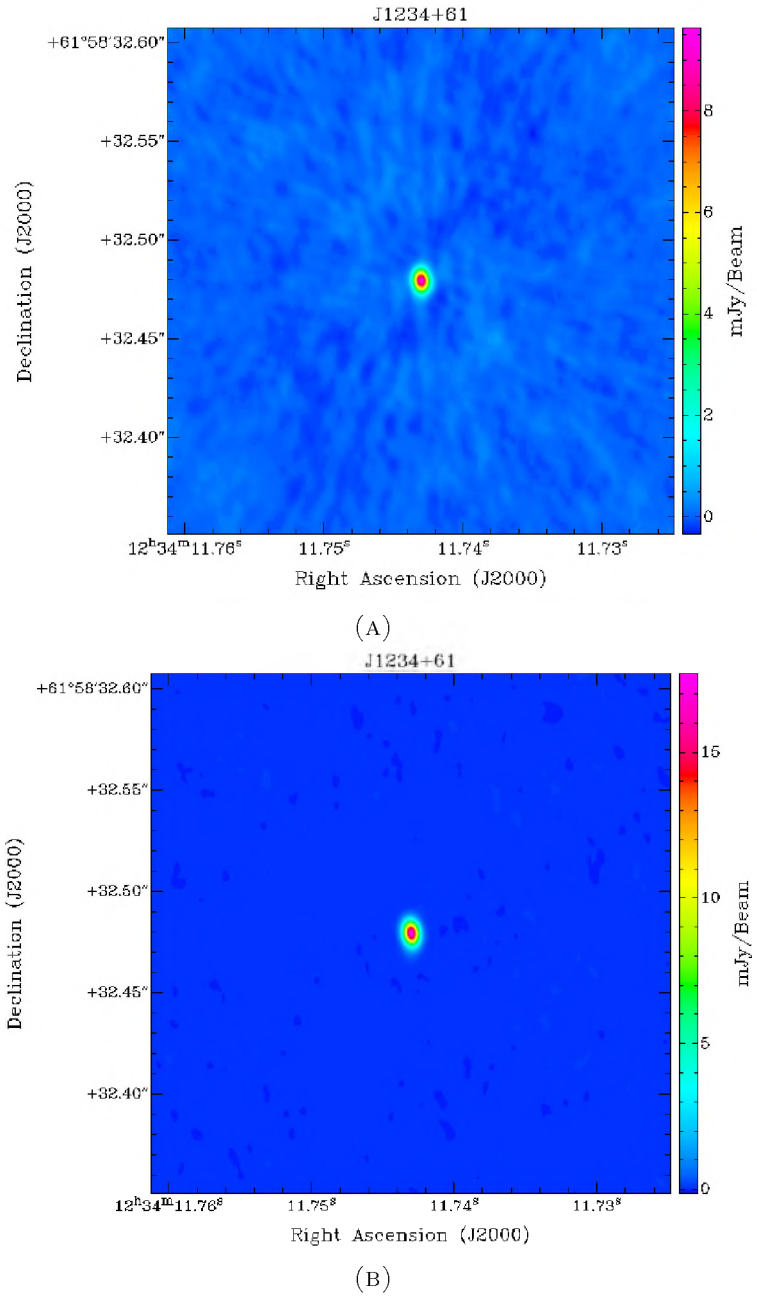

FIGURE 3.14: Comparison of the initial and final step of self-calibrated images of the gain calibrator.(a) Image of the initial step self-calibration of the gain calibrator, J1234+619 with peak flux of 9.48 mJy/beam and an rms of 83.63 μJy/beam (b) Image of the final 5 minutes amplitude and phase self-calibration of the gain calibrator, J1234+619 with peak flux of 17.64 mJy/beam and an RMS of 20.10 μJy/beam.

As demonstrated in Figure 3.14, we see that the gain calibrator is a point source as it appears resolved and there is also a significant improvement of the noise (see Table 3.2).

The statistics of the self-calibration cycles used on the gain calibrator source are shown in Table 3.2.

TABLE 3.2: Calibrator statistics during self-calibration.

Self-calibration statistics of the gain calibrator					
Solution Interval (min)	Free Parameter	Integrated Flux (mJy)	Integrated Flux RMS (μJy)	Peak Flux (mJy/beam)	Peak Flux RMS (μJy/beam)
15	phase	10.9	±142	9.5	±83.6
5	phase	18.7	±75	17.3	±34.6
2	phase	18.7	±75	17.4	±34.4
1	phase	18.8	±75	17.4	±34.3
0.5	phase	19.1	±75	17.8	±34.4
10	amplitude& phase	18.7	±44	17.7	±19.3
5	amplitude& phase	18.5	±46	17.7	±20.1

Here, we see from Table 3.2, that there was an increase in flux density (column 5) and a considerable decrease in the rms (column 6) as the solution intervals were decreased using the phase-only gain solution. Secondly, the rms of the gain calibrator images decreased further ($\sim 42\%$) after self-calibration with amplitude and phase as free parameters.

3.2.2.3 Imaging

The visibilities as mentioned in Section 1.2 are represented by Equation 1.25 and the van Cittert-Zernike theorem (McCutchen, 1966; Carozzi & Woan, 2009), where $I_B(l,m) = A(l,m)I(l,m)$ is the modified sky brightness distribution.

These visibilities are measured at discrete points of the sky (u,v) and so we only sample a percentage of the total visibility, thus the measured visibility consists of the total visibility multiplied by a sampling function

$$V^{'}(u,v) = S(u,v) \int_{-\infty}^{+\infty}\int_{-\infty}^{+\infty} I_B(l,m)\mathrm{e}^{-i2\pi(ul+vm)}\ dldm\ , \tag{3.11}$$

where $S(u,v)$ is the sampling function.

This translates to a convolution in the Fourier domain where the true image is convolved with the Fourier transform of the sampling function (also known as point spread function, PSF[17]). This combination is generally called the dirty imaging. The dirty image is the sensitive pattern obtained by Fourier transforming the points in the *uv*-plane. Hence, one

[17]Point spread function is defined as the response of an imaging system (array) to a point source.

of the fundamental steps in radio astronomy imaging is deconvolution where we attempt to separate the true image from the PSF. This is illustrated with Equations 3.12

$$I_{\rm D}(l,m) = \int_{-\infty}^{+\infty}\int_{-\infty}^{+\infty} V^{'}(u,v)S(u,v)\mathrm{e}^{i2\pi(ul+vm)}\ dudv, \tag{3.12a}$$

$$I_{\rm D} = I \otimes PSF, \tag{3.12b}$$

$$PSF = \int_{-\infty}^{+\infty}\int_{-\infty}^{+\infty} S(u,v)\mathrm{e}^{i2\pi(ul+vm)}\ dudv\ , \tag{3.12c}$$

where $I_{\rm D}(l,m)$ is the dirty image, $V^{'}$ denotes noise-corrupted observed visibility data, $\otimes$ is the convolution operator and I is the true sky.

In this work, the implementation of the CLEAN algorithm in CASA (Högbom, 1974) was used for the deconvolution. CLEAN considers the sky intensity to consist of a collection of point sources. Thus the dirty image can be represented by multiple scaled and centred point spread functions. The principal steps in the CLEAN algorithm are summarised as:

1. The image and the response to a point source are computed by Fourier transforming the visibility and the weighted transfer function in Equation 3.10.
2. The highest intensity point of the image is then located and the dirty beam multiplied by the peak amplitude and the loop gain factor,γ is subtracted from the dirty image at this location. We choose γ=0.1 for this work.
3. The position and amplitude of the component removed in Step **2** are recorded by inserting a delta[18] function component into a model that would become the cleaned image.
4. Next, return to Step **2** and repeat the process iteratively until the given iterative value limits are reached. Dirty images (NITER=0 and NPERCYCLE=30) were made in order to avoid artefacts in the model.
5. The delta functions in the cleaned model is now convolved with an idealised CLEAN-beam response.The CLEAN beam is usually an elliptical Gaussian with a half-amplitude width equal to the dirty beam.

[18]A delta function is defined as a function which is zero everywhere except at a single point, while at that point it is infinite in such a way that its integral over the real line is equal to one and given as $f(a) = \int_{-\infty}^{+\infty} f(x)\delta(x-a)\,dx$.

6. Finally, the residuals from Step **3** are then added to the CLEANed beam image which is then the final output of the process.

There are variants of the CLEAN implementation but the basic algorithm is almost always the same. The basic structure is presented in (Högbom, 1974). In order to make images to compare with the sources detected by Chi et al. (2013), we made 256×256 images centred on the RA (Right Ascension) and DEC (Declination) positions of the detected sources using the CASA imager. These images were made using pixel size of 0.5 mas. A summary of the survey details by Chi et al. (2013) is presented in Appendix A. The results of the detected sources from the CASA imaging is presented in Section 4.1.

3.2.2.4 WSCLEAN Wide-field Imaging

Wide-field (64k × 64k pixel) images were made using WSCLEAN (Cornwell & Fomalont, 1989b; Offringa et al., 2014), which is a wide-field astronomical imaging tool for radio interferometric data, written in C++ language. The 64k × 64k pixel images are of the target field, while the 256 × 256 pixel images are of the calibrator. WSCLEAN stands for 'w-stacking clean' which is an alternative to the w-projection algorithms (Cornwell et al., 2008). The core principle of w-projection is to multiply the intensity distribution by a w-dependence phase screen (Cornwell et al., 2008). In WSCLEAN, visibilities are read from MS and they are output as images in FITS file format or optionally as CASA image files (Offringa et al., 2014).

WSCLEAN imaging tool was chosen because it provides better processing/computing speed for the wide-field imaging when compared to other imaging tools like CASA which runs out of memory when used for the 64k × 64k pixel wide-field imaging.

A full derivation of the w-stacking method used in WSCLEAN can be found in (Offringa et al., 2014; Cornwell & Fomalont, 1989b).

In this work, the default number of w-layers (NWLAYERS = 128) was chosen for the imaging. The size of the image was chosen to be 64k×64k pixels (-SIZE = 2^{16}), while the cell size was chosen as 1.2 mas (-SCALE = '0.0012arcsec'). 'Natural' weighting was used and a dirty map (-NITER = 0) was made because most of the sources have sub-mJy flux densities and their sidelobes would not affect detection of other sources. WSCLEAN default values were used in addition to the above parameters. After successfully imaging the datasets, primary beam gains are applied to correct for amplitude attenuation.

3.2.2.5 Primary Beam Correction

The primary beam of an antenna is defined as the gain of the antenna as a function of its direction. The primary beam is also the Fourier Transform (FT) of the aperture illumination function. Typically, parabolic dishes have the maximum sensitivity at the pointing centre and the sensitivity drops off radially.

Fundamentally, the field of view in a VLBI observation is limited only by the primary antenna beams of the participating antennas (Keimpema et al., 2015). Primary beam attenuation is negligible in standard VLBI observations, as typically only a small fraction of the FoV is processed (Middelberg et al., 2011). The reason for the primary beam correction for this work is because we image a significant fraction of the primary beam. The observation of the survey of the GOODS-North field was performed within 80% of the primary beam of the VLBA and this is well approximated by analytical functions such (Gaussians, Sinc, Airy Disk models), which suffices for this thesis.

In this work, two analytic models for the primary beam corrections were considered, namely, Gaussian and Airy Disk models. Using a Gaussian model to correct the primary beam was implemented by Middelberg et al. (2013). This model was found to effectively model the main lobe of the antenna's power pattern response because it provided good approximation and is conveniently described by a single parameter to represent its properties; which is the full width at half maximum (FWHM; Middelberg et al. 2013). The Gaussian model, however, deviated beyond the first null of the antenna power pattern.

In this work, we used the more accurate model, the Airy Disk (Harrison et al., 2012) which is a Bessel function of order one and is also known as the Fraunhofer illumination pattern. The Airy Disk is given by Equation

$$I(\theta) = I_0 \times \left(\frac{2J_1(\frac{\pi}{\lambda} D \sin\theta)}{\frac{\pi}{\lambda} D \sin\theta} \right)^2 , \tag{3.13}$$

where D is the diameter of the dish, J_1 is the Bessel function of first order, λ is the wavelength of the observation and θ is the angular distance of which the intensity is to be determined. I_0 is set to unity since we are only interested in the deviations from the on-axis gain.

Figure 3.15 is the beam attenuation as a function of radial distances from the pointing centre

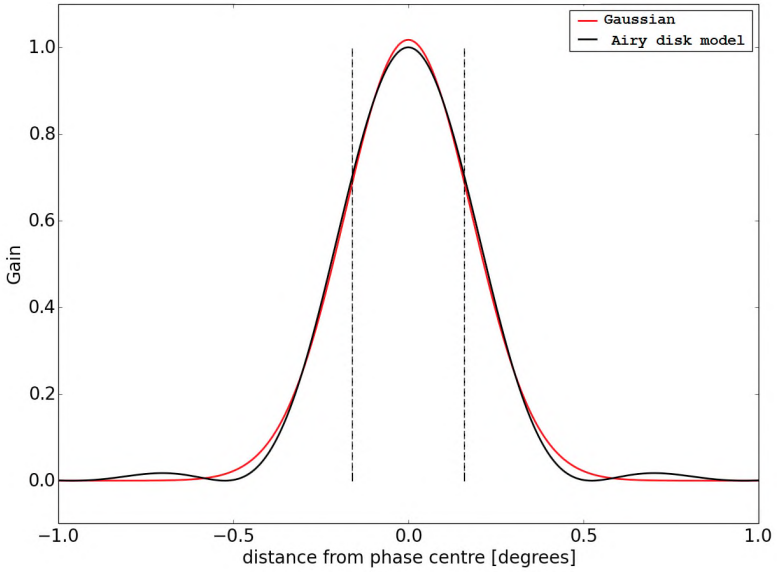

FIGURE 3.15: Plot showing a comparison of the Airy Disk model and the Gaussian. The dashed line corresponds to the maximum angular distance of ± 9.6 arcmin (± 0.16 degrees) between the most farthest phase centre (PC204) and the antenna pointing centre and this means that an image of PC204 will have the greatest primary beam attenuation of all the phase centres. Thus the space within the dashed lines shows where most of the sources were detected within the primary beam.

The primary beam correction strategy used in this work has been detailed in (Morgan et al., 2011) and has also been implemented by Middelberg et al. (2013). An application of this method is used to derive the primary beam gain and to correct for the attenuated flux density. Figure 3.16 is a plot of peak brightness and the corrected flux of the eleven (11) detected sources.

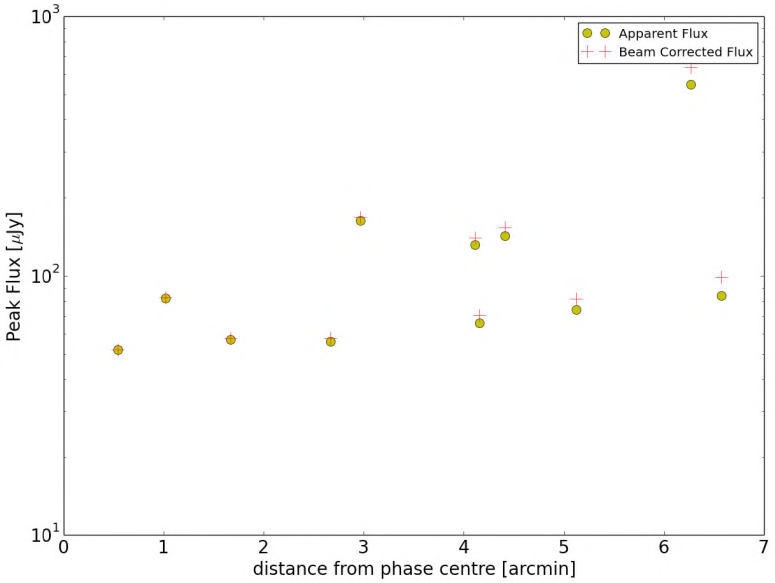

FIGURE 3.16: A comparison of the apparent flux versus primary-beam corrected flux of the 11 known sources detected in this work.

The table below (Table 3.3) is a comparison of the flux values and rms of the 11 known detections before and after application of the primary beam corrections.

TABLE 3.3: Comparison of apparent flux and RMS before and after primary-beam correction of the Known detected sources in this survey.

Compare							
PC Number	Source Name	Peak Flux (μ Jy/beam)	Integrated Flux (μJy)	Angular Distance[1] (arcmin)	Primary Beam Gain	PB[2] Peak Flux (μJy)	PB Integrated Flux (μJy/beam)
049	J123623+621642	129±13	301±12	4.41	0.90	143±15	335±14
055	J123716+621733	60±12	255±12	4.16	0.911	66±13	280±13
085	J123716+621512	53±13	114±13	2.67	0.963	56±14	119±23
097	J123652+621444	52±11	60±11	0.54	0.998	52±11	60±11
110	J123642+621331	57±6	626±12	1.67	0.985	57±9	636±12
111	J123646+621404	81±12	188±11	1.02	0.994	82±12	189±12
156	J123644+621133	156±13	227±12	2.97	0.954	163±13	238±11
160	J123721+621129	120±13	270±12	4.11	0.913	132±15	296±13
164	J123608+621035	67±12	126±11	6.57	0.790	84±15	159±15
182	J123700+620909	65±12	180±12	5.12	0.867	74±14	208±14
183	J123714+620823	442±27	2065±28	6.31	0.805	549±33	2565±34

[1] Angular distances were calculated using the source positions and the pointing centre of the VLBA.
[2] PB denotes Primary Beam

After applying the primary beam correction to the visibilities we then go forward with source extraction in the image domain.

3.2.2.6 Source Extraction

Source extraction was performed using PyBDSM (Mohan & Rafferty, 2015) and the purpose-built source finder. The python blob detection and source measurement (PyBDSM) software is a tool designed to decompose radio interferometry images into sources and make their properties available for further use (Mohan & Rafferty, 2015). The former is used to extract source parameters in the 512×512 postage-stamp images of the known sources while the latter is used to search for candidate sources in the 64k×64k wide-field images. Details of the source finders are discussed in the next two sections.

3.2.2.6.1 Purpose-Built Wide-Field Source Finder

The numpy-based source finder was developed by Dr Roger Deane.

Initial implementation of source finding for the wide-field images (64k×64k) was attempted using PyBDSM. It was concluded that the standard source finding packages were too computationally expensive for 64k×64k images particularly, given the low source density of the VLBI sky. Secondly, inclusion of ancillary multi-wavelength data is not possible in the existing source finders. This led to the development of a new purpose-built source finder written in python that included the multi-wavelength data.

For computing efficiency and calculation of the local rms, the 64k×64k images are sub-divided into 64 sub-images, with 1.2 mas pixel size and image size of 1024×1024 (ie, 65536/64=1024) pixels. The source extraction strategy used in this work is illustrated in Figure 3.17.

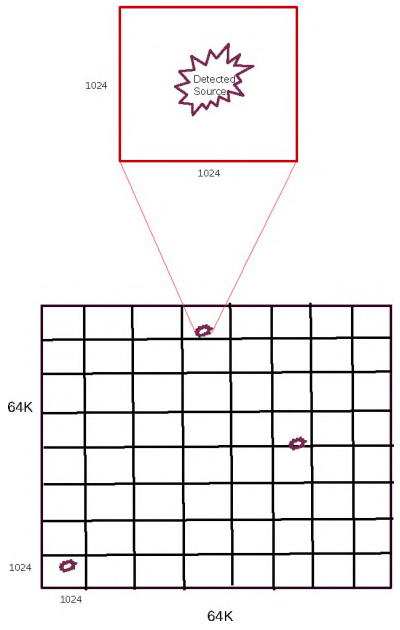

FIGURE 3.17: The source extraction schematics used for the wield-field imaging. Each small rectangular box represents a 1024×1024 pixel image. This was devised in order to optimise the array size in the maximum pixel and standard deviation calculation of the 64k×64k pixel images, while incorporating local noise level.

The standard deviation of the sub-images are the local rms of the sub-images. The maximum SNR is computed as flux density of the maximum pixel divided by the local rms flux density of the 1024×1024 sub-image. The maximum SNR for one of the sub-images of the wide-field is shown in Figure 3.18.

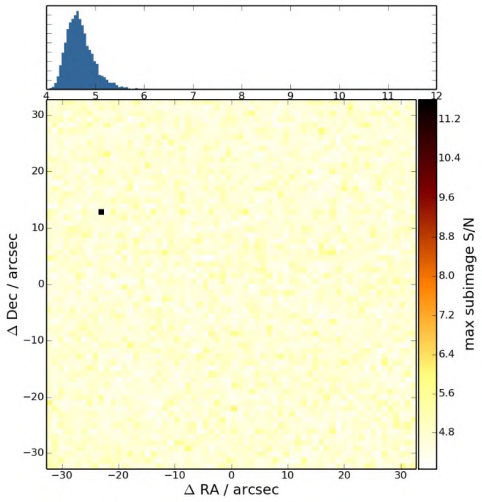

FIGURE 3.18: A 1024 × 1024 pixel map, where each pixel represents the maximum local SNR from 64k×64k VLBI image of phase centre PC110. As can be seen in this image, the small black dot in the above image has a higher likelihood to be classified as a real source because it has a high SNR.

The sub-images are then convolved with a 2-D Gaussian Kernel function (smoothing[19]). The Gaussian Kernel function were used as matched filters (Turin, 1960) to optimise the SNR by lowering the PSF sidelobes, optimising edge detections and removing high spatial components from the images. In this work, three iterative smoothing cycles were performed to optimise the detection probability of extended sources.

The results of the smoothing as can be seen in Figure 3.19, demonstrates improved SNR due to the applied smoothing iterations.

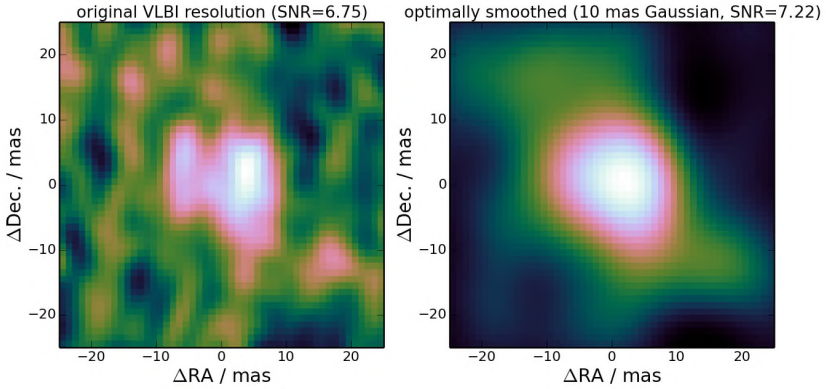

FIGURE 3.19: The image on the left is the original VLBI detected candidate while the image on the right is an optimally smoothed imaged of the same VLBI detected candidate showing an increase in SNR.

Next, multi-wavelength catalogues and the positions of sources from *Chandra* (X-ray; Weisskopf et al. 2000; Alexander et al. 2003; Brandt et al. 2001), *Spitzer* (NIR; Pilbratt et al. 2010; Elbaz et al. 2011; Ashby et al. 2015a) , 3D-*HST* (optical; Momcheva et al. 2013; Davis 2006; Ashby et al. 2015b) and VLA 1.4 GHz (radio; Morrison et al. 2010b,a) data are loaded in.

Counterparts to the VLBI candidate sources were searched using catalogue from Momcheva et al. (2016), Alexander et al. (2003), Morrison et al. (2010b) and Ashby et al. (2015a) of the GOODS-North field. The VLBI candidate sources of the GOODS-North extragalactic field are then compared with the positions of the multi-wavelength catalogue. The catalogues are then cross-matched to the GOODS-North data by calculating the angular distance of the locations of the radio, optical, X-ray and NIR positions to ensure that the emissions originated from the same astronomical objects. This is because of the depth of the available data and the high astrometric accuracy of the VLBA observations. This means that a simple match in coordinates will enhance the plausibility of a VLBI candidate source. A brief overview of these multi-wavelength catalogues and surveys that were used to complement the VLBI results are

[19]The Gaussian smoothing is an approximation to model the PSF to the image pixels, to obtain a new image with the probability that each pixel has the likelihood to be part of the object been searched for (Masias et al., 2012).

found in Appendix A. By using the catalogues from the surveys described in Appendix A, the conditions under which a VLBI candidate source is considered as a candidate source are:

- VLBI SNR $\geq 7\sigma$. This is because any peak brightness with SNR $\geqslant 7\sigma$ is more likely to be a source rather than a noise spike, assuming its only real sources that could make the distribution non-Gaussian (Rampadarath et al., 2015); and
- $5.5\sigma \leqslant$ VLBI SNR$< 7\sigma$ and the VLBI position is within 0.5 arcsec of a multi-wavelength source.

These two SNR threshold criteria stated above were chosen based on the large number of pixels per the 64k×64k images in this work because a threshold of 5σ would correspond to ∼729 false positive sources (see Figure 4.22). A small postage stamp (1024×1024) image centred on the VLBI candidate source is then made.

The postage stamp around the image (as insert) produced from the maximum SNR (Figure 3.18) map is shown as Figure 3.20.

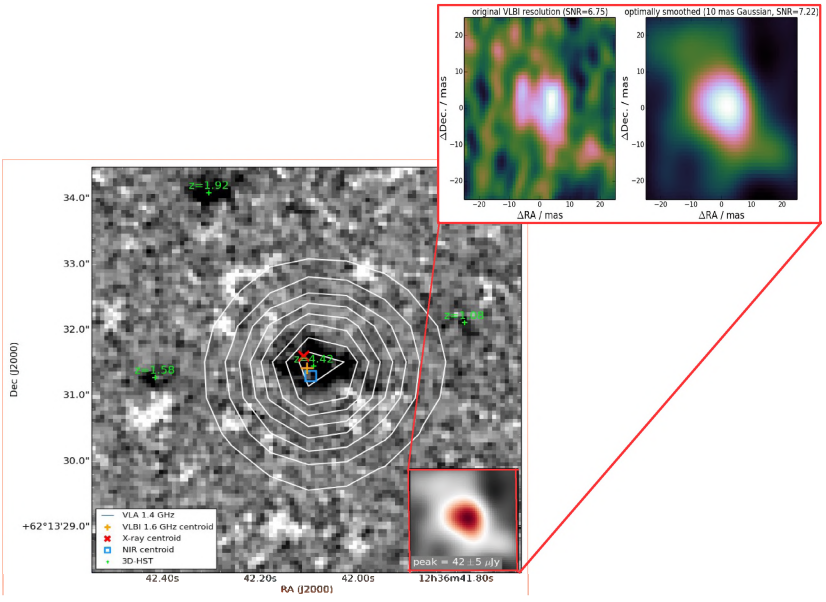

FIGURE 3.20: Clear Detection: The centroid of the greyscale image is the centre of the galaxy, whereas the contours around the source is a VLA detection position range. The greyscale image is an HST F814W image of the GOODS-North field. The orange + symbol in the greyscale image is the VLBI candidate source centroid, while the positions of the X-ray, NIR and optical counterparts are indicated by red ×, blue square, green + symbols respectively.

Next, the closest known source in arcsec in the NIR, HST, X-ray and VLA catalogues respectively are determined. Then an image clip is made out from the lower resolution (∼ 1.5 arcsec) VLA map of the GOODS-North. Finally, a multi-wavelength image is made, centred

on the VLBI candidate source and a catalogue of the source is saved. Furthermore, information about the source, such as the peak flux, photometric redshifts, angular distances and SNR values are extracted from the source. Next, PyBDSM is conveniently run on the postage stamp images to extract other needed source information.

3.2.2.6.2 Source extraction using PyBDSM

In order to extract the sources and basic statistics from the snapshot images (512×512 pixels) from CASA and the postage stamp images (1024×1024 pixels) from the wide-field, we used the PyBDSM source finder. Source finding algorithms like those employed in PyBDSM conventionally searches and groups pixels in an image that is considered to belong to an astronomical object. The major steps involved are:

- background estimation and subtraction;
- source identification;
- source characterisation and measurement; and
- cataloguing.

Details of these mentioned steps above are found in (Mohan & Rafferty, 2015).

For the 512×512 pixel images, we choose a 7σ threshold as the island peak and 5σ as the source detection threshold which is also the limit at which the flux is included in the source fitting. The 7σ threshold corresponds to a relatively small number ($\lesssim 10^{-6}$) of false positive sources per the 512×512 images and so sources detected at these thresholds are real rather than spurious. Similarly, a threshold of 5σ and 3σ were respectively chosen as island peak and detection thresholds for the 1024×1024 pixel images from the wide-field imaging. We chose a source list (CATALOG_TYPE='srl') which is formed by grouping Gaussians as the output catalog type because we want to compare the total source flux densities of the VLBI candidate sources from the wide-field snap shot images with other catalogues (Mohan & Rafferty, 2015). The uncertainties on the fitted parameters are computed following derivations from Condon (1997).

The figure made by the PyBDSM task PROCESS_IMAGE for an interactive extraction of a source from an image is shown in Figure 3.21.

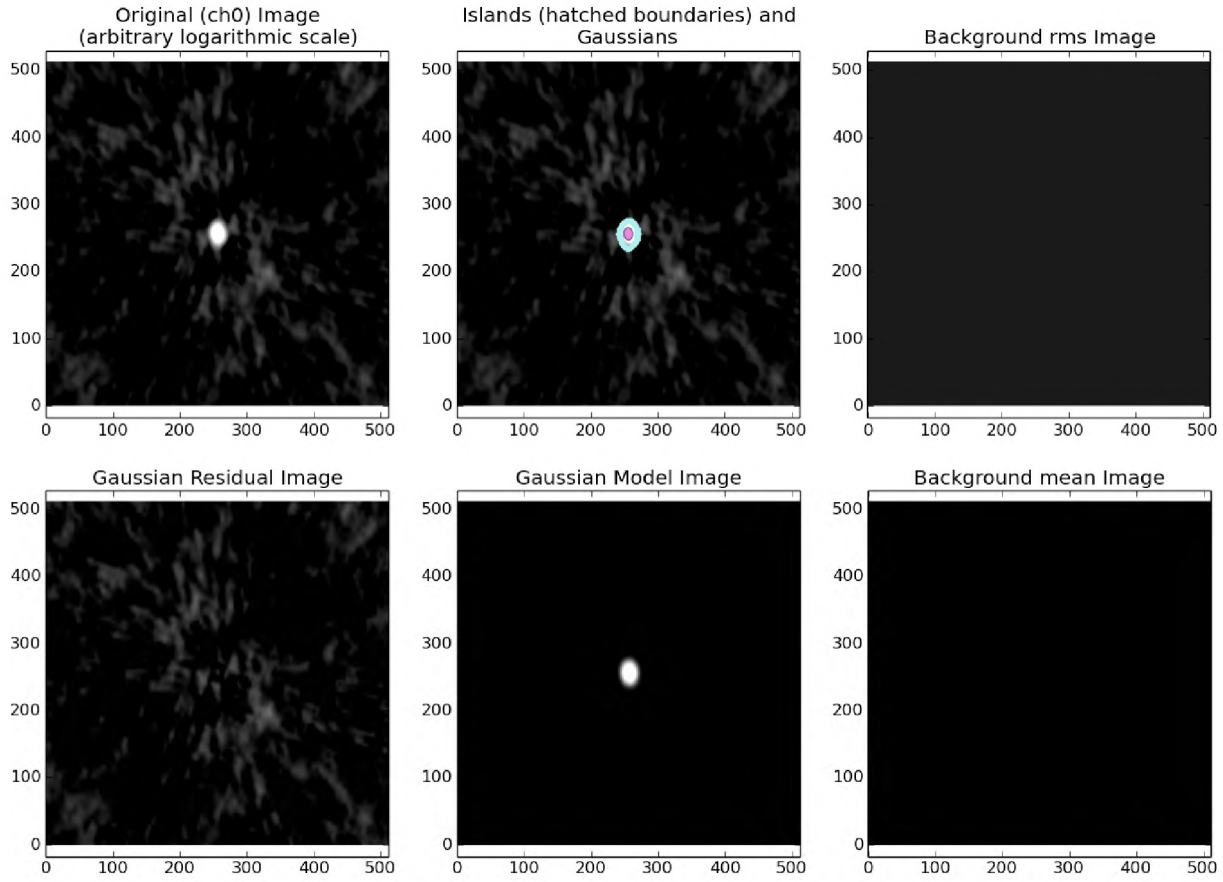

FIGURE 3.21: A snapshot of the interactive source extraction by PYBDSM, showing the original image with and without sources, the model image, background rms and mean images and the residual (original minus model) image. Boundaries of the island of the emission found by PYBDSM are indicated by light blue colour, while the fitted Gaussian for the island is shown as a purple ellipse.

The results of the calibration as well as the candidate sources detected from the CASA and WSCLEAN imaging are presented in Chapter Four.

Chapter 4

RESULTS AND DISCUSSIONS

This chapter focuses on the investigation of the known VLBI sources from Chi et al. (2013) and then comparing their positions and flux densities to this work. In the second part of this chapter, the results of the new candidate sources from this wide-field survey are presented, having processed 12 out of the total 205 sub-fields in the full survey.

4.1 Known VLBI Candidate Sources

In this section, the wide-field data was used to images of the known sources, by making on-the-fly phase rotated small (512×512 pixel) images. The known sources hereafter refers to the 12 detected sources by Chi et al. (2013). A comparison is then made between these known sources from the survey of the HDFN and HFF which has been described in Section 3.2.2.3 with the wide-field VLBI detections as a method of validation. The validation was carried out by making images centred on the positions of the known sources. The source finder PYBDSM was then used to fit single Gaussians of the sources in this work in order to compare with the Chi et al. (2013) values. For this purpose, the peak and integrated flux densities were primary-beam-corrected based on the angular distance between each source and the antenna pointing centre, assuming a Bessel function model as described in Middelberg et al. (2013) (see Section 3.2.2.5). There was no detection in the sub-field PC081. It is important to note that the source J123642+621545 (or PC081 in this work) detected by Chi et al. 2013 was classified as an 'unclear identification'.

The positions of the known sources in the GOODS-North field which were imaged in order to perform initial tests of the calibration pipeline are shown in Figure 4.1.

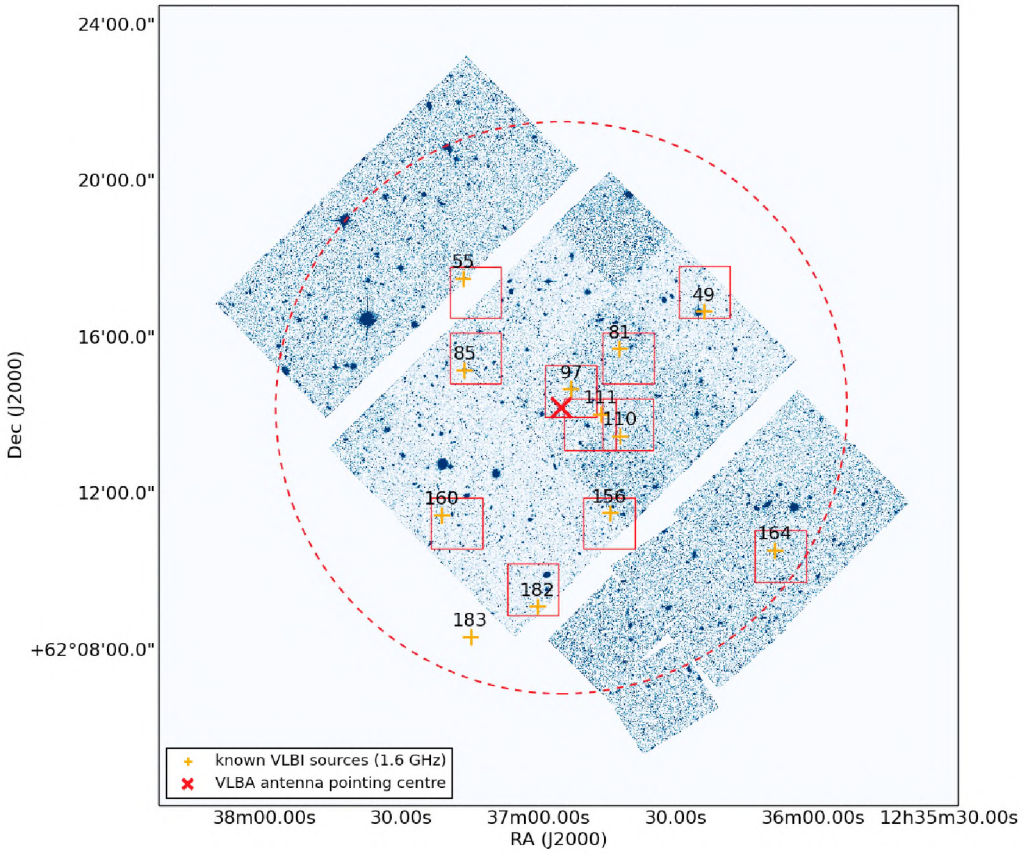

FIGURE 4.1: Plot of the HST coverage of the GOODS-North field and the positions of the Chi et al. (2013) detections: The colourscale image is a mosaic made from the HST F105W filter images from the GOODS-North field. The orange + symbol is the VLBI candidate source centroid within the phase centre (the red square symbols). The red squares are 72×72 arcsec in extent of the 64k×64k images, each with a pixel size of 1.1 mas. The big dashed circle is the VLBA 80% antenna gain while the red × symbol in the centre of the image is the antenna pointing centre. Image credit: Roger Deane.

The eleven detections from the pipeline using the CASA imaging task CLEAN are shown as Figure 4.2.

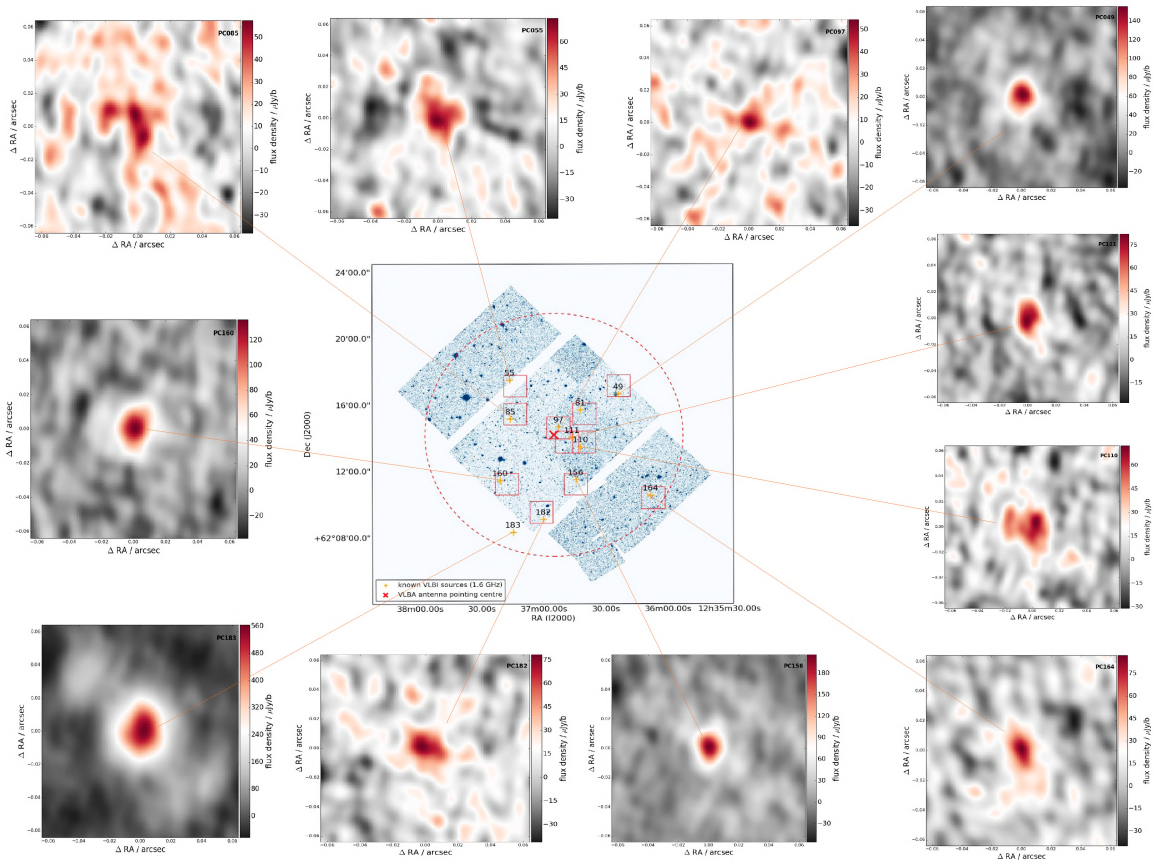

FIGURE 4.2: Automated pipeline images of the GOODS-North field made with the VLBA at 1.6 GHz- The central image is a repeat of Figure 4.1. The inserted greyscale 512×512 pixel images are the known detected sources in the validation step which were made with CASA CLEAN using the source positions of the survey by Chi et al. (2013).

As can be seen from Figure 4.2, many of the sources appear resolved and all lie well within the primary beam of the VLBA, but a future application of multi-source self-calibration (MSSC; Radcliffe et al., 2016) may lead to improved phase calibration and more compact appearance of the sources.

A comparison of the flux values obtained by Chi et al. (2013) and the survey of the GOODS-North field in this work are presented in Table 4.1. As can be seen from Table 4.1 and Figure 4.5, the flux densities of four (4) sources are consistent within uncertainties, four (4) are above with $> 1\sigma$ significance and three (3) sources are lower with $> 1\sigma$ significance. The flux values presented here are primary beam corrected.

TABLE 4.1: Comparison of flux values from previous surveys of the HDF.

Compare								
PCN	Name	RA	Dec	z	$S_{\rm VLA}$ (μJy)	$S_{\rm WSRT}$ (μJy)	$S_{\rm Chi}$ (μJy)	$S_{\rm VLBA}$ [1] (μJy)
049	J123623+621642	12:36:23.5436	62:16:42.754	1.918	481	476	327±50	335±14
055	J123716+621733	12:37:16.6811	62:17:33.327	1.146	346	362	177±25	280±13
081	J123642+621545	12:36:42.2123	62:15:45.521	0.857	150	88	343±101	
085	J123716+621512	12:37:16.3740	62:15:12.343	0.561	187	166	110±25	119±13
097	J123652+621444	12:36:52.8839	62:14:44.076	0.321	168	237	83±13	60±11
110	J123642+621331	12:36:42.0908	62:13:31.425	4.424	467	489	227±26	636±12
111	J123646+621404	12:36:46.3321	62:14:04.693	0.961	179	187	247±14	189±11
156	J123644+621133	12:36:44.3870	62:11:33.145	1.050	1290	1190	309±27	238±13
160	J123721+621129	12:37:21.2539	62:11:29.954	1.56	383	381	254±51	296±14
164	J123608+621035	12:36:08.1195	62:10:35.898	0.681	217	190	140±30	159±15
182	J123700+620909	12:37:00.2480	62:09:09.778	1.68	324	236	147±34	208±14
183	J123714+620823	12:37:14.9414	62:08:23.208	0.847	1350	1853	645±80	2565±34

[1] $S_{\rm VLBA}$ is flux density of the sources in this work.

The differences in flux values of the sources previously detected by Chi et al. (2013) and those in this work might be attributed to the fact that many compact sources are variable (most AGNs are variable at all wavelengths at which they have been observed as stated by Strotjohann et al. 2016).

In Figure 4.3, the source position comparison between Chi et al. (2013) and this work is presented.

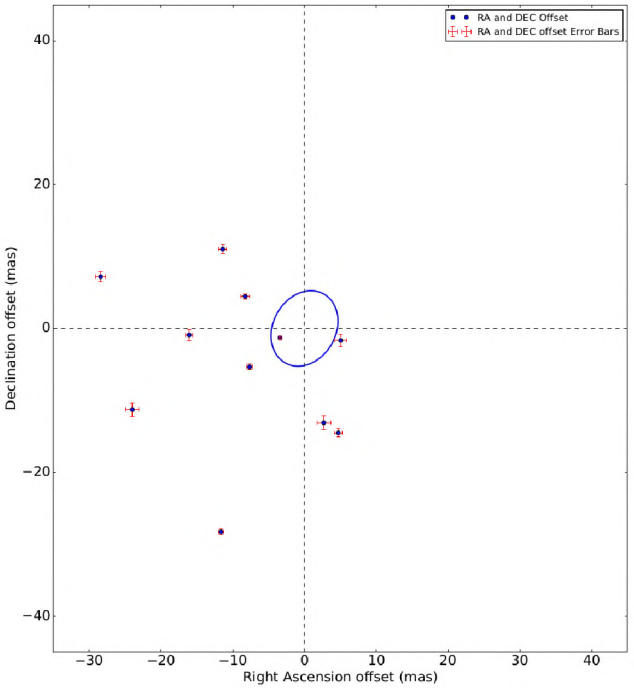

FIGURE 4.3: RA and DEC offsets between the known Chi et al. (2013) detections and this work. The positional uncertainties associated with the VLBA 1.6 GHz candidate sources are 1-σ error on the peak flux density of the candidate sources in μJy beam^{-1}. There were, however, no RA and DEC uncertainties associated with Chi et al. (2013) detections and so were calculated using Equation 4.1. The blue ellipse is a centred PSF of the VLBA which puts the offset in context. The RA and DEC offsets are within ∼30 mas. Reconciliation of the position offsets including VLBI synthetic data simulations is a topic of future work.

The RA and DEC uncertainties for the sources detected by Chi et al. (2013) were calculated using:

$$a = \frac{(0.5 \times (b/c))}{FWHM} \ , \tag{4.1}$$

where b are the integrated flux densities of the detected sources, while c are the 1-σ error on the integrated flux density of the candidate sources in sub-mJy/beam and $FWHM$ is full width at half maximum in arcsec.

noindent The positional offsets between that of Chi et al. (2013) and this work on the GOODS-North is shown in Figure 4.4.

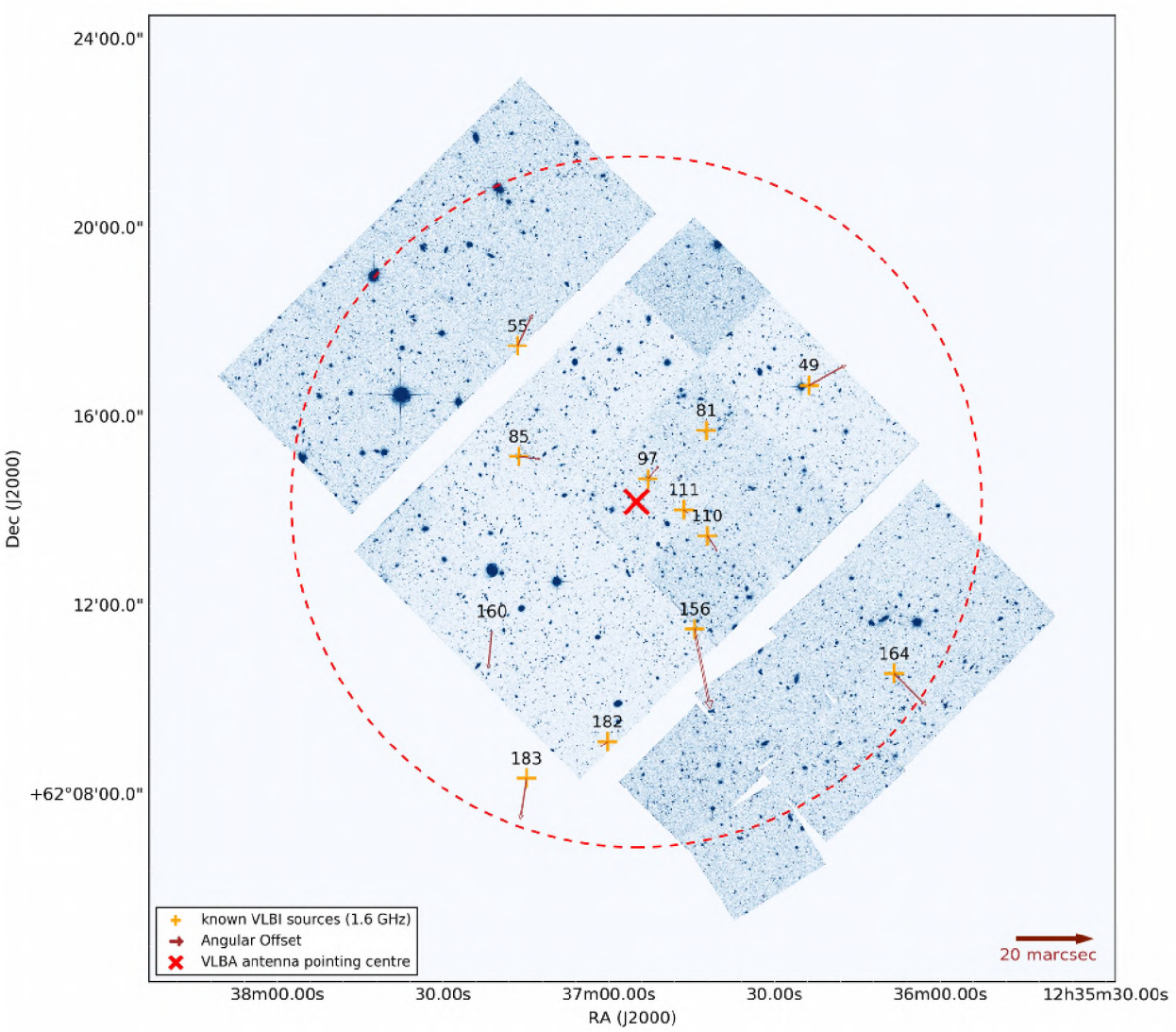

FIGURE 4.4: Positional offset between this work (VLBA observations at 1.6 GHz) and those of Chi et al. (2013) detections. The vectors show the magnitude of the positional offsets of the eleven detections. The orange + symbols indicate the source positions of Chi et al. (2013). The alphanumeric numbers represents the phase centres where the sources were detected. The colourscale image is a deep HST F814W image of the GOODS-North field. The scale bar represent the angular scale of the vectors and not that of the background.

These position offsets may be due to either calibration errors which are independent of the sources flux density (Condon, 1997) or they may be noise-like errors which are largely caused by low SNR of the source detections as discussed by Condon (1997); Condon et al. (1998) and will have to be systematically explored in future work.

Figure 4.5 shows a log-log scale plot of the integrated flux densities for the eleven known candidate sources detected in this work and that of Chi et al. (2013). The solid line is a one-to-one relation and not a straight line fit to the data points.

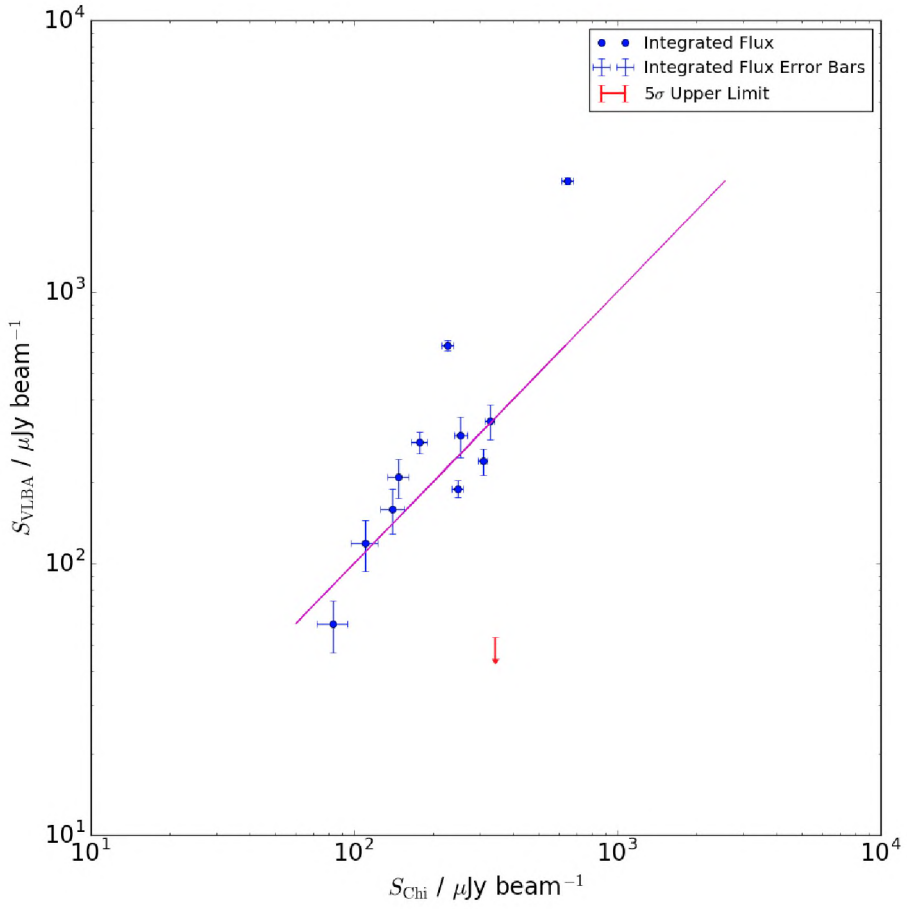

FIGURE 4.5: Flux density comparison between this work (VLBA observation at 1.6 GHz) and those obtained by Chi et al. (2013). The solid magenta line is a one-to-one plot of the flux densities while the red arrow is the 5σ upper limit of the 'missing' or undetected source (J123642+621545) in this work. Note that although the centre frequencies of the two observations differ by 200 MHz, a direct comparison was made rather than assuming a spectral index to compare them at a common frequency. This in effect assumes a flat spectrum for all sources.

There is a reasonable agreement in the flux densities and source positions given the ~ 10-year time baseline between the two surveys and the differing Fourier coverage of the VLBA and the EVN, as well as possible intrinsic source variability.

Since the results of the VLBA-detected known sources were in reasonable agreement with previous surveys, this then gave us the confidence to carry out wide-field imaging to search for previously unknown sources. In the next Section, the results of these candidate sources from the wide-field imaging techniques used are presented.

4.2 New VLBI Candidate Sources

Images of the 12 phase centres (as seen in Figure 2.1 and 4.1) we made and then run the purpose-built source finder through these images for new candidate sources which includes multi-wavelength positions. Even though there was no source detection in the subfield PC081 in this method of validation in this work, we still made wide-field images of the PC081 subfield. The candidate sources here are selected using the criteria described in 3.2.2.6.1. Emphasis is placed on the fact that the sources presented here also includes the eleven known sources shown in Figure 4.1.

All the 44 candidate sources have luminosity values above the 5σ sensitivity limit and hence are considered detections, but of course, other astrophysical processes need to be determined alongside other statistic considerations such as Likelihood ratio test (LR[1]; Sutherland & Saunders 1992; McAlpine et al. 2012, 2013).

The VLBA candidate source positions, flux densities, redshifts, angular distances and SNR of all the 44 candidate sources from the wide-field imaging using WSCLEAN are shown in Table 4.2.

[1]The likelihood ratio, LR, is the ratio of the probability that a given source and counterpart are related to the probability that they are unrelated (Sutherland & Saunders, 1992; McAlpine et al., 2012).

PCN [a]	Source Name	RA	DEC	$S_{1.6GHz}$ [c] (μJy/beam)	$I_{1.6GHz}$ [b] (μJy)	z	$L_{1.6}$ [d] (W Hz^{-1})	SNR	θ [e] (arcsec)	$T_{\rm B}$ [f] K
049	VLBA J123625+621701	12:36:25.894	+62:17:01.720	66±15	186±20	1.05	9.42e+23	5.67	0.36	3.13E+06
049	VLBA J123625+621717	12:36:25.000	+62:17:17.300	69±10	594±11	1.51	4.49e+24	5.6	0.42	3.97E+06
049	VLBA J123623+621642	12:36:23.554	+62:16:42.750	116±12	1071±13		0.0	11.16	0.11	2.64E+06
049	VLBA J123620+621701	12:36:20.882	+62:17:01.680	78±17	276±21	1.73	2.19e+24	5.96	0.29	4.90E+06
055	VLBA J123716+621733	12:37:16.684	+62:17:33.320	57±9	626±10	1.15	3.59e+24	6.73	0.08	2.83E+06
055	VLBA J123715+621647	12:37:15.228	+62:16:47.070	66±13	147±18	0.61	2.62e+23	5.72	0.26	2.45E+06
055	VLBA J123714+621648	12:37:14.793	+62:16:48.480	63±11	205±14	0.51	2.48e+23	5.61	0.4	2.18E+06
055	VLBA J123712+621649	12:37:12.019	+62:16:49.170	67±12	239±15	1.21	1.47e+24	6.04	0.15	3.41E+06
055	VLBA J123710+621646	12:37:10.049	+62:16:46.680	67±12	225±16	0.09	5.68e+21	5.52	0.33	1.67E+06
055	VLBA J123709+621641	12:37:09.235	+62:16:41.610	103±21	491±25	1.69	3.87e+24	5.68	0.01	6.31E+06
085	VLBA J123716+621545	12:37:16.207	+62:15:45.450	63±12	197±16	1.22	1.22e+24	5.6	0.28	3.22E+06
085	VLBA J123709+621524	12:37:09.941	+62:15:24.040	23±4	1481±27		0.0	5.62	0.44	5.35E+05
097	VLBA J123657+621415	12:36:57.417	+62:14:15.500	39±3	902±4	2.89	3.57e+24	5.53	0.25	3.47E+06
097	VLBA J123651+621459	12:36:51.317	+62:14:59.490	56±7	488±8	4.46	1.8e+23	5.55	0.02	7.04E+06
097	VLBA J123648+621416	12:36:48.825	+62:14:16.210	66±14	289±17	0.65	5.86e+23	5.75	0.46	2.49E+06
097	VLBA J123648+621436	12:36:48.275	+62:14:36.330	76±17	190±23	1.95	1.47e+24	5.59	0.09	5.15E+06
110	VLBA J123642+621331	12:36:42.102	+62:13:31.410	40±4	846±4	4.42	3.35e+23	7.22	0.1	5.01E+06
111	VLBA J123650+621357	12:36:50.829	+62:13:57.440	42±6	437±7	0.8	1.38e+24	5.77	0.34	1.73E+06
111	VLBA J123646+621404	12:36:46.338	+62:14:04.670	66±6	597±7	0.96	2.61e+24	8.65	0.06	2.96E+06

111	VLBA J123645+621409	12:36:45.440	+62:14:09.910	58±8	339±10	0.73	8.77e+23	5.5	0.24	2.32E+06
156	VLBA J123646+621055	12:36:46.484	+62:10:55.060	46±6	384±6	1.46	2.84e+24	5.63	0.29	2.61E+06
156	VLBA J123644+621047	12:36:44.567	+62:10:47.080	54±7	654±8	1.4	4.68e+24	5.55	0.46	3.00E+06
156	VLBA J123644+621133	12:36:44.393	+62:11:33.160	145±10	1094±11	1.01	5.21e+24	18.08	0.03	6.66E+06
156	VLBA J123644+621136	12:36:44.320	+62:11:36.220	47±7	339±8	1.74	2.69e+24	5.63	0.18	2.97E+06
160	VLBA J123721+621105	12:37:21.497	+62:11:05.110	69±13	184±18	1.7	1.46e+24	5.52	0.04	4.31E+06
160	VLBA J123721+621129	12:37:21.261	+62:11:29.960	103±7	993±7	1.87	7.8e+24	11.61	0.08	6.74E+06
160	VLBA J123717+621109	12:37:17.106	+62:11:09.970	65±14	147±20	1.19	8.85e+23	5.59	0.33	3.27E+06
160	VLBA J123715+621057	12:37:15.629	+62:10:57.400	67±15	203±19	0.86	7.36e+23	5.55	0.25	2.86E+06
160	VLBA J123714+621149	12:37:14.986	+62:11:49.140	80±13	553±15	0.86	1.98e+24	5.79	0.35	3.42E+06
164	VLBA J123608+621035	12:36:08.111	+62:10:35.900	61±9	605±10	0.68	1.36e+24	5.94	0.11	2.34E+06
164	VLBA J123607+621007	12:36:07.450	+62:10:07.770	41±3	759±3	0.64	1.49e+24	5.68	0.26	1.54E+06
164	VLBA J123606+621017	12:36:06.136	+62:10:17.030	55±11	470±12	1.12	2.61e+24	5.73	0.45	2.68E+06
182	VLBA J123702+620905	12:37:02.966	+62:09:05.560	58±10	519±12	1.74	4.11e+24	5.78	0.31	3.67E+06
182	VLBA J123701+620950	12:37:01.591	+62:09:50.320	52±7	629±7	1.02	3.02e+24	6.08	0.4	2.41E+06
182	VLBA J123700+620909	12:37:00.248	+62:09:09.780	54±8	603±9	1.61	4.71e+24	6.29	0.1	3.22E+06
182	VLBA J123659+620918	12:36:59.828	+62:09:18.810	45±7	525±7	0.2	7.6e+22	5.74	0.31	1.24E+06
182	VLBA J123658+621007	12:36:58.723	+62:10:07.090	86±16	290±20	1.4	2.08e+24	5.54	0.38	4.75E+06
182	VLBA J123658+620926	12:36:58.128	+62:09:26.910	72±15	192±21	1.93	1.5e+24	5.63	0.42	4.80E+06
182	VLBA J123656+620929	12:36:56.959	+62:09:29.860	78±17	302±21	1.67	2.38e+24	5.57	0.18	4.78E+06
183	VLBA J123713+620922	12:37:13.413	+62:09:22.930	49±8	416±8	1.43	3.04e+24	5.76	0.45	2.74E+06
183	VLBA J123712+620946	12:37:12.085	+62:09:46.240	58±10	401±11	5.11	4.12e+22	5.99	0.18	8.16E+06
183	VLBA J123711+620918	12:37:11.285	+62:09:18.120	70±14	270±17	1.24	1.72e+24	5.54	0.19	3.62E+06

183	VLBA J123710+620935	12:37:10.798	+62:09:35.240	23±5	1891±43	1.42	1.37e+25	5.66	0.26	1.28E+06
183	VLBA J123708+620925	12:37:08.310	+62:09:25.630	89±15	403±18			5.52	0.32	2.05E+06

TABLE 4.2: VLBI Detections in the eleven sub-fields

[a] PCN is phase centre number or field number.

[b] $S_{1.6GHz}$ is the primary beam corrected peak flux of the sources. The uncertainties associated with the fitted Gaussians in PyBDSM are computed using 1-σ error on the peak flux density of the candidate sources in μJy beam^{-1}.

[c] $I_{1.6GHz}$ is the primary beam corrected integrated flux of the candidate sources. Uncertainties quoted here are directly from the images on which Gaussian smoothing has been performed. The uncertainties associated with the integrated flux densities are determined by calculating 1-σ error on the total flux density of the candidate sources in μJy. Thus for a source composed of n-Gaussians with uncertainties in flux densities of $\delta_1, \delta_2, \delta_3, ..., \delta_n$, the uncertainty in the integrated flux δ_{int} is given by $\delta_{int} = \sqrt{\delta_1 + \delta_2 + \delta_3 + ... + \delta_n}$.

[d] $L_{1.6}$ is the continuum Luminosity calculated using Equation 1.4. We assumed a 3D-HST redshift of z, and a flat Λ cold dark matter (ΛCDM) with cosmological parameters; Hubble constant at z=0 of $H_0 = 70$ km^{-1}s^{-1}Mpc^{-1}, Omega matter of $\Omega_0 = 0.3$.

[e] Angular separation (θ) is the distance between the detected source positions and the nearest multi-wavelength candidate source.

[f] $T_{\rm B}$ is peak brightness temperature estimated using Equation 1.8.

All the known sources detected in the eleven (11) phase centres are presented in Figure 4.6a through to Figure 4.16e. The source positions of the 3D-*HST* sources are indicated with green + symbols, those of the X-ray positions are denoted with red × symbols. The contours plotted indicate the total radio intensity of 0.05 mJy/beam, 0.1 mJy/beam, 0.2 mJy/beam, 0.4 mJy/beam, 8.0 mJy/beam, 1.6 mJy/beam of the GOODS-North 1.4 GHz VLA map while that of the NIR are represented by a square blue box symbols in the greyscale images below. A brief description of the multi-wavelength catalogue from which the data shown in the VLBI candidate images were taken from is given in Appendix A.

The candidate sources are shown as the inserted zoomed-in images on the bottom right corner of each image (e.g., Figure 4.6a). The candidate sources are presented in Section 4.2.1 through to Section 4.2.11.

4.2.1 VLBI Candidate Sources in Phase Centre PC049

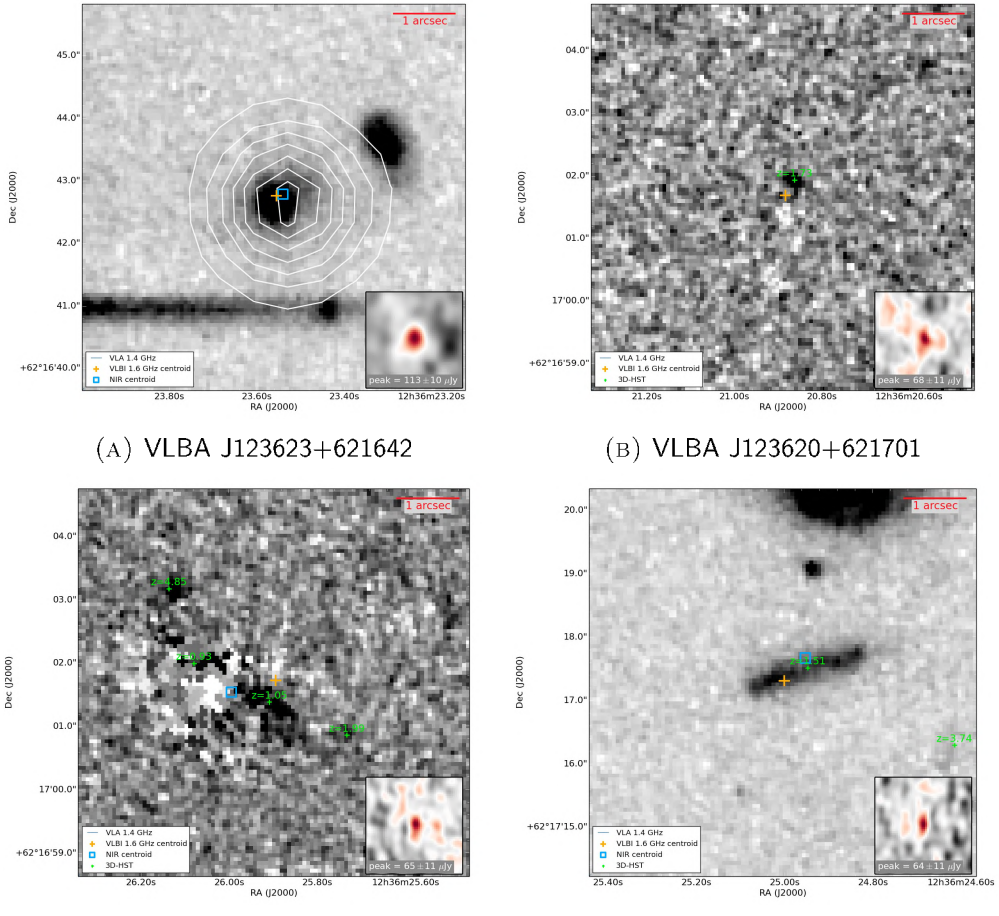

(A) VLBA J123623+621642

(B) VLBA J123620+621701

(C) VLBA J123625+621701

(D) VLBA J123625+621717

FIGURE 4.6: Candidate sources in the subfield PC049.

4.2.2 VLBI Candidate Sources in Phase Centre PC055

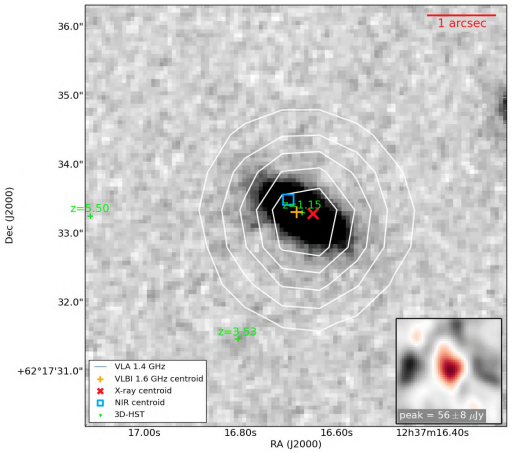

(A) VLBA J123716+621733

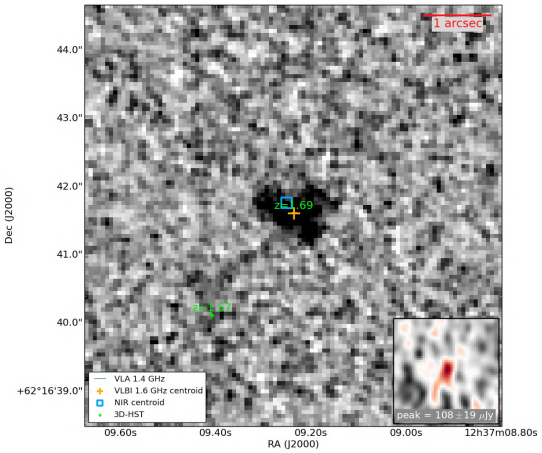

(B) VLBA J123709+621641

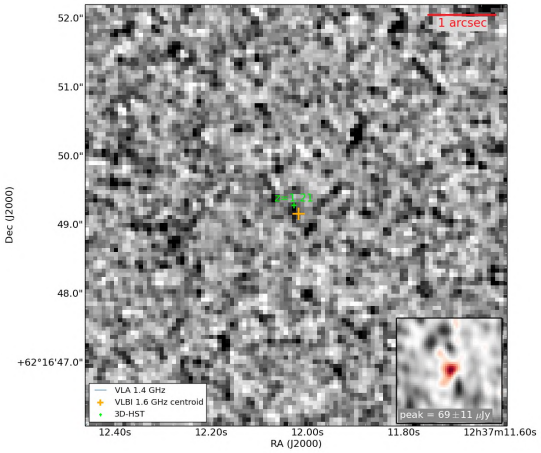

(C) VLBA J123712+621649

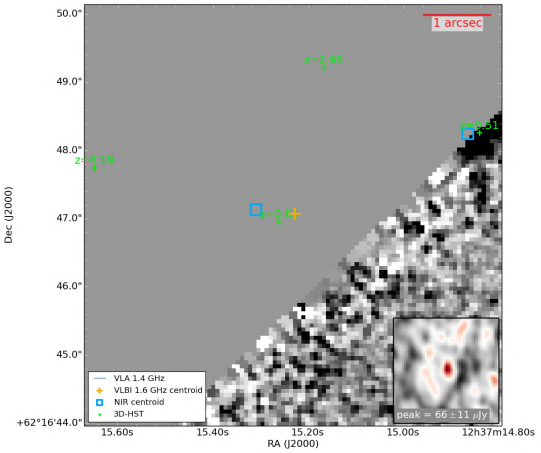

(D) VLBA J123715+621647

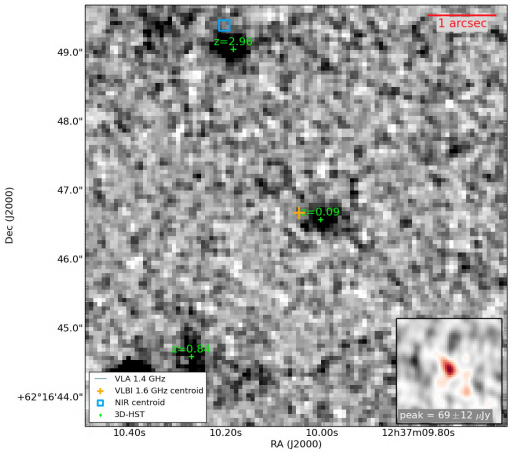

(E) VLBA J123710+621646

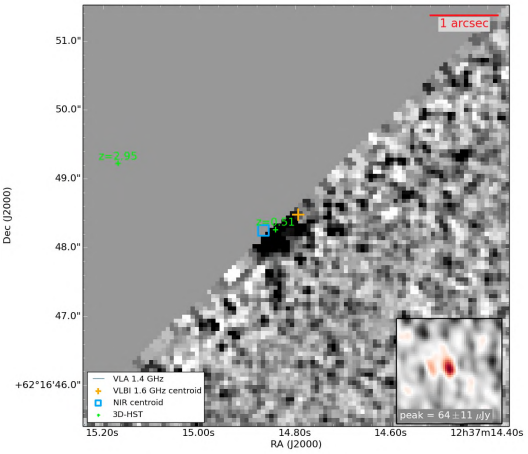

(F) VLBA J123714+621648

FIGURE 4.7: Candidate sources in the subfield PC055.

4.2.3 VLBI Candidate Sources in Phase Centre PC085

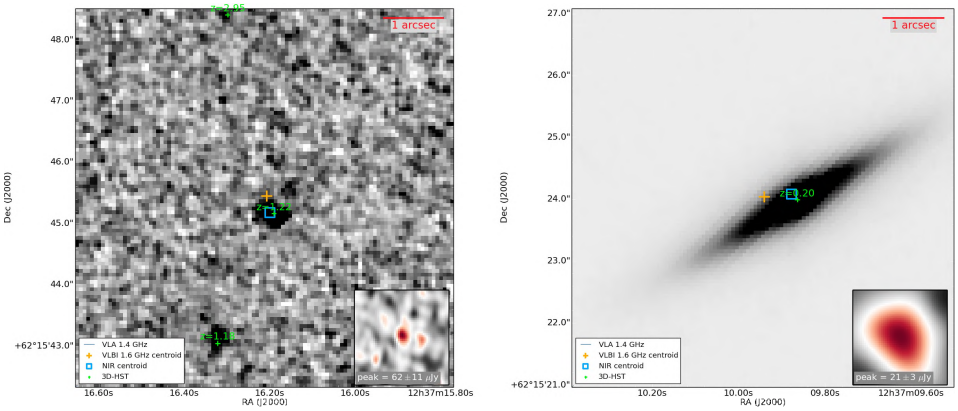

(A) VLBA J123716+621545 (B) VLBA J123709+621524

FIGURE 4.8: Candidate sources in the subfield PC085.

4.2.4 VLBI Candidate Sources in Phase Centre PC097

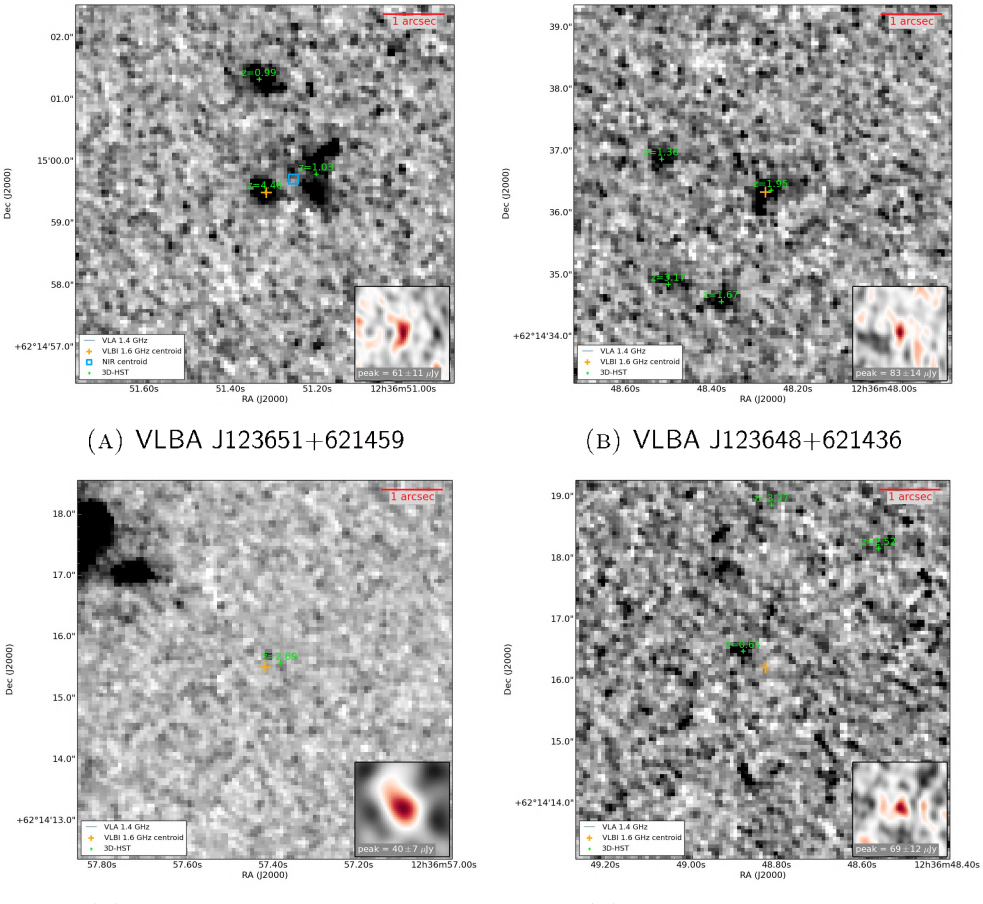

(A) VLBA J123651+621459 (B) VLBA J123648+621436

(C) VLBA J123657+621415 (D) VLBA J123648+621416

FIGURE 4.9: Candidate sources in phase centre PC097

4.2.5 VLBI Candidate Sources in Phase Centre PC110

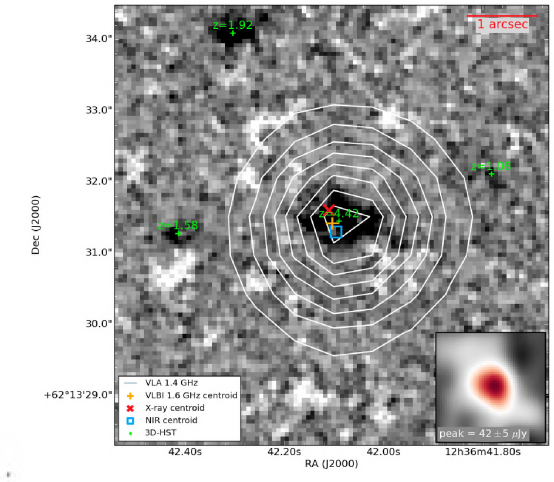

FIGURE 4.10: Candidate sources in the subfield PC110.

4.2.6 VLBI Candidate Sources in Phase Centre PC111

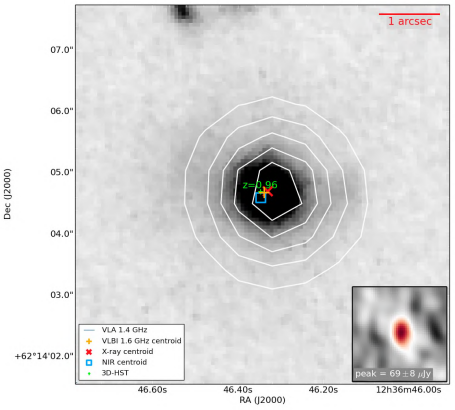

(A) VLBA J123646+621404

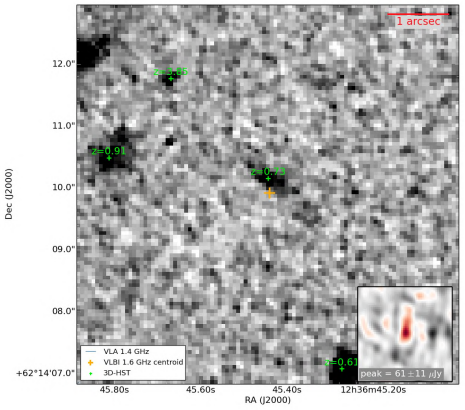

(B) VLBA J123645+621409

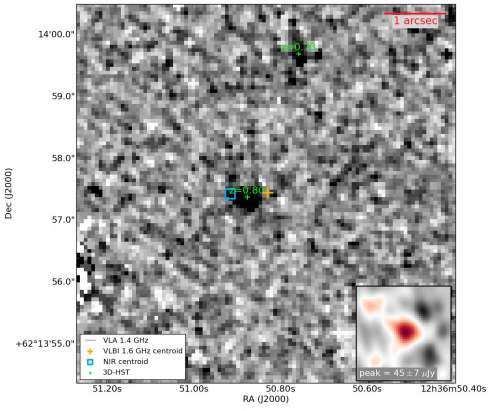

(C) VLBA J123650+621357

FIGURE 4.11: Candidate sources in subfield PC111.

4.2.7 VLBI Candidate Sources in Phase Centre PC156

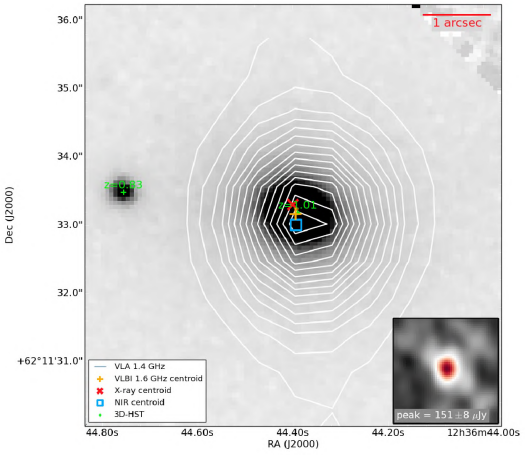

(A) VLBA J123644+621133

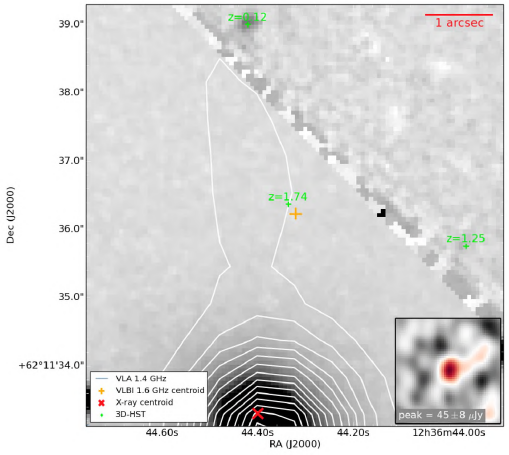

(B) VLBA J123646+621055

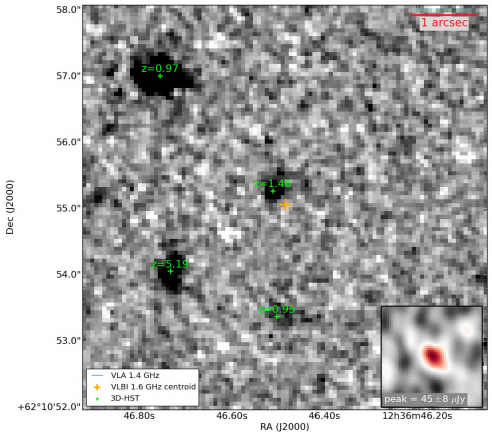

(C) VLBA J123644+621136

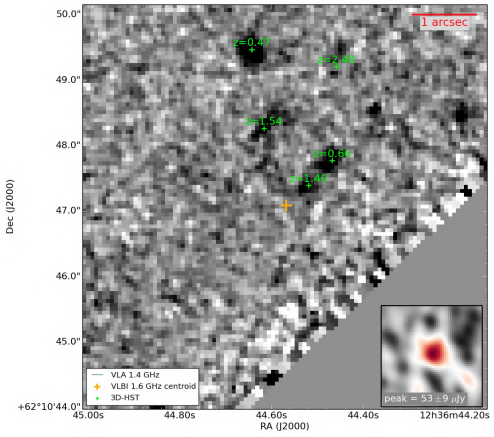

(D) VLBA J123644+621047

FIGURE 4.12: Candidate sources in phase centre PC156.

4.2.8 VLBI Candidate Sources in Phase Centre PC160

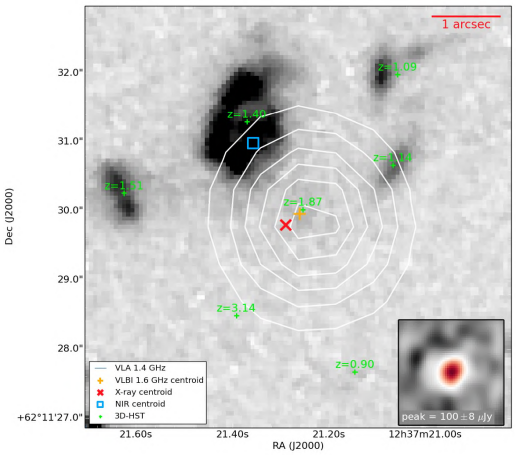

(A) VLBA J123721+621129

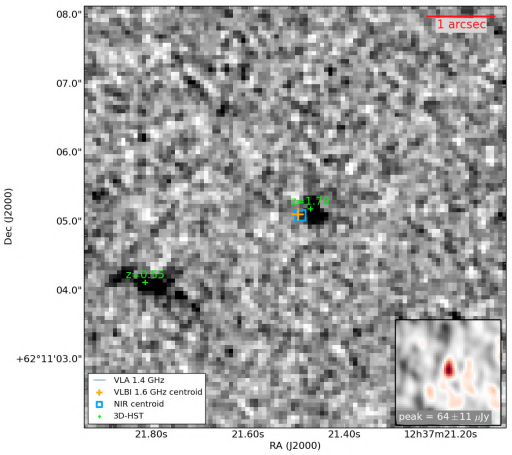

(B) VLBA J123721+621105

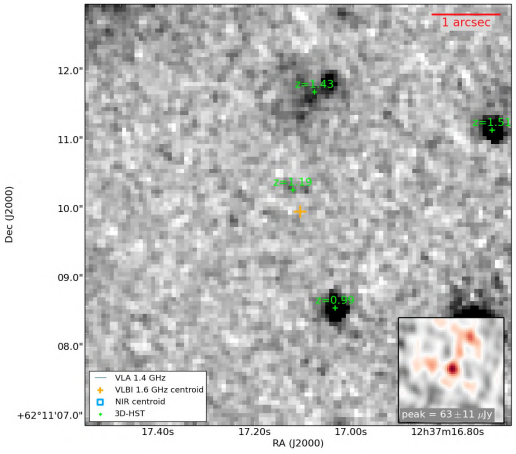

(C) VLBA J123717+621109

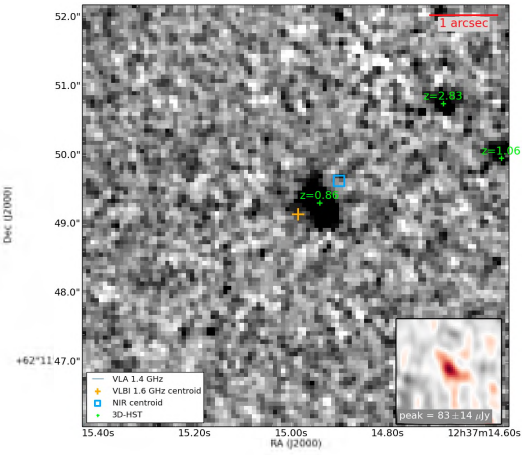

(D) VLBA J123714+621149

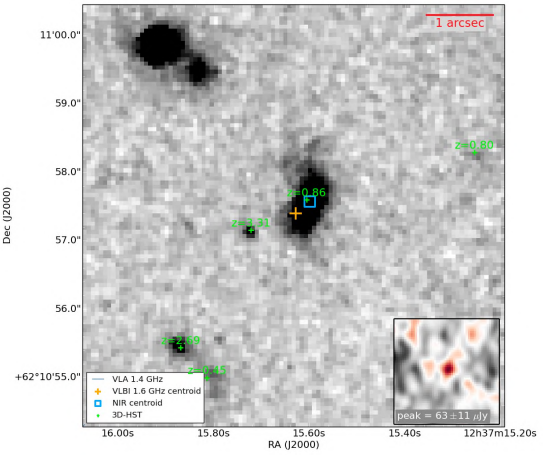

(E) VLBA J123715+621057

FIGURE 4.13: Candidate sources in the subfield PC160.

4.2.9 VLBI Candidate Sources in Phase Centre PC164

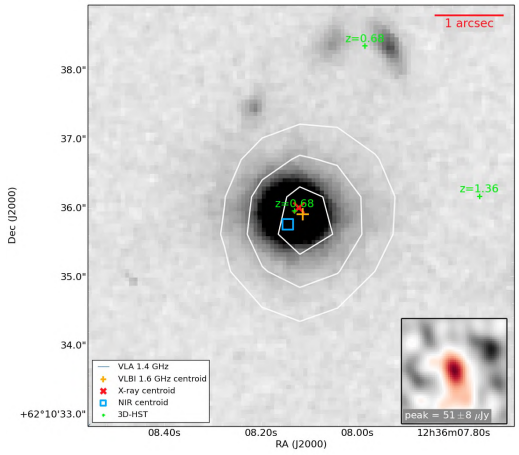

(A) VLBA J123608+621035

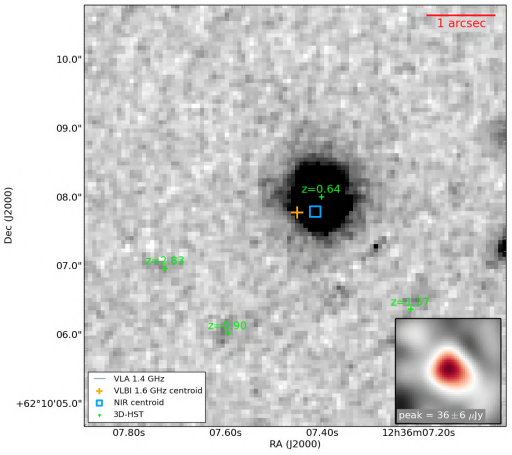

(B) VLBA J123607+621007

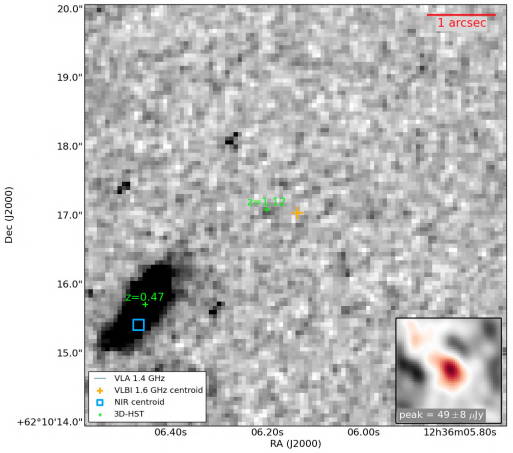

(C) VLBA J123606+621017

FIGURE 4.14: Candidate sources in the subfield PC164

4.2.10 VLBI Candidate Sources in Phase Centre PC182

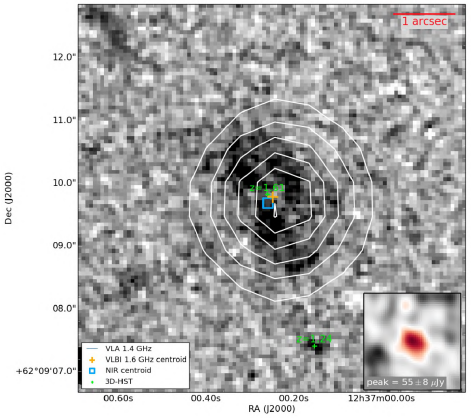

(A) VLBA J123700+620909

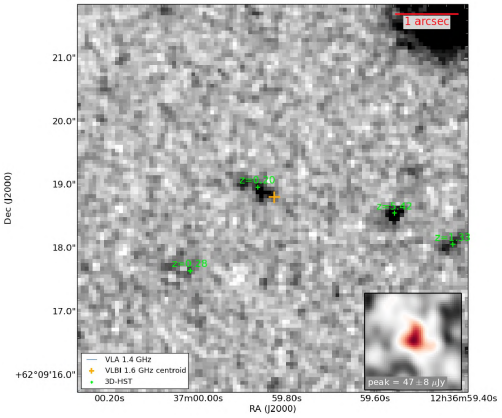

(B) VLBA J123659+620918

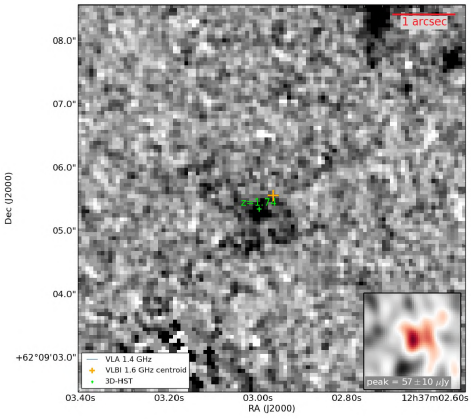

(C) VLBA J123702+620905

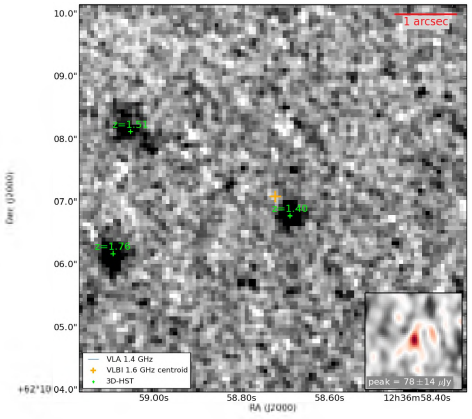

(D) VLBA J123658+621007

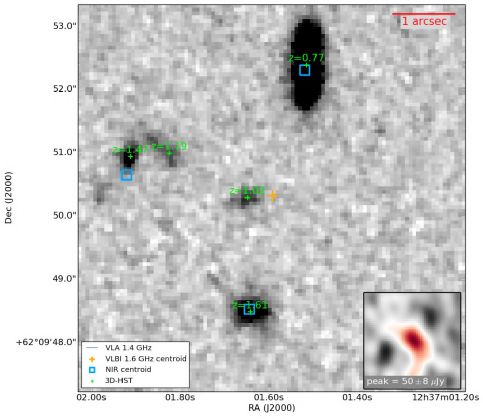

(E) VLBA J123701+620950

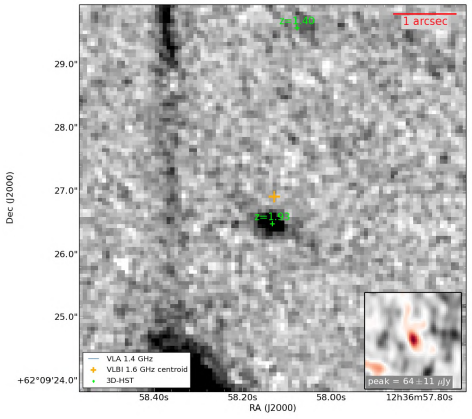

(F) VLBA J123658+620926

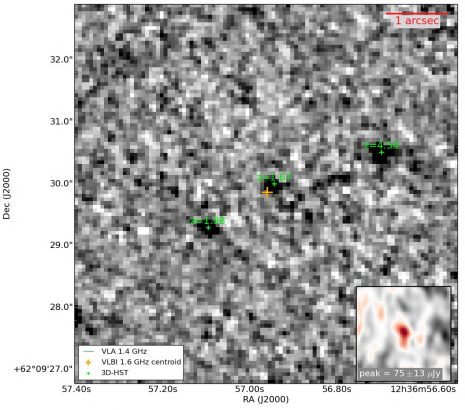

(G) VLBA J123656+620929

FIGURE 4.15: Candidate sources in the subfield PC182.

4.2.11 VLBI Candidate Sources in Phase Centre PC183

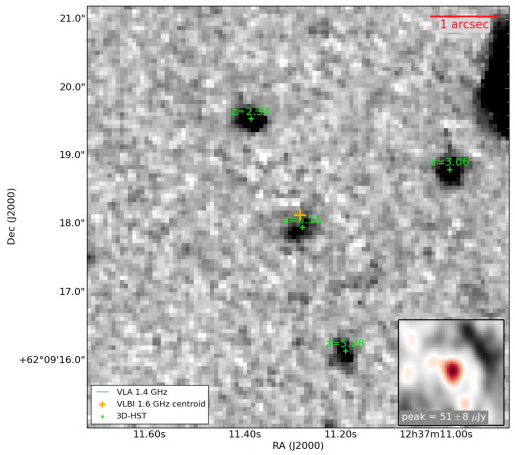

(A) VLBA J123711+620918

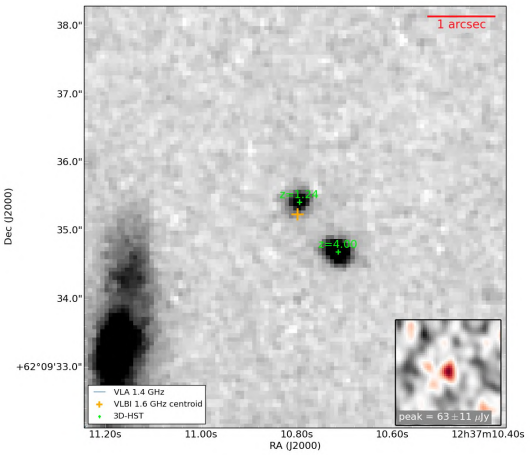

(B) VLBA J123710+620935

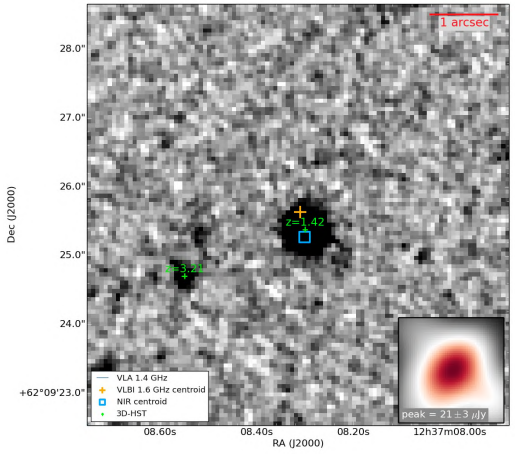

(C) VLBA J123708+620925

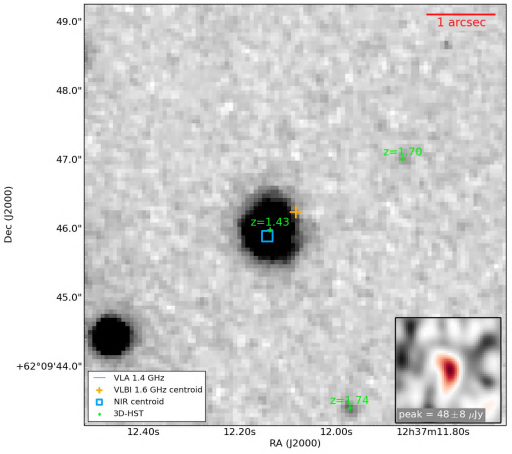

(D) VLBA J123712+620946

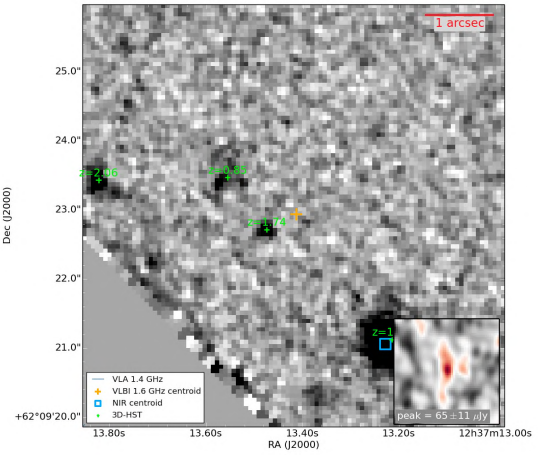

(E) VLBA J123713+620922

FIGURE 4.16: Candidate sources in the subfield PC183.

In total there are 44 candidate sources in the 12 processed sub-fields, each with a sky area of $\sim$70.4 arcsec^2. The flux density uncertainty of the candidate sources is $\sim$3 - 43 μJy/beam. The rms uncertainties of the flux densities are fitted rather than local. This is because three iterations of smoothing were carried out on the images before carrying out source extraction and so this might have an effect on the rms values.

A summary of the cross-matched multi-wavelength sources from the wide-field imaging is given as Figure 4.17. The summary results assume all sources are real, which is unlikely to be true, caution is thus raised in over-interpreting the veracity of all these candidate sources. In Section 4.3, further discussion on some of the statistical considerations that need to be understood will be mentioned. The goal here is simply to perform initial tests of this wide-field imaging technique and the purpose-built source finder.

A summary of the candidate sources in shown in Figure 4.17.

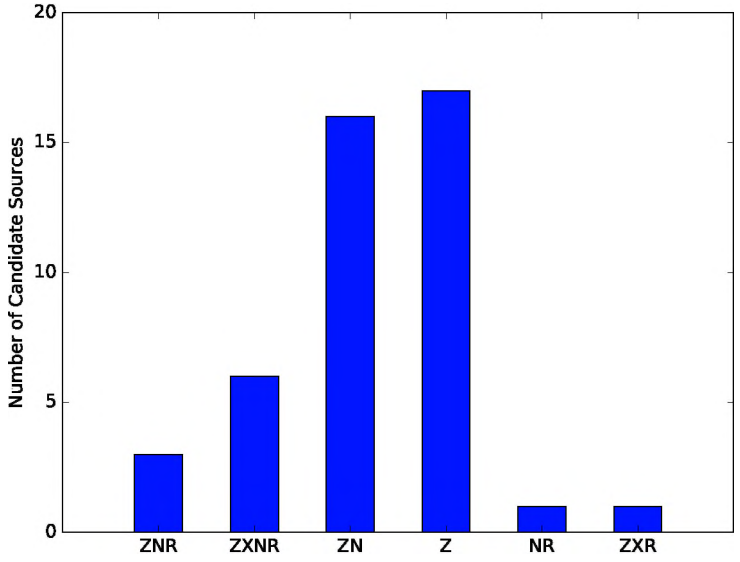

FIGURE 4.17: Summary of the candidate sources: ZN is the number of candidate sources with both optical counterparts and NIR counterparts; ZXNR represents the number of candidate sources which has optical counterparts, X-ray counterparts, NIR counterparts and VLA counterparts; ZNR are VLBI candidate sources with photometric redshifts and has NIR and Radio counterparts; NR represents the number of candidate sources with only NIR and radio counterparts , ZXR are the candidate sources with optical counterpartss, X-ray and VLA radio counterparts and Z represents the number of candidate sources with only optical counterparts.

Classification of these candidate sources are beyond the scope of this thesis. As stated earlier, 11 out of the 44 candidate sources have been detected in previous VLBI surveys (i.e., Chi et al. 2013) while the rest of the 33 sources are new candidate sources detected in this work. The 6 VLBI candidate sources labelled ZXNR (Figures 4.7a, 4.10, 4.11a, 4.12a, 4.13a and 4.14a), NR (Figure 4.6a), two of ZN (Figures 4.16c, 4.8a), one of ZNR (Figure 4.15a) and

one of Z (Figure 4.9b) in Figure 4.17 are all previously known detections from corresponding positions of the multi-wavelength counterpart of every source.

In Figure 4.18 we present the VLBI SNR as a function of angular separation from the corresponding position of the multi-wavelength counterpart of every source.

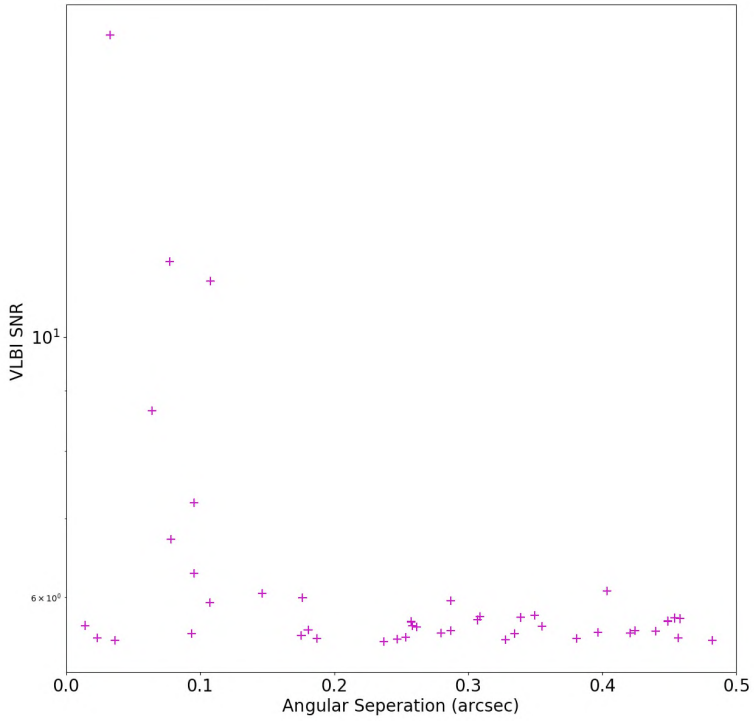

FIGURE 4.18: A plot of VLBI SNR and angular separation of all the 44 VLBI candidate sources from the eleven phase centres (sub-fields). The angular separation is the angular distance between the candidate source positions and their nearest multi-wavelength counterpart. Given the cross-matching area increasing as the square of angular separation, if these candidate detections were all spurious, one would expect a dramatic increase in the total number towards angular separations of 0.5 arcsec, which is not observed (see Figure 4.19).

Thirty-nine (39) of the candidate sources have a SNR between $5.5 \leqslant SNR < 7$, whereas 5 of the candidate sources were detected at a SNR $\geqslant 7$ with corresponding angular separation of $\leqslant 0.11$ arcsec.

The likelihood that theses VLBI candidate sources are spurious would be seen if most were detected towards the angular separation of 0.5 arcsec. Five sources were detected at angular separation of 0.26 arcsec as seen in Figure 4.19:

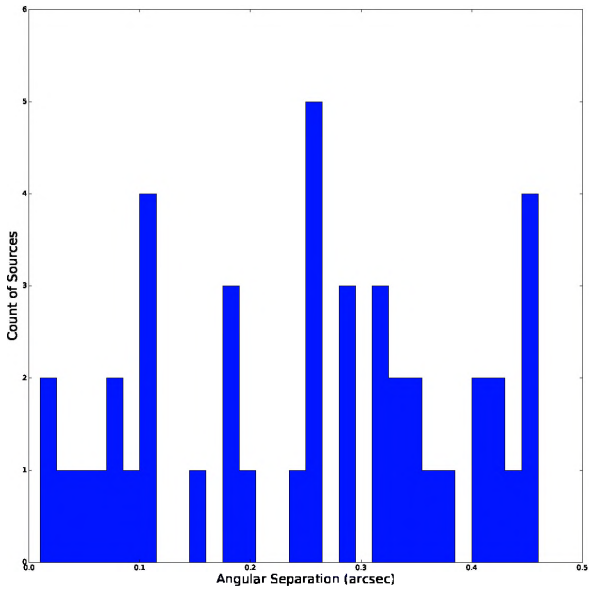

FIGURE 4.19: Histogram of the angular separation of the VLBI candidate sources from their multi-wavelength counterparts.

In Figure 4.20, plot of the luminosity of the candidate sources as function of redshift is presented.

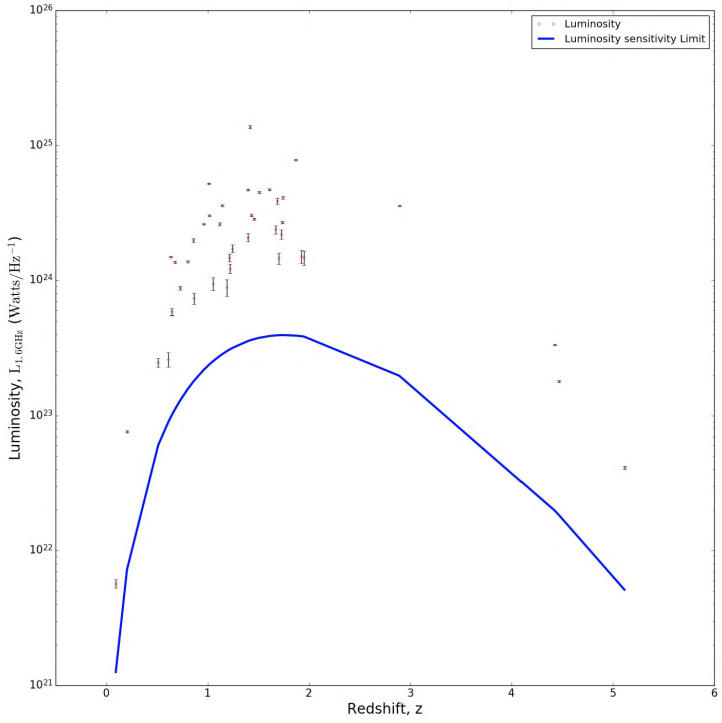

FIGURE 4.20: A plot of radio luminosity against redshift. The radio luminosity values are calculated by inserting the flux density, redshift and an assumed spectral index of $\alpha = -0.7$ into Equation 1.4. The luminosity sensitivity limit was calculated using a 5σ detection limit.

The strong correlation between radio luminosity and morphology type of radio galaxies is

essential for observational cosmology as stated by (Fanaroff & Riley, 1974). Secondly, because of the redshift-luminosity correlation, any effect directly related to redshift could also be regarded as a luminosity-dependent effect and vice-versa (Baum et al., 1995). The luminosity values in this survey can, thus, be used to estimate the type of morphologies (eg., star forming galaxies, AGN, supernovae) of the VLBI candidate sources. An inspection of Figure 4.20 reveals that all the VLBI candidate sources are above the luminosity sensitivity limit of the VLBA in this survey.

The linear relationship between the star formation rate (SFR) and luminosity is presented as:

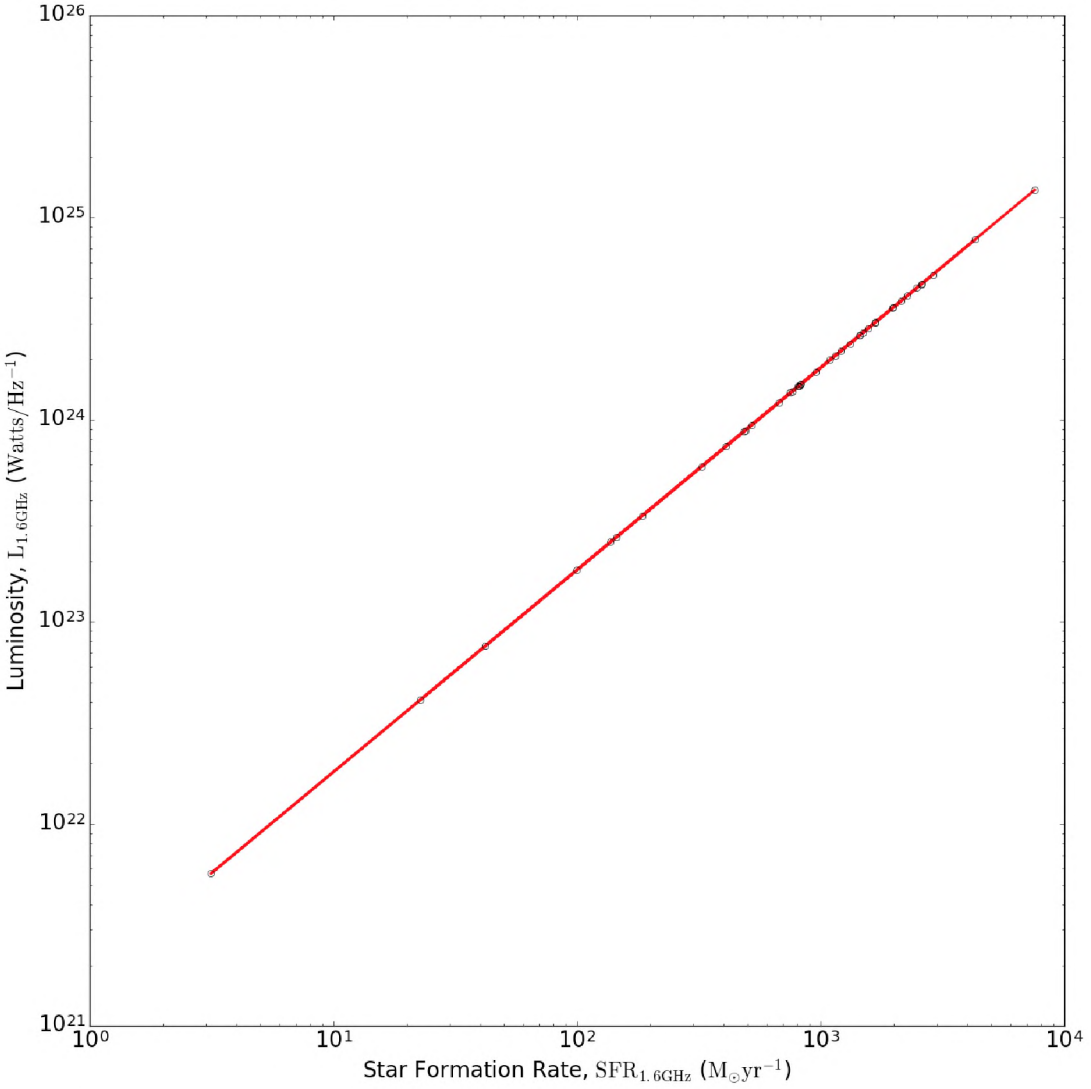

FIGURE 4.21: A plot of linear relationship between the radio luminosity of the VLBI candidate sources and the SFR.

Here, it is incorrectly assumed that most of the candidate sources are AGN and there is a direct relationship between the local radio luminosities derived and the SFR (Condon, 1992; Bell, 2003). In Figure 4.21, it has been shown that there is a linear relationship between

luminosity and star formation as theoretically expected (Bell, 2003). The reason for the assumption is to bolster the assertion that most of these candidate sources are indeed AGN.

The investigation of the relationship between the 1.6 GHz luminosity and the SFR rate over a broad luminosity and redshift range from this work can be used for future exploitation of surveys from the SKA and its precursors to measure the cosmic star formation history and to provide reliable predictions for future deep radio surveys (Bonato et al., 2017). The preceding assertion is only true after classification of the sources and therefore by studying only the relation on star-formating galaxies.

From the literature, it has been demonstrated that a VLBI detection with brightness temperature exceeding 10^5 K is interpreted as being a strong indicator of non-thermal synchrotron emissions, and this can unambiguously be used as an AGN indicator, as stated by Condon (1992); Kewley et al. (2000); Cao et al. (2014). The brightness temperature (see Table 4.2) of a large sample of the candidate sources in this work are $> 10^6$ K and so are likely to be considered as AGN. This assertion is only true after classification of these candidate sources. Hence, astrophysical parameters such as optical depth, morphology and spectral index would be considered for the classification.

Next, a brief description of the statistical analysis that would be performed on the detected sources is given.

4.3 Statistical Considerations

Each 64k×64k pixel map has a total of 4.3 Giga pixels, and so the typically used 5σ threshold is not good enough as this will produce ~ 1231 false positive using the relation

$$FP = \frac{1}{2}\left(1 - erf\left(\frac{x}{\sqrt{2}}\right)\right), \tag{4.2}$$

where erf is the error function, FP is the calculated number of false positive (FP) sources and x is an observation from normally distributed random variable.

Without the additional multi-wavelength criteria, about 13,541 false detections for all the eleven 64k×64k images would have been detected by the purpose-built source finder. In view of this, false positive rate based on NIR, X-ray, and source density of the candidate sources would be calculated and added to the purpose-built source finder. The calculated source densities for the *Spitzer*, X-ray, *HST*-3D and the VLA sources per sq. arcmin are respectively 73.1, 1.8, 214.0 and 1.9.

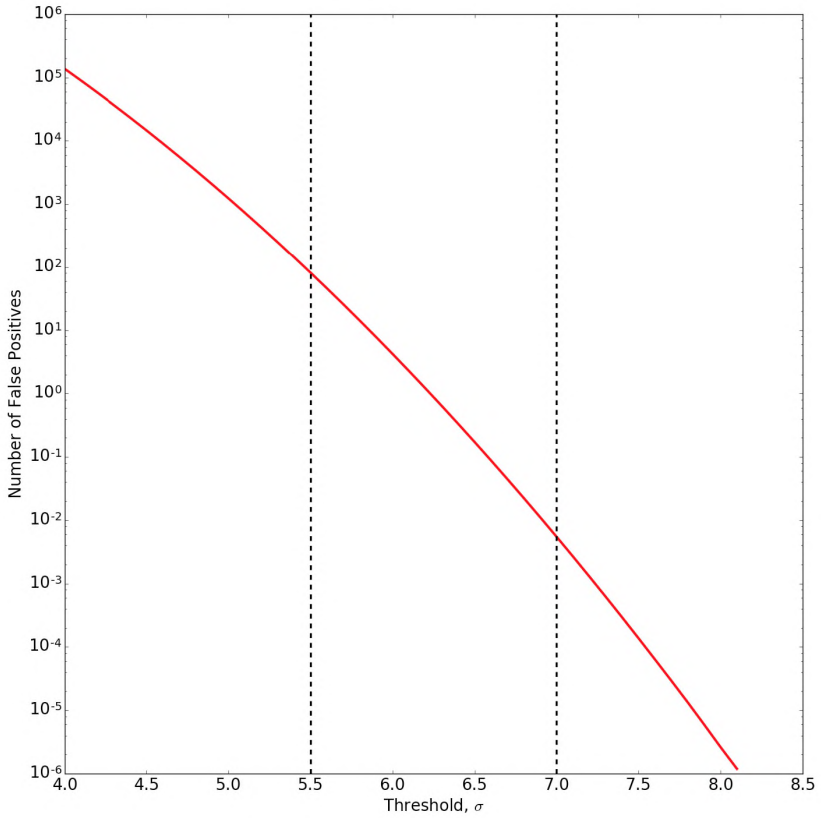

FIGURE 4.22: Number of false positives as a function of detection threshold without the multi-wavelength criteria. Sources with threshold $<5.5\sigma$ were not considered as the maximum number of false positives that would be produced are $>10^5$ considering the number of pixels per the 64k×64k image. Using a threshold between 5.5σ and 7σ would result in a maximum of ∼82 false positives without the multi-wavelength criteria. This, of course, is under the assumption of pure Gaussian noise.

Figure 4.22 shows that the number of false positives decreases as the detection threshold (SNR) increases. Given the relatively small number of false positive (0.01) sources per the 64k×64k pixel image at a threshold of 7σ, all detections with SNR $\geqslant 7$ are considered real, since this SNR is high enough to neglect the false positive rate and therefore additional multi-wavelength criteria were not considered for such sources. The 5.5σ and 7σ thresholds clearly need to be optimise, but this is the subject of future works.

The number of false positive sources at thresholds of less than 5σ are too high (729.82), whereas for threshold of 7σ is almost null (0.001) but some real detections would be missed. Hence, only sources with threshold of 5.5 (82 false positives) and 7 were considered, together with a multi-wavelength criterion to constrain and lower the number of false positives. The added criteria of course does not mean the 33 candidates are true sources. Detailed statistical considerations will thus be carried out to investigate the number of false positives in this sample space. These considerations will, however, be dealt with in their entirety in future work.

Chapter 5

CONCLUSIONS AND FUTURE WORK

5.1 Summary

This thesis presents a data post-processing pipeline of a deep (10 μJy/beam) and wide (160 arcmin^2) VLBA survey of the CANDELS GOODS-North field. The full GOODS-North field was surveyed using the multi-phase centre technique (205 phase centres), achieving quasi-uniform sensitivity at mas resolution over this well-studied multi-wavelength field.

The wide-field VLBA pipeline is split into components, first part is written in POPS to perform initial calibration in AIPS, while the remainder of the pipeline was performed in MS format using several software that have previously not been used for VLBI (particularly flagging using AOFlagger and wide-field imaging using WSCLEAN) as this significantly improves computational performance. This, therefore, demonstrates the pipeline's ability to automatically reduce a dual polarisation VLBA continuum dataset with minimal human intervention. The importance of this pipeline is to perform these major tasks with speed and repeatability given the wide-field application.

Twelve (12) out of the 205 phase centres, which were chosen because they contained known sources have been processed. A total of 44 sub-mJy radio sources which includes eleven known sources and 33 candidate sources in a 24-hour observing time at 1.6 GHz have been reported. The positions and flux densities of the known sources are consistent with published values from Chi et al. (2013), despite the fact that these sources are relatively far away from their respective phase centres.

The candidate sources, if real, are likely AGN given the brightness temperature sensitivity limits of the survey. Moreover, the calculated radio luminosities of the candidate sources

exceeding $L_{1.6\mathrm{GHz}} > 2 \times 10^{21}$ WHz^{-1} would support AGN origins if they are verified as real detections (Kewley et al., 2000; Middelberg et al., 2010, 2011).

Nine out of the eleven of the known sources were found at centres of galaxies and this presupposes they are highly likely to be AGNs. It is highly likely the astronomical source (J123642+621545) which was detected by Chi et al. (2013) and Morrison et al. (2010b) but which was undetected in this work is either fully or marginally resolved at this wide-field VLBI resolution or the source is time-variable. This is because the elapsed time of the survey by Chi et al. (2013) and this VLBA observations of the GOODS-North field is significant, given that this survey was carried out almost a decade after that of Chi et al. (2013) and Morrison et al. (2010b). Moreover, the missing source, J123642+621545 was also missed by Radcliffe et al. (2018) and had been found to have an e-MERLIN integrated flux density of 60 μ Jy and an integrated flux density value of 343 μ Jy by Chi et al. (2013) at the same period of observation confirming its variability.

Finally, by using these new tools for the analysis of massive VLBI data on wide-field surveys, these preliminary results suggest discovery spaces may be opening up.

5.2 Remainder Of The Survey

Future work involves conducting a detailed statistical analysis of the candidate sources and processing the rest of the field. The calibration could be improved by performing multi-source self-calibration (MSSC). This will be achieved by using the positions of the known detections to *uv*-stack and self-calibrate further (Radcliffe et al., 2016), where the multiple target sources that are detected (the known sources) in this field via the standard phase referencing mode are modified so that each data set approximates to a point source (Middelberg et al., 2013; Radcliffe et al., 2016) because this method is highly likely to improve the SNR of the snapshot images (1024×1024 images). The technique of MSSC may significantly increase the number of these candidate sources in this survey (Radcliffe et al., 2016).

Likelihood ratio (LR) test (Sutherland & Saunders, 1992; McAlpine et al., 2012) which combines information about the brightness distribution of the higher resolution data (VLBI) and positional errors in both the radio source catalogues (VLBI candidate sources) and the multi-wavelength data set (e.g., NIR, X-ray) to would be used to determine the most likely counterparts (McAlpine et al., 2012).

Young sources often have inverted flux densities. That is to say that the higher the frequency, the higher the flux density of the sources. This means sources that might have been missed by the VLBA 1.6 GHz survey have a higher probability of being detected at higher frequencies. This is because there is less RFI at a 5 GHz VLBI survey compared to a VLBI survey at 1.6 GHz and there are also higher identification rates than lower frequencies. Secondly, since the

impact of the ionosphere is inversely proportional to frequency (Middelberg & Bach, 2008), a VLBI survey at 5 GHz will be less affected by the ionosphere. Moreover, re-observing the CANDELS GOODS-North field will allow better estimation of false positive ratio and missed candidate source ratio at different levels of detection significance (Deller & Middelberg, 2014). With this in mind, a 5 GHz survey of the CANDELS GOODS-North is proposed to be carried out in the future.

5.3 Conclusion

The GOODS-North field was previously surveyed by (Chi et al., 2013) using conventional wide-field VLBI observational method and detected 12 radio sources. This pilot project involved observing the same GOODS-North using a new wide-field VLBI technique (multi-phase centre correlation method). Secondly, the phase centres in this work were not chosen based on pre-selected positions. Data for twelve phase centres were processed and forty-four sources were detected across a redshift of 0.09 - 5.11. Eleven of these detected sources in this work are previously known. The flux densities and positions of these sources are consistent with previously published works except for one source. One known source was undetected in this work, which suggests high variability of the source as it was also missed in other surveys (eg., Radcliffe et al., 2016, 2018).

It should also be mentioned that the pipeline developed in this pilot survey was only tested on VLBA datasets, but it could in principle be applied to other homogeneous arrays. It has, however, not been tested on datasets from heterogeneous arrays which add significant complexities (refer to Radcliffe et al., 2018). It is also pertinent to say that the pipeline is not fully automated, thus, human intervention is needed, especially when running the first part of the pipeline implemented in AIPS. The implementation of the code in AIPS is a bit laborious and needs to be fully automated. The purpose-built source finder is computationally expensive but can however be optimised. The 5.5 sigma and 7 sigma thresholds clearly need to be optimised by implementing the false positive probability as an additional criterion to the purpose-built source finder. The code is not currently available to the general user. Validation and verification tests need to be conducted before it can be released to the general user.

The pipeline developed in this pilot survey could be used towards processing the MIGHTEE-VLBI survey data when available. This is because MIGHTEE-VLBI will be focused on galaxy observations in the continuum where synchrotron emission and free-free emission are abundant and this will help in the study of AGN versus star formation emission separation and evolution of accretion activities over cosmic time as indicated in Section 1.3.4. As predicted

by Garrett et al. (1999), 'VLBI sensitivity approaches the sub-mJy level, a wide-field approach to data analysis becomes inevitable' and this work supports his assertions.

Appendix A

Multi-wavelength Catalogue of GOODS-North Field

Purpose-built Source Finder credited to Roger Deane.

The multi-wavelength catalogue used for the purpose-built source finder in Chapter 3.2.2.6.1 is presented in the paragraphs below:

The catalogue from the 3D-*HST* survey was obtained via a 248-orbit *Hubble Space Telescope* treasury program by Momcheva et al. (2016). The 3D-HST covers an area of 625 arcmin ^{2} of CANDELS. The survey obtained Wide Field Camera 3 (WFC3) G141 (IR Grism calibration files with a resolution power of 130@1400 nm and a wavelength of 1075-1700 MHz) spectroscopic data which is augmented with data from GO-1600 in GOODS-North. The WFC3 G141 grism has spectral coverage from 1.1 to 1.65 μm and a peak transmission of 48% at 1.45 μm (Momcheva et al., 2013). In their work, Momcheva et al. (2016) catalogued 98,668 with measured redshifts and line strength down to $JH_{IR} \leqslant 26$[1] and 22,548 with $JH_{IR} \leqslant 24$, where emission continuum were detected. Of these, 5,459 of the sources were classified as galaxies at $\mathrm{z} > 1.5$ and 9,621 at $0.7 < \mathrm{z} < 1.5$ with a redshift precision of $\sigma_z \approx 0.003(1+z)$ and with a 3σ limit for emission line flux values of point sources given as 1.5×10^{-17} ergs cm^{-2} s^{-1} (Momcheva et al., 2016).

The X-ray catalogue used for this work consists of point sources for the ≈2 Ms exposure of the *Chandra* Deep field North survey. This happens to be one of the Deepest X-ray observations of the universe in the 0.5-8.0 keV band (Alexander et al., 2003). The on-axis sensitivity limits for the 0.5-2.0 keV and 2.0-8.0 keV bands are $\approx 2.5 \times 10^{-17}$ ergs cm^{-2} s^{-1} and $\approx 1.4 \times 10^{-16}$ ergs cm^{-2} s^{-1} respectively whiles the average backgrounds in the 0.5-2.0 keV and 2.0-8.0 keV bands are reported to be 0.056 and 0.135 Ms^{-1} pixel^{-1}, respectively.

[1] JH: J Band and H band

Alexander et al. (2003) reported that out of the 503 X-ray detections over the entire ≈448 arcmin^2 in and up to the defined X-ray bands, twenty (20) of these sources lie in the ≈5.3 arcmin^2 Hubble Deep Field North (HDFN; 13.600^{+3800}_{-3000} sources deg^{-2}). Majority of the detected sources were reported by Alexander et al. (2003) to be starburst and normal galaxies.

The radio data catalogue used for this work is a wide-field radio continuum survey covering a region of $40' \times 40'$ of the GOODS-North field. The survey was conducted in November 1996 with the VLA at 1.4 GHz by Morrison et al. (2010b), centered at 12:36:49.4, +62:12:58, total integration time of 50 hr and at an integrated time of 5 s. Resultant maps with synthesized beam size of $\sim 1.7''$ with r.m.s. noise of ~ 3.9 $\mu\mathrm{Jybeam}^{-1}$ near the centre were produced. About 1,230 discrete radio emitters were catalogued within the field above 5σ detection threshold of ~ 20 Jy at the field centre.

The data from NIR is a *Spitzer* deep extragalactic survey which is a cycle 8 exploration survey to detect galaxies at very high redshifts. This survey was carried out within five widely separated extragalactic field including the HDFN by Ashby et al. (2015a). The survey covered a total area of 0.16 deg^2 in both of the warm Infrared Array Camera (IRAC) dual-band of $3.6 + 4.5$ μm and. The *Spitzer*-Cosmic Assembly Deep Near-Infrared Extragalactic Legacy Survey S-CANDELS covered a depth of 26.5 AB mag (3σ) with total exposure time of 50 hrs. The survey of the S-CANDELS by Ashby et al. (2015a) catalogued a deep IRAC counts of 135, 000 galaxies which was consisted with models based on known galaxy populations.

A summary of the survey by Chi et al. (2013) which we used for the comparison of our initial resulsts is given in the next paragraph:

The survey of the HDFN and flanking field (HFF) by Chi et al. (2013) was observed at 1.4 GHz on 20-22 February 2004 with the global VLBI array consisting of sixteen (16) telescopes in Europe and USA. In their work, Chi et al. (2013) used wide-field imaging technique which was previously introduced by Garrett et al. (1999) to image out the entire HDF-N and HFF. The entire field they survey was 201 arcmin^2 and with an array sensitivity of 7.3 $\mu Jy/$ beam and with a 4 mas angular resolution in the central 0-2" part. They reported twelve detections of AGN-driven sources of which most had X-ray detected counterparts.

Bibliography

2000, Perspectives on Radio Astronomy: Science with Large Antenna Arrays

Agudo I., Boettcher M., Falcke H., Georganopoulos M., Ghisellini G., Giovannini G., Giroletti M., Gomez J. L., Gurvits L., Laing R., et al., 2015, arXiv preprint arXiv:1501.00420

Agudo I., Krichbaum T., Ungerechts H., Kraus A., Witzel A., Angelakis E., Fuhrmann L., Bach U., Britzen S., Zensus J., Wagner S., Ostorero L., Ferrero E., Gracia J., Grewing M., 2006, Astronomy and Astrophysics, 456, 117

Agudo I., Marscher A. P., Jorstad S. G., Larionov V. M., Gómez J. L., Lähteenmäki A., Smith P. S., Nilsson K., Readhead A. C., Aller M. F., et al., 2011, The Astrophysical Journal Letters, 735, L10

Alexander D., Bauer F., Brandt W., Schneider D., Hornschemeier A., Vignali C., Barger A., Broos P., Cowie L., Garmire G., et al., 2003, The Astronomical Journal, 126, 539

Ali Z. S., Parsons A. R., Zheng H., Pober J. C., Liu A., Aguirre J. E., Bradley R. F., Bernardi G., Carilli C. L., Cheng C., et al., 2015, The Astrophysical Journal, 809, 61

Antonucci R., 1993, Annual Review of Astronomy and Astrophysics, 31, 473

Asaki Y., Sudou H., Kono Y., Doi A., Dodson R., Pradel N., Murata Y., Mochizuki N., Edwards P. G., Sasao T., et al., 2007, Publications of the Astronomical Society of Japan, 59, 397

Ashby M., Willner S., Fazio G., Dunlop J., Egami E., Faber S., Ferguson H., Grogin N., Hora J., Huang J.-S., et al., 2015a, The Astrophysical Journal Supplement Series, 218, 33

Ashby M., Willner S., Fazio G., Dunlop J., Egami E., Faber S., Ferguson H., Grogin N., Hora J., Huang J.-S., et al., 2015b, VizieR Online Data Catalog, 221

Atemkeng M., Smirnov O., Tasse C., Foster G., Jonas J., 2016, Monthly Notices of the Royal Astronomical Society, 462, 2542

Baker A., 2015, IAU General Assembly, 22, 2259942

Baker A., Elson E., Blyth S., 2017, in American Astronomical Society Meeting Abstracts Vol. 229 of American Astronomical Society Meeting Abstracts, Characterizing source confusion in hi spectral line stacking experiments. p. 132.07

Bartel N., 2009, in Hagiwara Y., Fomalont E., Tsuboi M., Yasuhiro M., eds, Approaching Micro-Arcsecond Resolution with VSOP-2: Astrophysics and Technologies Vol. 402 of Astronomical Society of the Pacific Conference Series, Supernova vlbi. p. 243

Bartel N., Bietenholz M. F., 2003, The Astrophysical Journal, 591, 301

Bartel N., Herring T., Ratner M., Shapiro I., Corey B., 1986, Nature, 319, 733

Baum S., Zirbel E., O'Dea C., 1995, The Astrophysical Journal, 451, 88

Beasley A., Conway J., 1995, in Very Long Baseline Interferometry and the VLBA Vol. 82 of Astronomical Society of the Pacific Conference Series, Vlbi phase-referencing. p. 327

Bell E., 2003, The Astrophysical Journal, 586, 794

Bennert N., Jungwiert B., Komossa S., Haas M., Chini R., 2006, Astronomy & Astrophysics, 456, 953

Bietenholz M., 2005, in Romney J., Reid M., eds, Future Directions in High Resolution Astronomy Vol. 340 of Astronomical Society of the Pacific Conference Series, Imaging of radio supernovae. p. 286

Bietenholz M., Brunthaler A., Soderberg A., Krauss M., Zauderer B., Bartel N., Chomiuk L., Rupen M., 2012, The Astrophysical Journal, 751, 125

Bietenholz M., Soderberg A., Bartel N., Ellingsen S., Horiuchi S., Phillips C., Tzioumis A., Wieringa M., Chugai N., 2010, The Astrophysical Journal, 725, 4

Bietenholz M. F., 2008, arXiv preprint arXiv:0802.4219

Blandford R. D., Narayan R., 1992, Annual Review of Astronomy and Astrophysics, 30, 311

Blandford R. D., Netzer H., Woltjer L., Courvoisier T., Mayor M., eds, 1990, Active Galactic Nuclei

Blecher T., Deane R., Bernardi G., Smirnov O., 2017, Monthly Notices of the Royal Astronomical Society, 464, 143

Bonato M., Negrello M., Mancuso C., De Zotti G., Ciliegi P., Cai Z.-Y., Lapi A., Massardi M., Bonaldi A., Sajina A., et al., 2017, Monthly Notices of the Royal Astronomical Society, 469, 1912

Brandt W. a., Hornschemeier A., Alexander D., Garmire G., Schneider D., Broos P., Townsley L., Bautz M., Feigelson E., Griffiths R., 2001, The Astronomical Journal, 122, 1

Bridle A., 1984, The Astronomical Journal, 89, 979

Bridle A., 1989, in Synthesis Imaging in Radio Astronomy Vol. 6 of Astronomical Society of the Pacific Conference Series, Synthesis observing strategies - a "hitch-hiker's guide". p. 443

Bridle A., Schwab F., 1989, in Synthesis Imaging in Radio Astronomy Vol. 6 of Astronomical Society of the Pacific Conference Series, Wide field imaging i: Bandwidth and time-average smearing. p. 247

Brisken W., 2010 A guide to the difx software correlator

Britzen S., Vermeulen R., Campbell R., Taylor G., Pearson T., Readhead A., Xu W., Browne I., Henstock D., Wilkinson P., 2008, Astronomy & Astrophysics, 484, 119

Burke B. F., Graham-Smith F.,

Cai Z., Peng B., Nan R., Schilizzi R., Fanti C., Fanti R., Inoue M., Kameno S., 1993, Acta Astrophysica Sinica, 13, 184

Cao H.-M., Frey S., Gurvits L., Yang J., Hong X.-Y., Paragi Z., Deller A., Ivezić Ž., 2014, Astronomy & Astrophysics, 563, A111

Carozzi T., Woan G., 2009, Monthly Notices of the Royal Astronomical Society, 395, 1558

Chang C., Ros E., Kovalev Y. Y., Lister M. L., 2010, Astronomy & Astrophysics, 515, A38

Chevalier R., Fransson C., 2016, ArXiv e-prints

Chi S., Barthel P., Garrett M., 2013, Astronomy & Astrophysics, 550, A68

Chi S., Garrett M., Barthel P., , in Wang W., Yang Z., Luo Z., Chen Z., eds, The Starburst-AGN Connection Astronomical Society of the Pacific Conference Series. p. 242

Chiaberge M., Gilli R., Lotz J., Norman C., 2015, The Astrophysical Journal, 806, 147

Clark S., 1999, Towards the edge of the universe: a review of modern cosmology. Springer

Condon J., 1992, Annual review of astronomy and astrophysics, 30, 575

Condon J., 1997, Publications of the Astronomical Society of the Pacific, 109, 166

Condon J., Condon M. A., Gisler G., Puschell J., 1982, The Astrophysical Journal, 252, 102

Condon J., Cotton W., Broderick J., 2002, The Astronomical Journal, 124, 675

Condon J., Huang Z.-P., Yin Q., Thuan T., 1991, The Astrophysical Journal, 378, 65

Condon J., Ransom S.,

Condon J. J., 1989, The Astrophysical Journal, 338, 13

Condon J. J., Cotton W., Greisen E., Yin Q., Perley R., Taylor G., Broderick J., 1998, The Astronomical Journal, 115, 1693

Copley C., Thondikulam V., Loots A., Bangani S., Cloete K., Combrinck L., Gioio S., Ludick J., Nicolson G., Pollak A., et al., 2016, arXiv preprint arXiv:1608.02187

Cornwell T., Fomalont E., 1989a, in Synthesis Imaging in Radio Astronomy Vol. 6 of Astronomical Society of the Pacific Conference Series, Self-calibration. p. 185

Cornwell T., Fomalont E., 1989b, in Synthesis Imaging in Radio Astronomy Vol. 6 of Astronomical Society of the Pacific Conference Series, Self-calibration. p. 185

Cornwell T., Golap K., Bhatnagar S., 2008, IEEE Journal of Selected Topics in Signal Processing, 2, 647

Cotton W., 1989, in Synthesis Imaging in Radio Astronomy Vol. 6 of Astronomical Society of the Pacific Conference Series, Special problems in imaging. p. 233

Cotton W., 1995, in Very Long Baseline Interferometry and the VLBA Vol. 82 of Astronomical Society of the Pacific Conference Series, Fringe fitting. p. 189

Cotton W., 1999, in Synthesis Imaging in Radio Astronomy II Vol. 180 of Astronomical Society of the Pacific Conference Series, Polarization in interferometry. p. 111

Croton D. J., Springel V., White S. D., De Lucia G., Frenk C. S., Gao L., Jenkins A., Kauffmann G., Navarro J., Yoshida N., 2006, Monthly Notices of the Royal Astronomical Society, 365, 11

Davis M., , 2006, Galaxy Environments and Evolution in the GOODS-N Field, HST Proposal

Davis M., Guhathakurta P., Konidaris N. P., Newman J. A., Ashby M. L., Biggs A. D., Barmby P., Bundy K., Chapman S. C., Coil A. L., et al., 2007, The Astrophysical Journal Letters, 660, L1

De Becker M., 2007, aapr, 14, 171

de Gasperin F., 2017, Monthly Notices of the Royal Astronomical Society, 467, 2234

de Vaate J., Torchinsky S., Faulkner A., Zhang Y., Gunst A., Benthem P., van Bemmel I., Kenfack G., 2014, General Assembly and Scientific Symposium, pp 1–4

Deane R., 2017, ArXiv e-prints

Deane R., Paragi Z., Jarvis M., Coriat M., Bernardi G., Fender R., Frey S., Heywood I., Klöckner H.-R., Grainge K., Rumsey C., 2014, Nature, 511, 57

Deane R., Paragi Z., Jarvis M., Coriat M., Bernardi G., Frey S., Heywood I., Kloeckner H., 2015, Advancing Astrophysics with the Square Kilometre Array (AASKA14), p. 151

Deller A., 2009, in New Science Enabled by Microarcsecond Astrometry, held 21-23 July 2009 in Socorro Wide-field, high sensitivity vlbi surveying and astrometry with mas resolution. p. 18

Deller A., Brisken W., Phillips C., Morgan J., Alef W., Cappallo R., Middelberg E., Romney J., Rottmann H., Tingay S., et al., 2011, Publications of the Astronomical Society of the Pacific, 123, 275

Deller A., Brisken W., Romney J., Walker C., 2010, in 25th Annual New Mexico Symposium The contribution of the difx software correlator to the vlba sensitivity upgrade. p. P29

Deller A., Middelberg E., 2014, The Astronomical Journal, 147, 14

Deller A. T., Tingay S., Bailes M., West C., 2007, Publications of the Astronomical Society of the Pacific, 119, 318

Dodson R., Rioja M., 2009, ArXiv e-prints

Dotti M., Sesana A., Decarli R., 2012, Advances in Astronomy, 2012, 940568

Dressel L., 2012, Wide Field Camera 3 Instrument Handbook for Cycle 21 v. 5.0

Elbaz D., Dickinson M., Hwang H., Díaz-Santos T., Magdis G., Magnelli B., Le Borgne D., Galliano F., Pannella M., Chanial P., et al., 2011, Astronomy & Astrophysics, 533, A119

Ellingson S., 2011, IEEE Transactions on Antennas and Propagation, 59, 1855

Falcke H., Körding E., Nagar N., 2004, New Astronomy Reviews, 48, 1157

Fanaroff B. L., Riley J., 1974, Monthly Notices of the Royal Astronomical Society, 167, 31P

Fey A. L., Gordon D., Jacobs C. S., Ma C., Gaume R., Arias E., Bianco G., Boboltz D., Böckmann S., Bolotin S., et al., 2015, The Astronomical Journal, 150, 58

Fomalont E., 1981, National Radio Astronomy Observatory Newsletter, 3, 3

Fomalont E., Kopeikin S., 2002, in Proceedings of the 6th EVN Symposium Phase referencing using several calibrator sources. p. 53

Fomalont E., Perley R. A., 1999, in Synthesis Imaging in Radio Astronomy II Vol. 180 of Astronomical Society of the Pacific Conference Series, Calibration and editing. p. 79

Frey S., 2006, in Proceedings of the 8th European VLBI Network Symposium Vlbi surveys. p. 1

Frey S., Gurvits L., Paragi Z., Gabanyi K., 2012, in Resolving The Sky - Radio Interferometry: Past, Present and Future Redshift, time, spectrum - the most distant radio quasars with vlbi. p. 41

Frey S., Paragi Z., Gurvits L., Gabányi K., Cseh D., 2011, Astronomy & Astrophysics, 531, L5

Gabuzda D., Gomez J., 2001, in Galaxies and their Constituents at the Highest Angular Resolutions Vol. 205 of IAU Symposium, The compact magnetic field structures of agn from space vlbi polarization observations. p. 134

Garrett M., 2012, in From Antikythera to the Square Kilometre Array: Lessons from the Ancients Radio astronomy transformed: Aperture arrays - past, present & future. p. 41

Garrett M., 2015, Lecture 14, Cosmic Rado Sources and their Emission Processes. ASTRON, The University of Manchester

Garrett M., Muxlow T., Garrington S., Alef W., Alberdi A., van Langevelde H., Venturi T., Polatidis A., Kellermann K., Baan W., et al., 2001, Astronomy & Astrophysics, 366, L5

Garrett M., Porcas R., Pedlar A., Muxlow T., Garrington S., 1999, New Astronomy Reviews, 43, 519

Garrett M., Wrobel J., Morganti R., 2005, in Future Directions in High Resolution Astronomy Vol. 340 of Astronomical Society of the Pacific Conference Series, 21st century vlbi: Deep wide-field surveys. p. 600

Gaylard M., Bietenholz M., Combrinck L., Booth R., Buchner S., Fanaroff B., MacLeod G., Nicolson G., Quick J., Stronkhorst P., et al., 2014, arXiv preprint arXiv:1405.7214

Giavalisco M., Ferguson H., Koekemoer A., Dickinson M., Alexander D., Bauer F., Bergeron J., Biagetti C., Brandt W., Casertano S., et al., 2004, The Astrophysical Journal Letters, 600, L93

Giroletti M., Giovannini G., Taylor G., Falomo R., 2004, The Astrophysical Journal, 613, 752

Giroletti M., Orienti M., D'Ammando F., Massaro F., Tosti G., LICO R., Giovannini G., Agudo I., Alberdi A., Bignall H., Pommier M., Wolter A., 2015, Advancing Astrophysics with the Square Kilometre Array (AASKA14), p. 153

Giroletti M., Paragi Z., Bignall H., Doi A., Foschini L., Gabányi K., Reynolds C., Blanchard J., Campbell R., Colomer F., et al., 2011, Astronomy & Astrophysics, 528, L11

Goddi C., Falcke H., Kramer M., Rezzolla L., Brinkerink C., Bronzwaer T., Davelaar J., Deane R., De Laurentis M., Desvignes G., et al., 2017, International Journal of Modern Physics D, 26, 1730001

Greenstein J., Minkowski R., 1973, The Astrophysical Journal, 182, 225

Greisen E., 1990, in Longo G., Sedmak G., eds, Acquisition, Processing and Archiving of Astronomical Images The astronomical image processing system. pp 125–142

Greisen E., 2003, Information Handling in Astronomy - Historical Vistas, 285, 109

Greisen E. W., 2009, FITS Interferometry Data Interchange Convention,AIPS Memo 114. National Radio Astronomy Observatory, Socorro, New Mexico, USA, 2011

Grogin N. A., Kocevski D. D., Faber S., Ferguson H. C., Koekemoer A. M., Riess A. G., Acquaviva V., Alexander D. M., Almaini O., Ashby M. L., et al., 2011, The Astrophysical Journal Supplement Series, 197, 35

Guyon O., Roddier F., 2001, Publications of the Astronomical Society of the Pacific, 113, 98

Gwinn C., Taylor J., Weisberg J., Rawley L., 1986, The Astronomical Journal, 91, 338

Hamaker J., Bregman J., Sault R., 1996, Astronomy and Astrophysics Supplement Series, 117, 137

Hanisch R. J., Farris A., Greisen E. W., Pence W. D., Schlesinger B. M., Teuben P. J., Thompson R. W., Warnock A., 2001, Astronomy & Astrophysics, 376, 359

Harrison P., Garrington S., Beswick R., Richards A., Muxlow T., Wrigley N., Noble R., 2012, Albius report, Direction dependent calibration at cm and mm wavelengths. JBO/Manchester

Heckman T. M., Best P. N., 2014, Annual Review of Astronomy and Astrophysics, 52, 589

Hees A., Bailey Q., Bourgoin A., Pihan-Le Bars H., Guerlin C., Le Poncin-Lafitte C., 2016, Universe, 2, 30

Hillebrandt W., Niemeyer J. C., 2000, Annual Review of Astronomy and Astrophysics, 38, 191

Hodgson J., Lee S., Zhao G., Algaba J., Yun Y., Jung T., Byun D., 2016, Journal of Korean Astronomical Society, 49, 137

Högbom J., 1974, Astronomy and Astrophysics Supplement Series, 15, 417

Holwerda B., Blyth S., Baker A., 2012, in The Spectral Energy Distribution of Galaxies - SED 2011 Vol. 284 of IAU Symposium, Looking at the distant universe with the meerkat array (laduma). pp 496–499

Hopkins P. F., Hernquist L., Cox T. J., Di Matteo T., Robertson B., Springel V., 2006, The Astrophysical Journal Supplement Series, 163, 1

Karamanavis V., Fuhrmann L., Krichbaum T., Angelakis E., Hodgson J., Nestoras I., Myserlis I., Zensus J., Sievers A., Ciprini S., 2016, Astronomy & Astrophysics, 586, A60

Kardashev N., Slysh V., 1988, in The Impact of VLBI on Astrophysics and Geophysics Vol. 129 of IAU Symposium, The radioastron project (invited). p. 433

Kaspi S., Smith P. S., Netzer H., Maoz D., Jannuzi B. T., Giveon U., 2000, The Astrophysical Journal, 533, 631

Keimpema A., Kettenis M., Pogrebenko S., Campbell R., Cimó G., Duev D., Eldering B., Kruithof N., van Langevelde H., Marchal D., et al., 2015, Experimental Astronomy, 39, 259

Kellermann K., Moran J., , Annual Review of Astronomy and Astrophysics, pp 457–509

Kellermann K., Vermeulen R., Zensus J., Cohen M., 1998, The Astronomical Journal, 115, 1295

Kellermann K., Verschuur G., 1988, Galactic and extragalactic radio astronomy (2nd edition)

Kellermann K. I., Pauliny-Toth I., 1981, Annual Review of Astronomy and Astrophysics, 19, 373

Kembhavi A. K., Narlikar J. V., 1999, Quasars and Active Galactic Nuclei: An Introduction. Cambridge University Press

Kennicutt Jr R. C., Evans II N. J., Kennicutt R. C., Evans N. J., 2012, Annual Review of Astronomy and Astrophysics

Kettenis M., van Langevelde H., Reynolds C., Cotton B., 2006, in Gabriel C., Arviset C., Ponz D., Enrique S., eds, Astronomical Data Analysis Software and Systems XV Vol. 351 of Astronomical Society of the Pacific Conference Series, Parseltongue: Aips talking python. p. 497

Kewley L., Heisler C., Dopita M., Sutherland R., Norris R., Reynolds J., Lumsden S., 2000, The Astrophysical Journal, 530, 704

Kirshner R. P., Oke J., Penston M., Searle L., 1973, The Astrophysical Journal, 185, 303

Klöckner H.-R., Martínez-Sansigre A., Rawlings S., Garrett M., 2009, Monthly Notices of the Royal Astronomical Society, 398, 176

Kocevski D. D., Faber S., Mozena M., Koekemoer A. M., Nandra K., Rangel C., Laird E. S., Brusa M., Wuyts S., Trump J. R., et al., 2011, The Astrophysical Journal, 744, 148

Koekemoer A. M., Faber S., Ferguson H. C., Grogin N. A., Kocevski D. D., Koo D. C., Lai K., Lotz J. M., Lucas R. A., McGrath E. J., et al., 2011, The Astrophysical Journal Supplement Series, 197, 36

Kopeikin S., 2003, Physics Letters A, 312, 147

Kormendy J., Ho L. C., 2013, Annual Review of Astronomy and Astrophysics, 51, 511

Kraus J. D., 1966, Radio Astronomy. McGraw-Hill, Inc, New York

Krichbaum T., Alef W., Witzel A., Zensus J., Booth R., Greve A., Rogers A., 1998, Astronomy and Astrophysics, 329, 873

Krips M., Peck A., Sakamoto K., Petitpas G., Wilner D., Matsushita S., Iono D., 2007, The Astrophysical Journal Letters, 671, L5

Laing R., Bridle A., 2013, Monthly Notices of the Royal Astronomical Society, 437, 3405

LaMassa S., , 2011, Ucovering hidden black holes: obscured AGN and their relationship to the host galaxy

Lanyi G., Boboltz D., Charlot P., Fey A., Fomalont E., Gordon D., Jacobs C., Ma C., Naudet C., Sovers O., Zhang L., 2005, Baltic Astronomy, 14, 458

Lee S.-S., Lobanov A. P., Krichbaum T. P., Zensus J. A., 2016, The Astrophysical Journal, 826, 135

Leisawitz D., Zhang X., Danchi W., Leviton D., Lyon R., Martino A., Mather J., Mundy L., 2001, in American Astronomical Society Meeting Abstracts #198 Vol. 33 of Bulletin of the American Astronomical Society, Wide-field imaging interferometry. p. 861

Levanda R., Leshem A., 2010, IEEE Signal Processing Magazine, 27, 14

Lister M., Aller M., Aller H., Hovatta T., Kellermann K., Kovalev Y., Meyer E., Pushkarev A., Ros E., Ackermann M., et al., 2011, The Astrophysical Journal, 742, 27

Loh N. C., , High-Resolution Micromachined Interferometric Accelerometer

Loots A., 2015, in American Astronomical Society Meeting Abstracts Vol. 225 of American Astronomical Society Meeting Abstracts, The african vlbi network project. p. 126.02

Lu R.-S., Roelofs F., Fish V. L., Shiokawa H., Doeleman S. S., Gammie C. F., Falcke H., Krichbaum T. P., Zensus J. A., 2016, The Astrophysical Journal, 817, 173

McAlpine K., Jarvis M., Bonfield D., 2013, Monthly Notices of the Royal Astronomical Society, 436, 1084

McAlpine K., Smith D., Jarvis M., Bonfield D., Fleuren S., 2012, Monthly Notices of the Royal Astronomical Society, 423, 132

McCutchen C., 1966, Journal of the Optical Society of America (1917-1983), 56, 727

McKean J., Jackson N., Vegetti S., Rybak M., Serjeant S., Koopmans L., Metcalf R., Fassnacht C., Marshall P., Pandey-Pommier M., 2015, arXiv preprint arXiv:1502.03362

Maiolino R., Rieke G., 1995, The Astrophysical Journal, 454, 95

Maoz D., Mannucci F., Nelemans G., 2014, Annual Review of Astronomy and Astrophysics, 52, 107

Masias M., Freixenet J., Lladó X., Peracaula M., 2012, Monthly Notices of the Royal Astronomical Society, 422, 1674

Mesler R. A., Pihlström Y. M., Taylor G. B., Granot J., 2012, The Astrophysical Journal, 759, 4

Mevius M., van der Tol S., Pandey V., Vedantham H., Brentjens M., de Bruyn A., Abdalla F., Asad K., Bregman J., Brouw W., et al., 2016, Radio Science, 51, 927

Middelberg E., Bach U., 2008, Reports on Progress in Physics, 71, 66901

Middelberg E., Deller A., Morgan J., Rottmann H., Alef W., Tingay S., Norris R., Bach U., Brisken W., Lenc E., 2010, in 10th European VLBI Network Symposium and EVN Users Meeting: VLBI and the New Generation of Radio Arrays Finding agn with wide-eld vlbi observations. p. 26

Middelberg E., Deller A., Morgan J., Rottmann H., Alef W., Tingay S., Norris R., Bach U., Brisken W., Lenc E., 2011, Astronomy & Astrophysics, 526, A74

Middelberg E., Deller A. T., Norris R. P., Fotopoulou S., Salvato M., Morgan J. S., Brisken W., Lutz D., Rovilos E., 2013, Astronomy & Astrophysics, 551, A97

Miley G., 1980, Annual Review of Astronomy and Astrophysics, 18, 165

Miller D. F., 1998

Minkowski R., 1964, Annual Review of Astronomy and Astrophysics, 2, 247

Mo H., van den Bosch F., White S. D. M., 2010, Galaxy Formation and Evolution.

Mohan N., Rafferty D., , 2015, PyBDSM: Python Blob Detection and Source Measurement, Astrophysics Source Code Library

Momcheva I. G., Brammer G. B., Van Dokkum P. G., Skelton R. E., Whitaker K. E., Nelson E. J., Fumagalli M., Maseda M. V., Leja J., Franx M., et al., 2016, The Astrophysical Journal Supplement Series, 225, 27

Momcheva I. G., Van Dokkum P., Brammer G., Franx M., Skelton R., Lundgren B., Whitaker K., et al., 2013, in American Astronomical Society Meeting Abstracts# 221 Vol. 221, The 3d-hst survey: An introduction

Momjian E., Wang W., Knudsen K., Carilli C., Cowie L., Barger A., 2010, The Astronomical Journal, 139, 1622

Morgan J. S., Mantovani F., Deller A., Brisken W., Alef W., Middelberg E., Nanni M., Tingay S., 2011, Astronomy & Astrophysics, 526, A140

Morrison G., Dickinson M., Owen F., Daddi E., Chary R., Bauer F., Mobasher B., MacDonald E., Koekemoer A., Pope A., 2008, in Infrared Diagnostics of Galaxy Evolution Vol. 381 of Astronomical Society of the Pacific Conference Series, The goods-north radio galaxies: On the origin of the radio emission. p. 376

Morrison G., Owen F., Dickinson M., Ivison R., Ibar E., 2010a, VizieR Online Data Catalog, 218

Morrison G. E., Owen F. N., Dickinson M., Ivison R. J., Ibar E., 2010b, The Astrophysical Journal Supplement Series, 188, 178

Müller C., Kadler M., Ojha R., Perucho M., Großberger C., Ros E., Wilms J., Blanchard J., Böck M., Carpenter B., et al., 2014, Astronomy & Astrophysics, 569, A115

Müller C., Kadler M., Ojha R., Wilms J., Böck M., Edwards P., Fromm C., Hase H., Horiuchi S., Katz U., et al., 2011, Astronomy & Astrophysics, 530, L11

Muxlow T., Pedlar A., Wills K., Garrett M., Diamond P., Wilkinson P., Alef W., 1999, in Bulletin of the American Astronomical Society Vol. 31, Vlbi observations of supernova remnants in messier 82. p. 974

N H. R., Middelberg E., Deller A., Norris R., Best P., Brisken W., Schinnerer E., Smolcic V., Delvecchio I., Momjian E., Bomans D., Scoville N., Carilli C., 2017, ArXiv e-prints

Netzer H., 2013, The Physics and Evolution of Active Galactic Nuclei

Netzer H., 2015, Annual Review of Astronomy and Astrophysics, 53, 365

Noeske K., Weiner B., Faber S., Papovich C., Koo D., Somerville R., Bundy K., Conselice C., Newman J., Schiminovich D., et al., 2007, The Astrophysical Journal Letters, 660, L43

Norris R. P., Afonso J., Bacon D., Beck R., Bell M., Beswick R., Best P., Bhatnagar S., Bonafede A., Brunetti G., et al., 2013, Publications of the Astronomical Society of Australia, 30

Offringa A., , 2010, AOFlagger: RFI Software

Offringa A., de Bruyn A., Zaroubi S., Biehl M., 2010, ArXiv e-prints

Offringa A., McKinley B., Hurley-Walker N., Briggs F., Wayth R., Kaplan D., Bell M., Feng L., Neben A., Hughes J., et al., 2014, Monthly Notices of the Royal Astronomical Society, 444, 606

Offringa A., Van De Gronde J., Roerdink J., 2012, Astronomy & Astrophysics, 539, A95

Offringa A., Wayth R., Hurley-Walker N., Kaplan D., Barry N., Beardsley A., Bell M., Bernardi G., Bowman J., Briggs F., et al., 2015, Publications of the Astronomical Society of Australia, 32

Ojha R., Fey A. L., Johnston K. J., Jauncey D. L., Reynolds J. E., Tzioumis A. K., Quick J. F., Nicolson G. D., Ellingsen S. P., Dodson R. G., et al., 2004, The Astronomical Journal, 127, 3609

Ojha R., Kadler M., Böck M., Booth R., Dutka M. S., Edwards P. G., Fey A. L., Fuhrmann L., Gaume R. A., Hase H., et al., 2010, Astronomy & Astrophysics, 519, A45

Ostrovsky A. S., Martínez-Niconoff G., Martinez-Vara P., Olvera-Santamaría M. A., 2009, Optics express, 17, 1746

Padovani P., 2016, The Astronomy and Astrophysics Review, 24, 13

Padovani P., Miller N., Kellermann K., Mainieri V., Rosati P., Tozzi P., 2011, The Astrophysical Journal, 740, 20

Palmer J., 1996, Starlink User Note, 207

Paragi Z., 2016, ArXiv e-prints

Paragi Z., Godfrey L., Reynolds C., Rioja M., Deller A., Zhang B., Gurvits L., Bietenholz M., Szomoru A., Bignall H., et al., 2014, arXiv preprint arXiv:1412.5971

Paragi Z., Vermeulen R., Spencer R., 2012, in Resolving The Sky - Radio Interferometry: Past, Present and Future Ss433, microquasars, and other transients. p. 28

Pearson T., 1995, in Very Long Baseline Interferometry and the VLBA Vol. 82 of Astronomical Society of the Pacific Conference Series, Non-imaging data analysis. p. 267

Pearson T., Readhead A., 1984, Annual review of astronomy and astrophysics, 22, 97

Pedlar A., Muxlow T., Garrett M., Diamond P., Wills K., Wilkinson P., Alef W., 1999, Monthly Notices of the Royal Astronomical Society, 307, 761

Pérez-Torres M., Romero-Canizales C., Alberdi A., Polatidis A., 2009, Astronomy & Astrophysics, 507, L17

Petrosian V., Bykov A., Rephaeli Y., 2008, in , Clusters of Galaxies. Springer, pp 191–206

Petrov L., 2000, in Takahashi F., ed., International VLBI Service for Geodesy and Astrometry 2000 General Meeting Proceedings Instrumental errors of geodetic vlbi. pp 230–235

Pilbratt G., Riedinger J., Passvogel T., Crone G., Doyle D., Gageur U., Heras A., Jewell C., Metcalfe L., Ott S., et al., 2010, Astronomy & Astrophysics, 518, L1

Piner B., Pant N., Edwards P., 2010, The Astrophysical Journal, 723, 1150

Pober J. C., Parsons A. R., Aguirre J. E., Ali Z., Bradley R. F., Carilli C. L., DeBoer D., Dexter M., Gugliucci N. E., Jacobs D. C., et al., 2013, The Astrophysical Journal Letters, 768, L36

Pohl M., Reich W., Krichbaum T., Standke K., Britzen S., Reuter H., Reich P., Schlickeiser R., Fiedler R., Waltman E., et al., 1995, arXiv preprint astro-ph/9503082

Pollack L. K., Taylor G., Zavala R., 2003, The Astrophysical Journal, 589, 733

Porcas R., Patnaik A., 1996, in Extragalactic Radio Sources Vol. 175 of IAU Symposium, Multi-frequency vlbi observations of the gravitational lens b0218+ 357. p. 115

Pracy M. B., Ching J. H., Sadler E. M., Croom S. M., Baldry I., Bland-Hawthorn J., Brough S., Brown M., Couch W. J., Davis T. M., et al., 2016, Monthly Notices of the Royal Astronomical Society, 460, 2

Preston R., Morabito D., Williams J., Faulkner J., Jauncey D., Nicolson G., 1985, The Astronomical Journal, 90, 1599

Radcliffe J., Garrett M., Muxlow T., Beswick R., Barthel P., Deller A., Keimpema A., Campbell R., Wrigley N., 2018, arXiv preprint arXiv:1808.04296

Radcliffe J. F., Garrett M. A., Beswick R. J., Muxlow T. W., Barthel P., Deller A. T., Middelberg E., 2016, Astronomy & Astrophysics, 587, A85

Raimundo S., Fabian A., 2009, Monthly Notices of the Royal Astronomical Society, 396, 1217

Rampadarath H., Morgan J. S., Soria R., Tingay S. J., Reynolds C., Argo M. K., Dumas G., 2015, Monthly Notices of the Royal Astronomical Society, 452, 32

Randall K. E., Hopkins A. M., Norris R. P., Zinn P.-C., Middelberg E., Mao M. Y., Sharp R., 2012, Monthly Notices of the Royal Astronomical Society, 421, 1644

Readhead A., Pearson T., Taylor G., Wilkinson P., 1996, in Symposium-International Astronomical Union Vol. 175, The evolution of extragalactic radio sources. pp 88–89

Readhead A. C., 1994, The Astrophysical Journal, 426, 51

Reynolds C., Paragi Z., Garrett M., 2002, ArXiv Astrophysics e-prints

Rohlfs K., Wilson T. L., 2013, Tools of radio astronomy. Springer Science & Business Media

Romney J., 1999, in Synthesis Imaging in Radio Astronomy II Vol. 180 of Astronomical Society of the Pacific Conference Series, Cross correlators. p. 57

Romney J., Ulvestad J., Brisken W., Deller A., Walker R., Durand S., 2010, in 25th Annual New Mexico Symposium The vlba sensitivity upgrade: Science and status. p. 3

Ros E., 2005, in Romney J., Reid M., eds, Future Directions in High Resolution Astronomy Vol. 340 of Astronomical Society of the Pacific Conference Series, High precision differential astrometry. p. 482

Ros E., 2012, ArXiv e-prints

Ros E., Guirado J., Marcaide J., Pérez-Torres M. A., Falco E., Munoz J., Alberdi A., Lara L., 2000, arXiv preprint astro-ph/0009493

Ruiz N. H., Middelberg E., Norris R. P., Maini A., 2016, Astronomy & Astrophysics, 589, L2

Sadler E. M., Jackson C. A., Cannon R. D., McIntyre V. J., Murphy T., Bland-Hawthorn J., Bridges T., Cole S., Colless M., Collins C., et al., 2002, Monthly Notices of the Royal Astronomical Society, 329, 227

Sambruna R., Maraschi L., Urry C., 1996, The Astronomical Journal, 463, 444

Saripalli L., 2012, The Astronomical Journal, 144, 85

Sasao T., Fletcher A. B., 2005, Suwon: Ajou University

Schinnerer E., Sargent M., Bondi M., Smolčić V., Datta A., Carilli C., Bertoldi F., Blain A., Ciliegi P., Koekemoer A., et al., 2010, The Astrophysical Journal Supplement Series, 188, 384

Schwab F., Cotton W., 1983, The Astronomical Journal, 88, 688

Simmons B., Van Duyne J., Urry C., Treister E., Koekemoer A., Grogin N., Team G., et al., 2011, The Astrophysical Journal, 734, 121

Sjouwerman L., Mioduszewski A., Greisen E., 2005, in Romney J., Reid M., eds, Future Directions in High Resolution Astronomy Vol. 340 of Astronomical Society of the Pacific Conference Series, Nrao's vlba data calibration pipeline. p. 613

Smirnov O., 2011, Astronomy & Astrophysics, 527, A106

Strotjohann N., Saxton R., Starling R. L., Esquej P., Read A., Evans P., Miniutti G., 2016, Astronomy & Astrophysics, 592, A74

Sutherland W., Saunders W., 1992, Monthly Notices of the Royal Astronomical Society, 259, 413

Takefuji K., Terasawa T., Kondo T., Mikami R., Takeuchi H., Misawa H., Tsuchiya F., Kita H., Sekido M., 2016, Publications of the Astronomical Society of the Pacific, 128, 84502

Taylor G., Beasley A., Frail D., Kulkarni S., Reynolds J., 1999, Astronomy and Astrophysics Supplement Series, 138, 445

Taylor G. B., 2010, in American Astronomical Society Meeting Abstracts #215 Vol. 42 of Bulletin of the American Astronomical Society, The parsec-scale characteristics of fermi blazars and radio galaxies. p. 543

Thaller D., Krügel M., Rothacher M., Tesmer V., Schmid R., Angermann D., 2007, Journal of Geodesy, 81, 529

Thompson A., Bagri D., 1991, in IAU Colloq. 131: Radio Interferometry. Theory, Techniques, and Applications Vol. 19 of Astronomical Society of the Pacific Conference Series, A pulse calibration system for the vlba. pp 55–59

Thompson A. R., Moran J. M., Swenson G. W., 2001, Interferometry and Synthesis in Radio Astronomy, 2nd edition. John Wiley & Sons Inc., New York, US

Thompson A. R., Moran J. M., Swenson G. W., 2017, Introduction and Historical Review. Springer International Publishing, pp 1–58

Tilanus R., Krichbaum T., Zensus J., Baudry A., Bremer M., Falcke H., Giovannini G., Laing R., van Langevelde H., Vlemmings W., et al., 2014, arXiv preprint arXiv:1406.4650

Tingay S., Jauncey D., Preston R., Meier D., Reynolds J., Tzioumis A., Lovell J., Jones D., McCulloch P., Murphy D., et al., 1996, in , Extragalactic Radio Sources. Springer, pp 129–130

Tingay S. J., Preston R. A., Lister M. L., Piner B. G., Murphy D. W., Jones D. L., Meier D. L., Pearson T. J., Readhead A. C. S., Hirabayashi H., Murata Y., Kobayashi H., Inoue M., 2001, The Astrophysical Journal Letters, 549, L55

Treister E., Schawinski K., Urry C., Simmons B., 2012, The Astrophysical Journal Letters, 758, L39

Tremaine S., Gebhardt K., Bender R., Bower G., Dressler A., Faber S. M., Filippenko A. V., Green R., Grillmair C., Ho L. C., et al., 2002, The Astrophysical Journal, 574, 740

Turin G., 1960, IRE Transactions on Information Theory, 6, 311

Ulvestad J., 1999, in American Astronomical Society Meeting Abstracts #194 Vol. 31 of Bulletin of the American Astronomical Society, Capabilities of the very long baseline array. p. 921

Urry C. M., Padovani P., 1995, Publications of the Astronomical Society of the Pacific, 107, 803

Urry M., 1999, in BL Lac Phenomenon Vol. 159 of Astronomical Society of the Pacific Conference Series, Bl lac objects and blazars: Past, present and future. p. 3

van den Bergh S., Tammann G. A., 1991, Annual Review of Astronomy and Astrophysics, 29, 363

van Haarlem M. á., Wise M., Gunst A., Heald G., McKean J., Hessels J., De Bruyn A., Nijboer R., Swinbank J., Fallows R., et al., 2013, Astronomy & Astrophysics, 556, A2

van Velzen S., Falcke H., Körding E., 2014, Monthly Notices of the Royal Astronomical Society, 446, 2985

Venturi T., Cotton W., Feretti L., Giovannini G., Lara L., Marcaide J., 1996, in Extragalactic Radio Sources Vol. 175 of IAU Symposium, Vlbi observations of fri radio galaxies. p. 124

Walker R., 1995, in Very Long Baseline Interferometry and the VLBA Vol. 82 of Astronomical Society of the Pacific Conference Series, Practical vlbi imaging. p. 247

Walker R., 1999, in Synthesis Imaging in Radio Astronomy II Vol. 180 of Astronomical Society of the Pacific Conference Series, Very long baseline interferometry. p. 433

Walker R., 2015, in THE SCHED USER MANUAL Version 11.4, Release of March 14, 2015 The sched user manual

Wandel A., Peterson B., Malkan M., 1999, The Astrophysical Journal, 526, 579

Wang L., Cui X., Zhu H., Tian W., 2015, Advancing Astrophysics with the Square Kilometre Array (AASKA14), p. 64

Weiler K., Sramek R., , in The Interpretation of Modern Synthesis Observations of Spiral Galaxies Astronomical Society of the Pacific Conference Series, The observation and interpretation of radio supernovae in nearby galaxies, volume = 18, year = 1991. pp 91–101

Weiler K., Sramek R., Panagia N., Van Der Hulst J., Salvati M., 1986, The Astrophysical Journal, 301, 790

Weiler K. W., Panagia N., Sramek R. A., Van Dyk S. D., Williams C. L., Stockdale C. J., Kelley M. T., 2007, in AIP Conference Proceedings Vol. 937, Radio emission from supernovae. pp 256–263

Weisskopf M. C., Tananbaum H. D., Van Speybroeck L. P., O'Dell S. L., 2000, in X-Ray Optics, Instruments, and Missions III Vol. 4012, Chandra x-ray observatory (cxo): overview. pp 2–17

Wells D., 1985, in Data Analysis in Astronomy Nrao's astronomical image processing system (aips). p. 195

Whitney A., 2006 Vol. 82 of IVS 2006 General Meeting Proceedings, The mark 5b vlbi data system. pp 200–205

Wild S., 2017, Nature News, 545, 144

Williams R. E., et al., 1996, arXiv preprint astro-ph/9607174

Woltjer L., 1972, Annual Review of Astronomy and Astrophysics, 10, 129

Woosley S., Heger A., Weaver T. A., 2002, Reviews of Modern Physics, 74, 1015

Woosley S., Weaver T. A., 1986, Annual Review of Astronomy and Astrophysics, 24, 205

Wrobel J., Taylor G., Myers S., Fassnacht C., 2001, An NRAO VLBA Survey of FIRST Sources in the NOAO Deep Wide Field J1432+3416. Springer Berlin Heidelberg, Berlin, Heidelberg, p. 308

Zhang M., , 2016, SAND: Automated VLBI imaging and analyzing pipeline, Astrophysics Source Code Library

Zhang Y., An T., Frey S., Gabányi K. É., Paragi Z., Gurvits L. I., Sohn B. W., Jung T., Kino M., Lao B., et al., 2017, Monthly Notices of the Royal Astronomical Society, 468, 69